2016

Development of high capacity composite anode materials for rechargeable lithium/sodium ion battery

Qiuran Yang
University of Wollongong

Institute for Superconducting & Electronic Materials

Development of high capacity composite anode materials for rechargeable Lithium/Sodium Ion Battery

Qiuran Yang

This thesis is presented as part of the requirements for the

Award of the Degree of Master of Philosophy

University of Wollongong

July 2016

CERTIFICATION

I, Qiuran Yang, declare that this thesis, submitted in partial fulfilment of the requirements for the award of Mater of Philosophy, in the Institute for Superconducting & Electronic Materials (ISEM), Faculty of Engineering, University of Wollongong, NSW, Australia, is an originally work of me unless otherwise referenced or acknowledged. This thesis has not been submitted to other academic institutions for qualifications.

Qiuran Yang

July 2016

ACKNOWLEDGEMENTS

First of all, I would like to convey my gratitude towards my supervisors, Dr. Shulei Chou and Prof. Huakun Liu, for their continuous patient and professional support and guidance. Strongly, I would like to thank Dr. Shulei for giving me great encouragement in various ways during my Master studies.

I would strongly express my appreciation towards Prof. Jiazhao Wang for giving encouragement and help during my master study. I would also convey my appreciation to Dr. Tania Silver, who are always carefully reviewing my manuscripts and polish the expressions.

I would like to thank Prof. Yemin Hu (Shanghai Univeristy) for his contributions in the cooperation work during my master study. I would also like to thank Prof.Zhanliang Tao(NanKai University) and Dr.Yuanzhen Chen(Xian Jiaotong Univeristy) for their help and suggestions during my master study.

I would also like to give my appreciations to Dr. Gilberto Casillas (EMC), Dr. Dongqi Shi (ISME), Dr. Germanas Peleckis (ISME), Dr. Tony Romeo (EMC),for their technical assistances in my master study. I would also like to give my thank to Ms. Joanne George, Ms. Narelle Badger, and Ms. Crystal Mahfouze for giving me assistance in my master study.

I also would like to thank my labmates Dr.Weijie Li,Dr. Yunxiao Wang, Mr. Mingzhe Chen, Mr. Zhe Hu, Mr. Boyang Ruan, Mr. Yuhai Dou, Dr. Zhijia Zhang, Dr Jun Wang, Dr Lanling Zhao, Dr. Qi Li, Dr.Lily Liu, Dr. Wenbin Luo , Mr. Weihong Lai, Mr.

Haipeng Guo, Mr Zhixin Tai, Mr Chandraselar subranmaniyam, Mr Wenchao Zhang, Ms.Qiannan Liu, Ms Yanfei Xu, Ms Yajie Liu, Ms Dan Zhang, Ms Yu Zhang and other members in ISEM for their kindly sharing knowledge and experience with me and always help me in my master study.

Finally, I would like to give my gratitude to all of my friends and relatives who give me lots of help and support during my master study in the University of Wollongong. This thesis is dedicated to them.

ABSTRACT

Renewable energy resources such as solar energy and wind energy can be used in generating electric instead of traditional fossil fuels. These sources of energy are not constant, however. Low-cost rechargeable lithium ion batteries and sodium ion batteries can be used as energy storage devices to smooth out the intermittency of the renewable energy, besides acting as new, clean, and portable energy resources themselves, which can be applied in mobile phones, laptop computers, electric cars, etc. My Master's thesis work is focused on the study of anode materials for LIBs and NIBs. The obtained materials are Si/C/Fe/Sn nanocomposite and Sn/SnO_2@C composite nanofibers as anode materials for the lithium ion battery and FeP/graphite as anode material for the sodium ion battery.

The Si/Fe/Sn/Carbon composite was prepared by the simple high energy ball milling method. Based on the X-ray diffraction, transmission electron microscopy, and X-ray photoelectron spectroscopy results, the obtained frogspawn-like composite is a composite of silicon crystals embedded in an amorphous matrix. The frogspawn-like structure can deliver outstanding electrochemical performance, since the amorphous matrix can efficiently accommodate the volume changes; the "spawn" has electrically conductive shells continuously connected to each other, which are beneficial for improving the electrical conductivity of silicon; and the continuous carbon network can restrict the agglomeration of silicon and tin during prolonged cycling. The initial

capacity of the Si/Sn/Fe/C composite tested in lithium bis(fluorosulfonyl)imide (LiFSI) electrolyte is 1274 mAh g^{-1}, and even after 1000 cycles, the capacity remains high at 620 mAh g^{-1}, which is excellent.

Sn/SnO_2@C composite nanofibers were successfully fabricated by a facile annealing strategy. The composite consists of an amorphous carbon matrix encapsulating carbon nanotubes decorated by ultrafine (< 10 nm) SnO_2 nanoparticles, with submicron Sn particles incorporated in the entangled networks of the composite nanofibers. When used as anode material for lithium ion batteries, the Sn/SnO_2@C composite nanofibers exhibited a high initial charge capacity of 756 mAh g^{-1} at 100 mA g^{-1}, excellent high-rate capacity of 190 mAh g^{-1} at 5 A g^{-1}, and excellent capacity retention of 591 mAh g^{-1} after 100 cycles at 100 mA g^{-1}. High-resolution transmission electron microscopy, energy dispersive spectroscopy mapping, X-ray photoelectron spectroscopy, and electrochemical impedance spectroscopy were applied to investigate the origins of the excellent electrochemical Li^+ storage properties of Sn/SnO_2@C. It could be deduced that the ductile carbon matrix and free spaces in the composite nanofiber networks can effectively accommodate the strain of volume changes during cycling, prevent the aggregation and pulverization of Sn/SnO_2 particles, keep the whole structure stable, and facilitate electron and ion transport through the electrode.

Graphite performs well as anode material in lithium ion batteries, but it has no capacity in sodium ion batteries. Silicon has the highest theoretical capacity in lithium batteries, but it has no capacity in sodium ion batteries at room temperature. Among all the alloy

elements, phosphorus has the highest theoretical capacity of 2596 mAh g^{-1}, which makes phosphorus a promising anode material for sodium ion batteries, with theoretical capacity of 2596 mAh g^{-1}. Phosphorus has a low electrical conductivity of 1×10^{-14} $S \cdot cm^{-1}$, however, which results in poor cycling and rate performances. Even if it is alloyed with conductive Fe, it still delivers poor electrochemical performance. In this thesis, FeP/graphite composite has been synthesized using the simple, cheap, and productive method of low-energy ball milling, which is an efficient way to improve the electrical conductivity of FeP compound. The cycling performance was improved significantly, and when the current density increased to 500 mA g^{-1}, the FeP/graphite composite could still deliver capacity of 134 mAh g^{-1}, which was more than twice the capacity of the FeP compound alone. Our results suggest that by using a low-energy ball-milling method, promising FeP/graphite anode material can be synthesized for the sodium ion battery.

Table of content

LIST OF FIGURES

LIST OF TABLES

CHAPTER 1 INTRODUCTION

The traditional energy resource, fossil fuel, is responsible for a serious risk to the present energy economy because of the continuous increase in the depletion of nonrenewable resources and the rapid increase in CO_2 emissions, which results in global climate change. This has led to urgency in the demand for investment and exploration of renewable energy, leading to the fast development of the wind and solar energy industries and the high energy storage systems based on the lithium ion battery. The lithium ion battery is an efficient energy storage system as well as a clean energy power source, which is already widely applied in our daily lives. The history of the lithium ion battery started early, before 1980s with the application of TiS_2. $LiCoO_2$ was first reported as cathode material for the lithium ion battery by Goodenough's group, and it is widely utilized as a commercialized material. The great success of lithium ion battery applications has resulted in a shortage of lithium sources such as high-energy cobalt-based materials, which is responsible the increasing cost of lithium-ion batteries. Compared to lithium sources, sodium element is evenly distributed, and rich deposits exist in the Earth's crust. In addition, the sodium ion and the lithium ion have similar ionic radii (1.02Å and0.76 Å) and similar redox potentials versus standard hydrogen electrode (-2.71 V and -3.6 V). Because of the similarities in chemical properties between sodium and lithium, and the practically infinite sodium resources, the sodium-ion battery has become a hot research topic, and the development of high energy density sodium ion batteries has become an urgent issue.

The key issue during for the development of lithium ion and sodium ion batteries is to increase the energy density. Thus, it is crucial to obtain suitable anode materials that can be applied in lithium ion batteries (LIBs) and sodium ion batteries (NIBs). Considering the anode materials suitable for LIBs, alloy elements have the highest theoretical capacity, although the huge volume changes during the charge-discharge process and the low electrical conductivity result in a short cycle life and poor rate performance, which are obstructing their application. Up to the present, the commercialized anode material for LIBs is graphite, which has a low theoretical capacity of 375 mAh g^{-1}. For the NIBs, the situation is similar. The alloy element P has the highest theoretical capacity of 2560 mAh g^{-1}, although the huge volume changes and low electrical conductivity are obstructing application.

My Master's work is focused on the search for and synthesis of suitable anode materials for application in lithium ion batteries and sodium ion batteries, which have long cycle life, high rate performance, and are also low-cost and environmentally friendly. An outline of my Master's thesis can be described as follows: Find the most suitable and promising alloy element based on previous study; synthesize the material (Si/Fe/Sn/C nanocomposite, Sn/SnO_2@C composite, and FeP/graphite composite) by simple ball milling and a facile annealing method; analyze the crystal structure, morphology, and electrochemical performance by using X-ray diffraction (XRD), scanning electron microscopy (SEM), transmission electron microscopy (TEM), X-ray photoelectron spectroscopy (XPS), galvanostatic electrochemical testing, etc.

My thesis includes 7 chapters:

Chapter 1 gives a brief background for the work and the outline of my Master's thesis.

Chapter 2 presents basic background information on lithium-ion and sodium ion battery and give explanations of the basic mechanisms and concepts of the thesis. In addition, it introduces the anode materials, carbon materials, silicon based materials, and phosphorus based materials, and introduces the electrolytes used in lithium ion and sodium ion batteries.

Chapter 3 contains the synthesis and characterization methods used in my Master's work.

Chapter 4 presents the Si/Fe/Sn/Carbon composite synthesized by the simple ball milling method, which delivers extraordinary electrochemical performance as anode material in lithium ion batteries, and explains the mechanism.

Chapter 5 presents Sn/SnO_2@C anode composite nanofibers, which were successfully prepared by a facile annealing method and exhibit excellent electrochemical performance, with an initial charge capacity of 756 mAh g^{-1}, and can sustain stable cycling, with a charge capacity of 591 mAh g^{-1} retained after 100 cycles at 100 mA g^{-1} in lithium ion batteries.

Chapter 6 presents the FeP/graphite composite prepared by a simple low-energy ball-milling method. The results demonstrate that, after ball milling with graphite, the cycling and high-rate performance of FeP compound are greatly improved: the FeP/graphite presents 58% retention of discharge capacity with respect to the second cycle; when the current density increased to 500 mA g^{-1}, the FeP/graphite composite still delivered 134 mAh g^{-1}, which is more than twice the capacity of the FeP compound.

The graphite was converted to amorphous carbon after ball milling, which serves as a conductive matrix to strongly connect the particles, hinder aggregation, and improve the electrical conductivity. Our results suggest that FeP/graphite composite will be a cheap and productive anode material for sodium ion batteries in the future.

Chapter 7 gives the conclusion.

CHAPTER 2 LITERATURE REVIEW

The present traditional energy sources are mostly fossil fuels such as coal and oil, which are non-renewable and can cause serious pollution. With the fast development of technology and economic growth, it is becoming more and more urgent to develop the environmentally friendly energy sources which have high energy density and are low cost. Clean energy resources, such as wind energy, solar energy, wave energy, and nuclear energy are promising replacements for traditional energy sources, although these kinds of energy are climate restricted, uncontrollable, high-cost, and intermittent. Thus, rechargeable lithium-ion and sodium-ion batteries, which can not only be utilized alone, but can also be included in renewable energy systems for energy storage, are promising devices in the near future.

2.1.1General background on the lithium-ion battery

The history of the lithium ion battery started early, well before the 1980s with the application of TiS_2. Goodenough's group was the first to report $LiCoO_2$ as a cathode material for the lithium ion battery, and it is widely utilized as a commercialized material nowadays. The motivation for using the lithium ion battery is that Li is the most electropositive (-0.304 V) metal as well as the third lightest metal [1], thus endowing the battery with high energy density, as shown in Fig. 2.1[2].

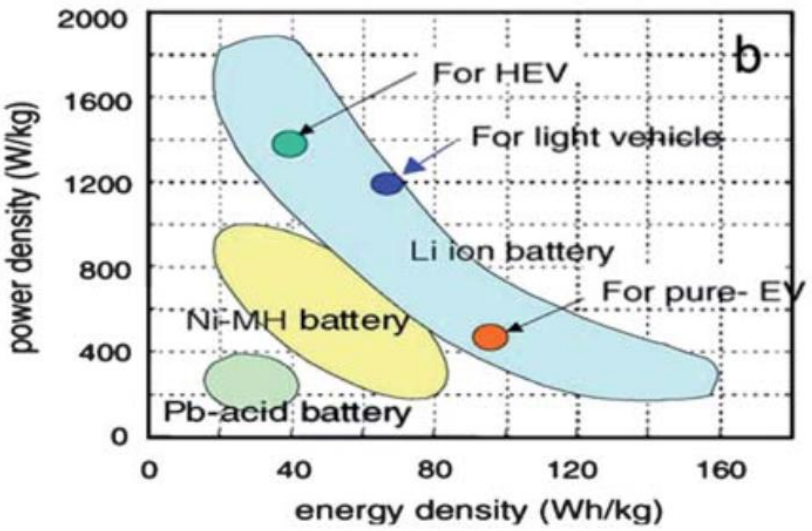

Fig. 2.1 Comparison of energy densities of different batteries.

In the stages, the primary negative material for the lithium-ion battery was Li metal. The disadvantage of using Li metal as the anode material is the uneven growth of this metal during cycling, which can result in a dangerous explosion. The most efficient way to avoid this hazard is to use a second insertion compound to take place of Li metal. In the 1980s, Goodenough's group [3] applied a layered structured lithium containing oxide compound, Li_xCoO_2, as cathode material, which was first commercialized by the Sony Company in the early 1990s and is now widely used in lithium-ion secondary battery. The first commercialized anode material applied in lithium-ion batteries was graphite, which has capacity of over 300 mAh g^{-1} (with the stoichiometry of LiC_6) and high coulombic efficiency. It is still widely utilized.

2.1.2 General background on the sodium-ion battery

Because of the successful commercialization of the lithium ion battery, the lithium industry developed rapidly, which has resulted in a shortage of lithium sources such as Li_2CO_3, thus increasing the cost of lithium-ion batteries. Comparing to Li resources,

sodium resources are richer in the Earth's crust, as shown in Fig. 2.2. In addition, sodium and lithium have many chemical and physical similarities, which results in the possibility that the sodium ion battery might become a commercial reality. Thirdly, sodium has a redox potential of -2.71 V (vs. standard hydrogen electrode (SHE)). Because of these reasons, the sodium ion battery has promise for replacing the lithium ion battery in the future. Although the study of the sodium ion battery has recently been undergoing rapid development, research on it started early. Na_xCoO_2 was the first potential cathode material reported for the sodium ion battery. The development of this battery system was suspended for about 20 years due to the difficulty in finding a suitable anode material that would be applied at room temperature. At the beginning of the 20th century, the sodium ion battery was being given attention again, as shown in Fig. 2.3. Publications on the sodium ion battery have increased dramatically in the past five years. Compared to the lithium ion battery, the energy density of the sodium ion battery is much lower, so it is important to find high capacity and long-cycle-life negative materials.

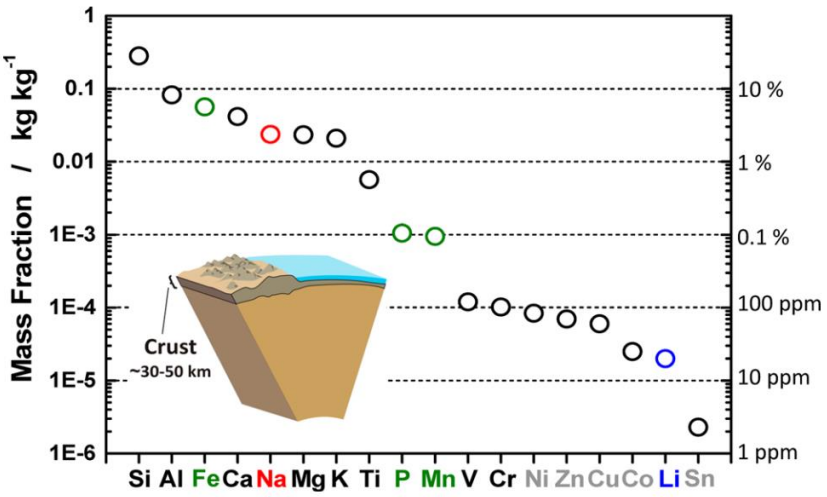

Fig 2.2 Contents of elements in the Earth's crust[4]

The most widely commercialized carbonaceous negative material for the lithium ion battery is graphite, which has a high theoretical capacity of 372 mAh g^{-1} and a low reaction potential below 0.2 V [5-6]. It also has high coulombic efficiency and excellent cycling performance. Unfortunately, graphite has been proven to have no capacity in the sodium ion battery [7]. In the last century, there were seldom any reports about the negative material for the sodium ion battery, until hard carbon was demonstrated to have a high capacity of nearly 300 mAh g^{-1} in a sodium ion battery. Its cycling performance is not as good as that of graphite, however. Meanwhile, research on cathode materials for the sodium ion also progressed rapidly. To date, the cathode materials mainly include layered oxides and polyanionic compounds, cathode materials that show a capacity range of 120-200 mAh g^{-1} and a narrow operation voltage range of 2.6 V to 3.2 V. Another important aspect of studying the sodium ion battery is to find suitable electrolytes, for there are some differences between sodium and lithium in aprotic polar solvents. For example, it is hard to form a stable solid interphase for metallic sodium anode in organic electrolytes compared to Li. In addition, the reduction products are easily generated at the anode, which can be oxidized at cathode, thus causing lower coulombic efficiency.

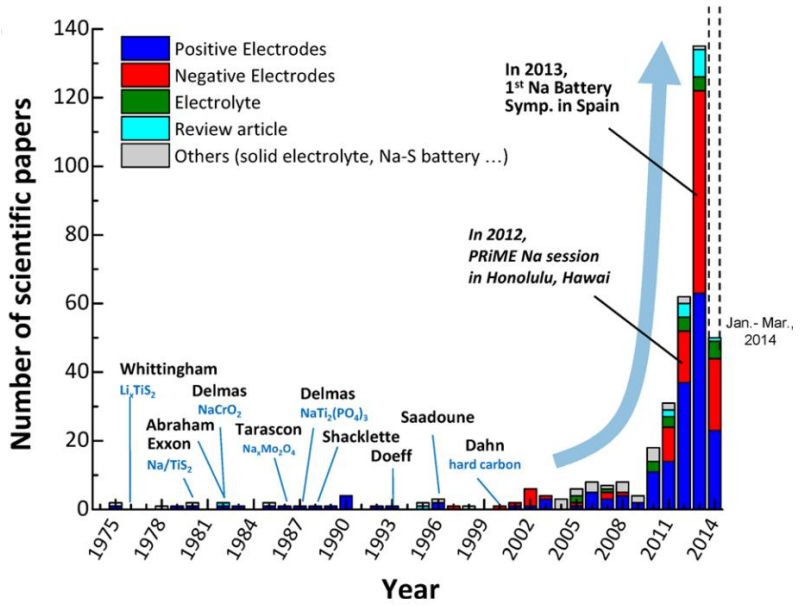

Fig. 2.3 Publications on the sodium ion battery from 1975 to 2014.

2.1.3 Basic mechanism and concepts

The structures of sodium ion batteries and lithium ion batteries are similar. As shown in Fig. 2.4, both the lithium ion battery and the sodium ion battery consist of three parts: the negative electrode (anode), the positive electrode (cathode), and the (liquid or solid) electrolyte between them.

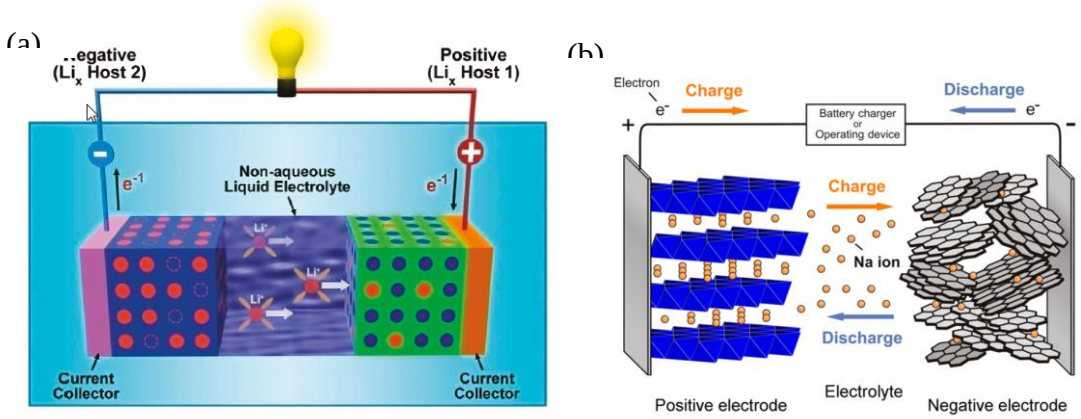

Fig. 2.4 Schematic illustration of (a) lithium ion and (b) sodium ion batteries.

When the cell is charged, large numbers of electrons released from the cathode move along the external circuit to the anode. At the same time, the charge carrier Li^+ (or Na^+)

ions move from the positive to the negative side. When the cell is discharged, the Li^+ (or Na^+) ions will be inserted into the positive material, meanwhile the electrons move from the anode to the cathode. The Li^+ (or Na^+) ions flow between negative and positive, which makes the battery store and release energy.

The basic concepts are as follows:

(1) Specific Capacity (Q_c)

Capacity is the total amount of electrode charge in the cell, involving the oxidation and reduction (redox) reactions during the charging and discharging process, and the specific capacity is the capacity per unit weight or per unit area of the material. The equation is:

$$Q = \frac{\int_{e1}^{e2} I(e)de}{m} = \frac{\mathrm{nzF}}{m} = \frac{n \times F}{m}$$

Where *n* is the mole number of ions, *F* is the Faraday constant (96485C mol^{-1}), and *m* is the weight of the active material.

(2) Theoretical capacity

Theoretical capacity is the capacity theoretically calculated based on the material. The equation is:

$$Q = \frac{n \times F \times 1000}{M \times 3600}$$

Where *F* is the Faraday constant (96485C mol^{-1}), *n* is the mole number of the electrons, and *M* is the molar mass of the active material.

(3) Coulombic efficiency

The coulombic efficiency is the ratio of the output energy/ input energy and it can be calculated from the charge and discharge capacities.

(4) Rate capacity

Rate capacity is the capacity of the material at different current densities. Rate is the ratio of current density to theoretical capacity, usually given the symbol C. For example, if the theoretical capacity is 2000 mAh g^{-1}, 0.2 C means 400 mA g^{-1}.

(5) Power density

Power density means the maximum power output of the battery, usually in terms of W/kg and W/L.

2.2. Negative electrode materials

The normal negative materials for lithium ion and sodium ion batteries include carbon materials, alloy compounds, transition metal oxides, and metal sulphides. A suitable anode material for a lithium ion battery requires high rate capacity, long cycle life, and high coulombic efficiency. Promising anode materials for lithium ion battery include silicon, graphite, and alloy compounds, as shown in Fig. 2.5.

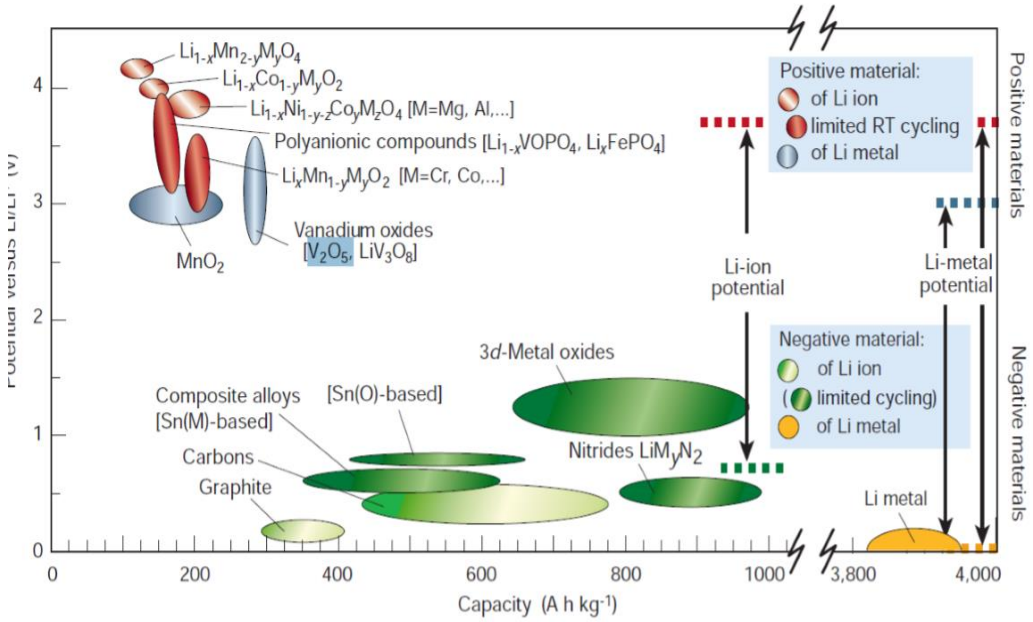

Fig. 2.5 Voltage versus capacity for cathode and anode electrode materials.

Similarly, promising anode materials for the sodium ion battery have been rapidly developed over the past few decades. The anode material extend from alloy compounds to phosphides, transition metal oxides, and carbonaceous materials, as shown in Fig. 2.6. The specific energy density of a sodium full cell can reach 350 Wh kg^{-1}. Among all the anode materials for the sodium ion battery and lithium ion battery, alloy compounds deliver the highest capacity, and they also have the highest energy density in the sodium full cell, although the huge volume changes during charge and discharge processes will result in rapid capacity decade, which damages the electrochemical performance.

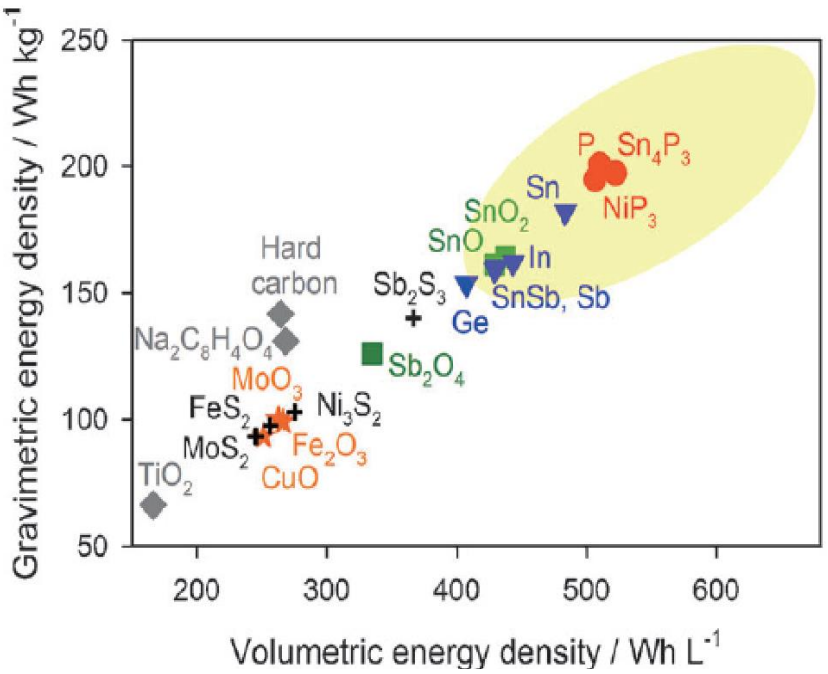

Fig. 2.6 Average gravimetric energy density versus volumetric energy density for various negative electrode materials for the sodium ion battery.

2.2.1 Carbon materials

The best commercialized carbon material date in the lithium ion battery is graphite, which has a capacity of 372mAh g^{-1} and is suitable for Li^+ ion insertion or intercalation into its hexagonally bonded sheets [8] and forms LiC_6 at the low voltage of 0.1 V. In addition, the diffusion coefficient of graphite is below 10^{-6} cm^2 s^{-1}. Apart from graphite, there are different carbon materials with various structures, such as amorphous carbon, hard carbon, porous carbon, carbon nanotube (CNT) and two-dimensional (2D) carbon. For example, CNT, which has a high surface activity allowing lithium ion insertion between the layers, has a high capacity of 500 mAh g^{-1} [9-10]. The two-dimensional graphene is a promising anode material, which consists of multilayers of honeycomb lattice and has the highest mechanical strength, high electrical conductivity, and high carrier mobility, has along with a high reversible capacity of 540-1000 mAh g^{-1} as anode material in the lithium ion battery[11-13]. Porous carbon materials are divided into three types, microporous carbon, mesoporous carbon material, and the nanoporous carbon material, by the sizes of the pores. Porous carbon has demonstrated excellent electrochemical performance in lithium ion batteries, and the nitrogen-doped porous carbon anode material even delivers a high capacity of over 900 mAh g^{-1} after 600 cycles[14].

As has mentioned above, graphite is already commercialized in lithium ion batteries. Nevertheless, it is impossible to form NaC_6 compound because the sodium ions cannot intercalate or insert themselves into the layers of graphite.

Hard carbon (HC) is composed of disordered graphene-like layers, as shown in Fig. 2.7. The insertion and extraction of sodium ions into/from hard carbon at room temperature

were first reported early in this century. Glucose was carbonized to form HC, and the as-prepared material delivered a high capacity of 300 mAh g^{-1}. In 2012, Pouronch and his group prepared HC from sugar pyrolysis, and it also delivered a high reversible capacity of over 300 mAh g^{-1} even after 120 cycles, as shown in Fig. 2.8 [15].

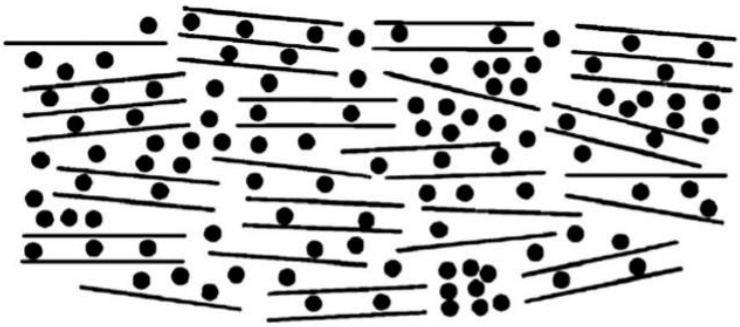

Fig. 2.7 Model of Na^+ filled hard carbon.

The mechanism of lithium ion insertion into hard carbon was investigated by Dahn's group[16-17] in the last century, and the mechanism of sodium ion insertion into hard carbon is similar[18]. There are two stages of sodium ion insertion: the plateau at 0.1 V is corresponded to the Na^+ inserted into the nanovoids, and the sloping range from 0.1-2 V is assigned to the Na^+ ions inserted into the disordered graphene layers.

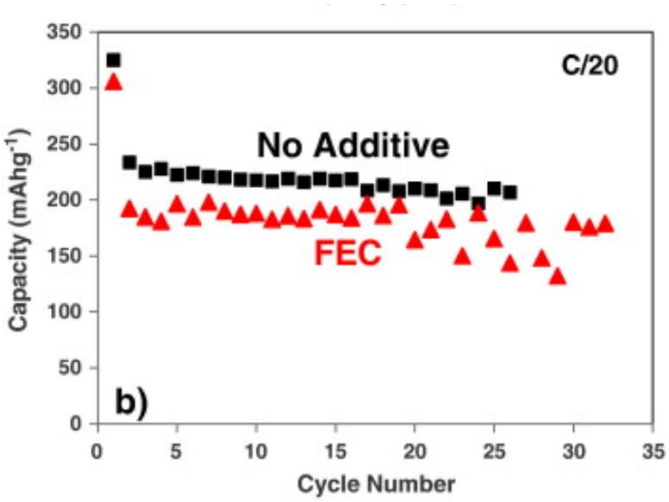

Fig. 2.8 The cycling performance of hard carbon [15].

2.2.3 Silicon based materials

The rechargeable lithium battery is a promising energy storage device used in mobile phones, cars, and power system. The choice of promising anode material has become the worldwide focus of prominent research groups in the battery field. Graphite is a commercialized low-cost, scalable production anode material with low average voltage and long cycling life. Its specific capacity is only 375 mAh g^{-1}, however. Thus, finding a good substitute anode material is crucial to the development of the lithium ion battery.

Alloy elements have high theoretical capacities. Group IV elements that can be alloyed with lithium or form compounds with it are especially promising and the most studied. Fig.2.9 shows the crystal structures and theoretical capacities of Group IV elements. Since Pb is toxic and harmful, and Ge is expensive, Si and Sn might be more promising, and the structures and comparison can be seen in Fig. 2.9[19].

(a)

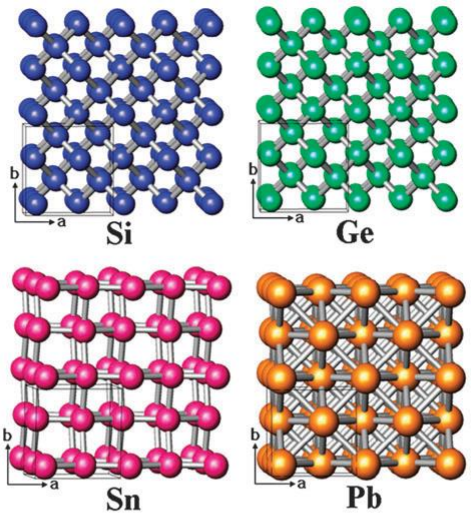

(b)

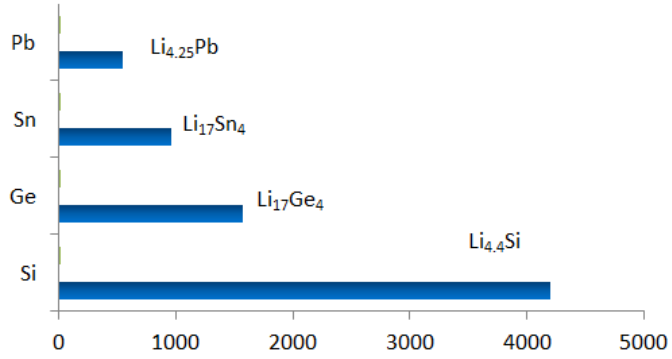

Fig. 2.9 Crystal structures (a) and theoretical capacities (b) of the elements Pb, Sn, Ge, Si.

Silicon has the highest capacity (4200 mAh g^{-1}) as anode material in the lithium batteries[20] The discharge potential of silicon is 0.2 V, which is lower than for most elements in the IVA and VA groups[21]. Because of these two points, silicon is a promising anode material. The main challenge for using it is finding a way to lower the volume changes during charge and discharge, which can result in in pulverization and a consequent loss of electrical contact. This occurs during the lithiation reaction involving the two phases (crystal silicon and amorphous silicon). Because of it, the capacity will fade rapidly. This issue is obstructing the application of silicon-based materials [9]. Many methods have been used to solve this problem. There are basically three ways to overcome the volume changes. One way is to combine silicon with carbon materials. Another way is to prepare silicon-based alloy. The third way is to prepare nanoscale pure silicon. These three methods can also be used together.

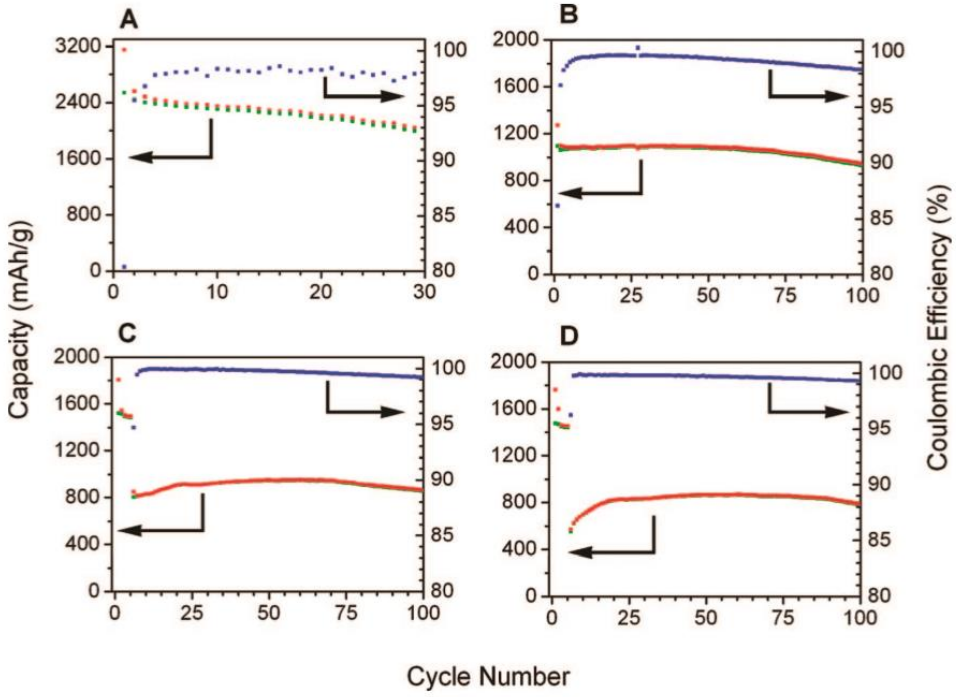

Fig. 2.10 Cycling performance of core-shell NWs at different current densities.

Cui[22] and his group fabricated silicon nanowires (NWs), which retained their capacity for 10 cycles. The nanowires can accommodate large volume changes without pulverization. Cui[23] and his group then prepared crystal-amorphous core-shell silicon nanowires, which had high capacity of 1000 mAh g^{-1} and retained capacity of 860 mAh g^{-1} in the 100th cycle, as can been seen in Fig. 2.10. The good performance is due to the core-shell nanowire structure with crystal silicon on the inside and amorphous silicon on the outside. Based on their study, this structure can efficiently provide pathways for electrons, and the crystal on the inside can remain mechanically stable. Jaephil Cho [24] and his group fabricated three-dimensional (3D) porous silicon particles by thermal annealing and etching. With their 200 nm size and pores 40 nm in diameter, the silicon particles showed 99% capacity retention in the 100th cycle, as shown in Fig. 2.11 The reason for this superior performance is that the nanostructure greatly improves the

lithium ion transportation. In addition to the nanostructure effect on the electrochemical performance, the size of particles also has a great effect. Jaephil Cho[25] and his group prepared nanoscale silicon particles in different sizes. Their results indicate that the 10-nm size particles have the best electrochemical performance compared to the 5 nm and 20 nm.

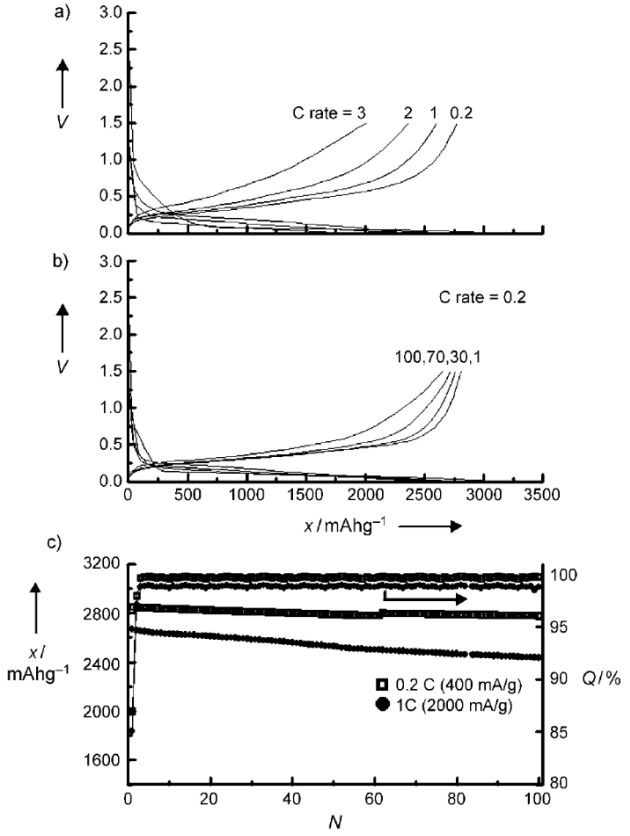

Fig. 2.11 Charge-discharge curves at different rates (a), the discharge and charge curves for different cycles at the rate of 0.2 C (b), and the cycling performance (c) of the 3D porous Si anode material.

Although the electrochemical performance of silicon has been improved by designing different nanostructures and controlling the particle size, the huge volume changes have not been effectively alleviated. Therefore, silicon-carbon composites are being

extensively investigated. Currently, several different carbon materials are used in preparing silicon-carbon composites.

Carbon nanotube is an allotrope of graphite, which consists of a one-dimensional (1D) tube of graphite sheet. It has high conductivity, a high Young's modulus, and high strength. The capacity of CNTs in the lithium ion battery is 300−600 mAh g^{-1}, which is higher than that of graphite. Apart from its excellent mechanical properties, CNT has several advantages in lithium ion batteries. When combined with nanoparticles, CNT can work as a glue-like matrix and keep the structure intact when the nanoparticles are alloyed, since it can keep the particles attached to the current collector and it has high conductivity [8- 26].

Based on the Seung M. Oha group's research, Si/CNTs composite electrode delivers better electrochemical performance than pure Si. They suppose that this is because the CNTs with spaces between them wrap up the Si particles and can serve as a conductive buffer to accommodate the volume changes. Furthermore, the CNTs also improve the electronic conductivity.

In contrast to the Seung M. Oha's group, which used CNTs to wrap the silicon particles, N. Kumta er al,[27-28] and Barbara Laïk [29] used the chemical vapor deposition (CVD) method to prepare the vertically aligned CNTs (VASCNTs) and then dispersed the silicon particles onto the CNTs. The electrode delivered stable cycling performance and high rate performance.

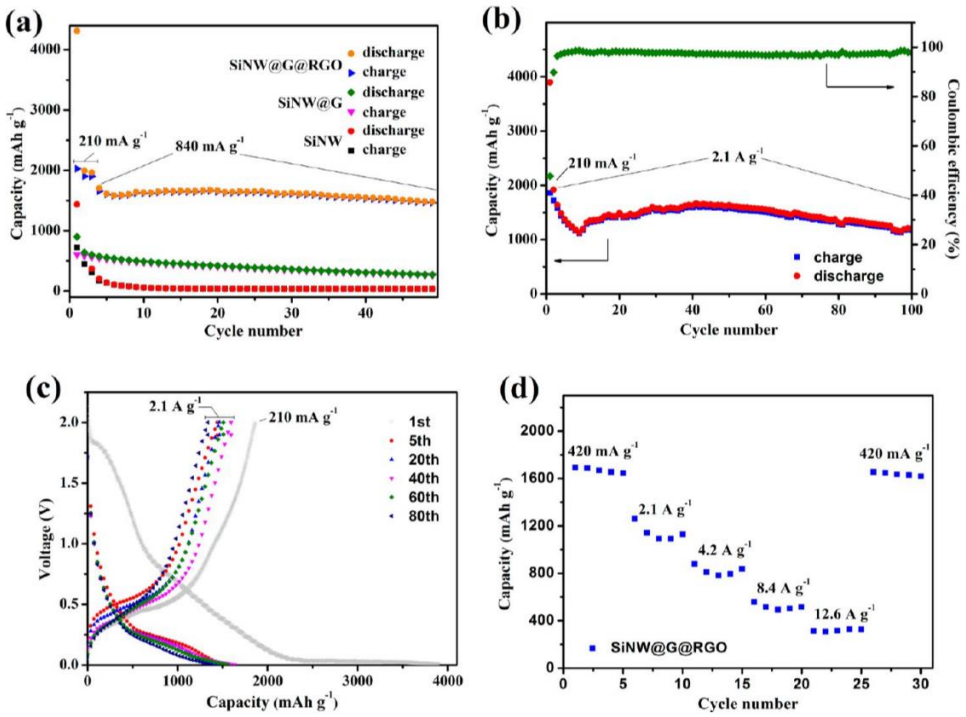

Fig. 2.12 The electrochemical performance of f SiNW@G@RGO composite.

Since K. S. Novoselov[30] first discovered graphene, a single-atomic-layer carbon sheet, it has been extensively investigated. Graphene has many unique characteristics. For example, the Young's modulus is 1 TPa, and because of the ambipolar electric field effect, it has high carrier mobility [31]. In addition, when silicon is wrapped by graphene, the solid electrolyte interphase (SEI) will form on the layer of graphene instead of growing directly on the silicon, which will be beneficial for forming a stable SEI layer [32].

Yu-Guo Guo [33], Shu-Lei Chou [34], and Hongfa Xiang [35] have prepared silicon-graphene composites which delivered good electrochemical performance. From the scanning and transmission electron microscope (SEM and TEM) images, the silicon particles are coated onto the graphene or wrapped by the graphene. The graphene has capacity of 304 mAh g^{-1} in lithium ion batteries, as in reference [34].

During the Li-ion insertion and extraction into and out of the composite, graphene can alleviate the volume change, prevent aggregation, and also improve the conductivity, although it still has some disadvantages. The silicon particles are hard to disperse in a homogeneous way, and the thin layers of graphene are hard to prepare, thus resulting in low lithium ion diffusion [33]**.** Bin Wang [36] and his group prepared a SiNWs@RGO composite by combining silicon nanowires with reduced graphene oxide (RGO). The composite delivered extraordinary electrochemical performance, as shown in Fig. 2.13. The specific capacity of the as-prepared composite could reach over 1600 mAh g^{-1} at a high current density of 2.1A g^{-1}, and even after cycling for over 100 cycles, the retained capacity was 1280 mAh g^{-1}. The excellent electrochemical performance is due to the highly flexible nature of the graphene, which efficiently accommodates the volume changes. In addition, graphene sheaths in the composite can form a continuous electroconductive network, which effectively improves the conductivity of the silicon composite.

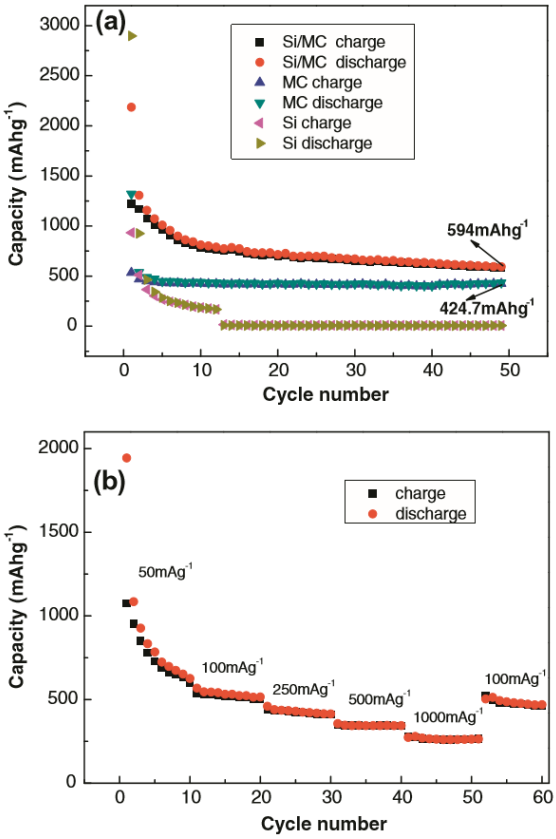

Fig. 2.13 The electrochemical performance of Si/MC composite: (a) MC and Si at a current density of 100 mA g^{-1}, (b) rate performance of composite.

Apart from using CNTs or graphene, many other carbon materials or carbon composites are used to prepare silicon-carbon composites. Daobin Mu [37] and his group used mesoporous carbon to combine with silicon. The capacity of the composite remained at about 600 mAh g^{-1} after cycling for 50 cycles, as shown in Fig. 2.14. The mesoporous carbon (MC) consists of disordered carbon materials with pores around 40-50 nm in size, and silicon particles are deposited in the pore channels of mesoporous carbon or on its surface. Because the Si particles are accommodated in the pores, the volume expansion is hindered. Nevertheless, this structure also results in low coulombic efficiency. Amorphous carbon-silicon composite [38] was prepared by in-situ spray

pyrolysis. The silicon particles were 10-100 nm in size and covered with a layer of amorphous carbon 10-40 nm in thickness, as shown in Fig. 2.15. The carbon layer can efficiently avoid the aggregation of silicon particles and accommodate the volume expansion. The amorphous carbon results in high irreversible capacity for the first 20 cycles.

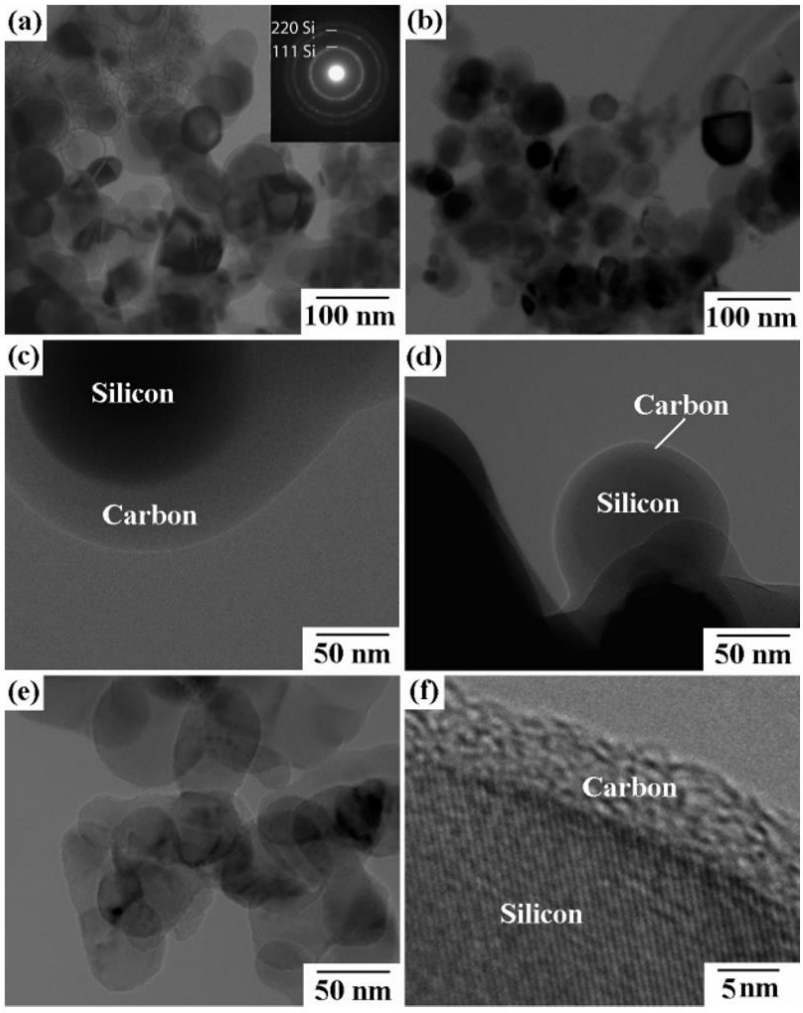

Fig. 2.14 TEM images of silicon, with the inset showing the selected area electron diffraction (SAED) pattern (a), and carbon-coated silicon (b-f).

Using carbon material to improve the electrochemical performance of silicon has its drawbacks, however. The volumetric capacity of silicon is 8322 mA h·cm^{-3}, and one

reason for the high volumetric capacity is the high density of silicon compared to graphite.

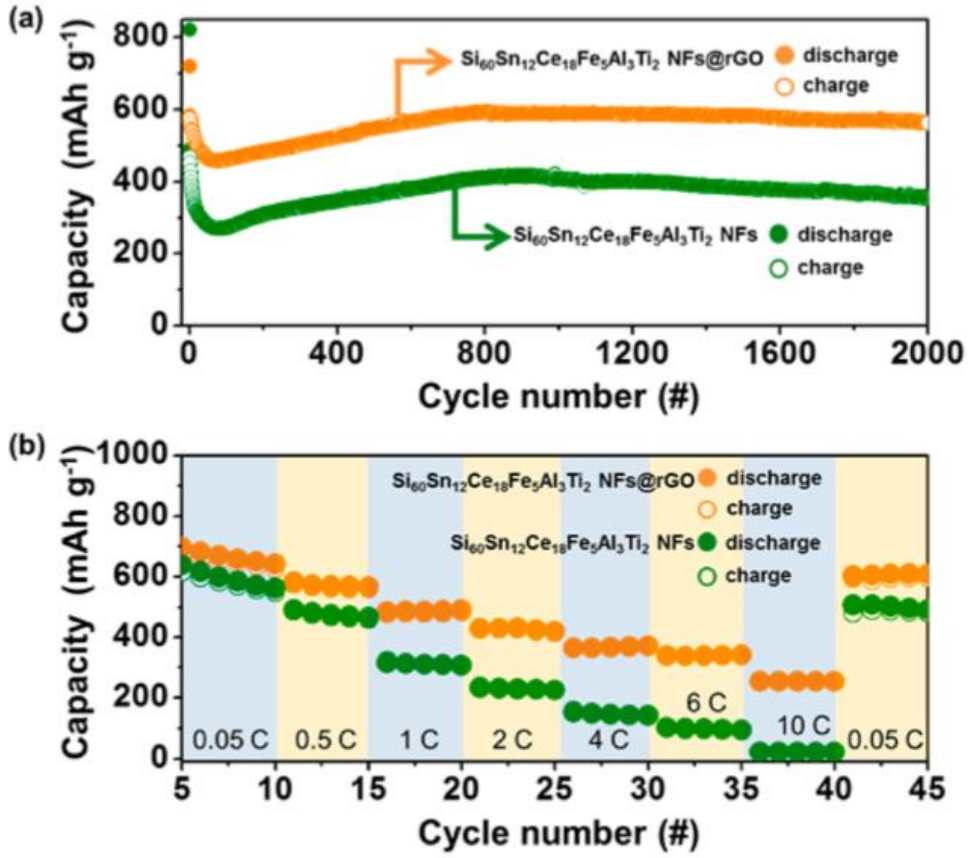

Fig. 2.15 The cycling performance (a) and the rate performances (b) of $i_{60}Sn_{12}Ce_{18}Fe_5Al_3Ti_2$ NFs and $Si_{60}Sn_{12}Ce_{18}Fe_5Al_3Ti_2$ NFs@rGO.

Apart from using carbon materials to alleviate the volume changes of silicon during charge and discharge processes, forming silicon-based alloy compounds or composites is also an efficient method. Inactive materials, such as Ni [39-40], Cu [41-43], Co [44], and Fe [45-46], and active metals, such as Mg [47], Al [48], Zn [49], and Sn [50-53], can be alloyed with silicon. Using these metals can improve the electrical conductivity and alleviate the volume changes, so that they can improve the electrochemical performance compared to pure

silicon. In addition, an active metal can hinder the formation of two-phase regions, which can block pulverization. When silicon and other metallic elements are combined in a proper ratio, they will form an isotropic amorphous phase, which is beneficial to stable cycling performance and rate capacity[32]. As shown in Fig. 2.16, the alloyed composite combined with graphene delivered extraordinary electrochemical performance in a lithium ion battery. Furthermore, since metal materials have high density compared to carbon, the volumetric capacity of the alloy will be higher.

It was reported that inactive materials, mostly transition metals, in silicide can act as an inactive matrix former that can connect the silicon particles after cycling.

Nae-Lih Wu [40] and G.X. Wang [39] prepared NiSi-composite with nanocrystals of NiSi alloy through a simple ball milling method, and the samples delivered high gravimetric capacity of 1180 mAh g^{-1} and volumetric capacity of 7050 mA h ml^{-1}. Because silicon has a high capacity of 4000 mA h g^{-1}, both the composite and the compound have high capacity. The reaction between Li-ions and NiSi alloy can be summarized as follows:

$$xLi^{+} + xe^{-} + NiSi \rightarrow Li_xSi + Ni_2Si$$

This reaction indicates that Ni is inactive and has no capacity in the lithium ion battery. The transition metals Co, Cu, and Fe have similar characteristics and can react with Si to form silicates. Sung-Man Lee prepared Fe_xSi [54] ($0.25 < x < 1$) alloy through the ball-milling method and Co-Si [44] alloy through the co-deposition method. When the Fe_xSi was combined with graphite, it delivered a high reversible capacity of 600 mAh g^{-1}. Yu-Guo Guo [41] prepared Cu-Si nanotube arrays by growing Cu cores directly on the

current collector, which delivered a high capacity of 1660 mAh g^{-1}, and after cycling for 100 cycles, it still delivered 1560 mAh g^{-1}.

Silicon in alloys with other active metals has been extensively studied over the past few years. Compared to inactive metals, the active elements can also serve as a conductive matrix to hinder the volume expansion of silicon. In addition, some of the active metals can suppress the formation of binary phase, and some of the active metals also hinder the formation of $Li_{15}Si_4$ crystal, which is harmful to cycling performance [55]. Among all the active materials, tin is the most promising one. Sn is an active metal in the lithium ion battery, which has a high theoretical capacity of 990 mAh g^{-1}. When Sn is alloyed with Si, it can help to restrict the formation of $Li_{15}Si_4$ crystal. Fig. 2.17 shows the electrochemical performance of the SiSn/C nanoparticles.

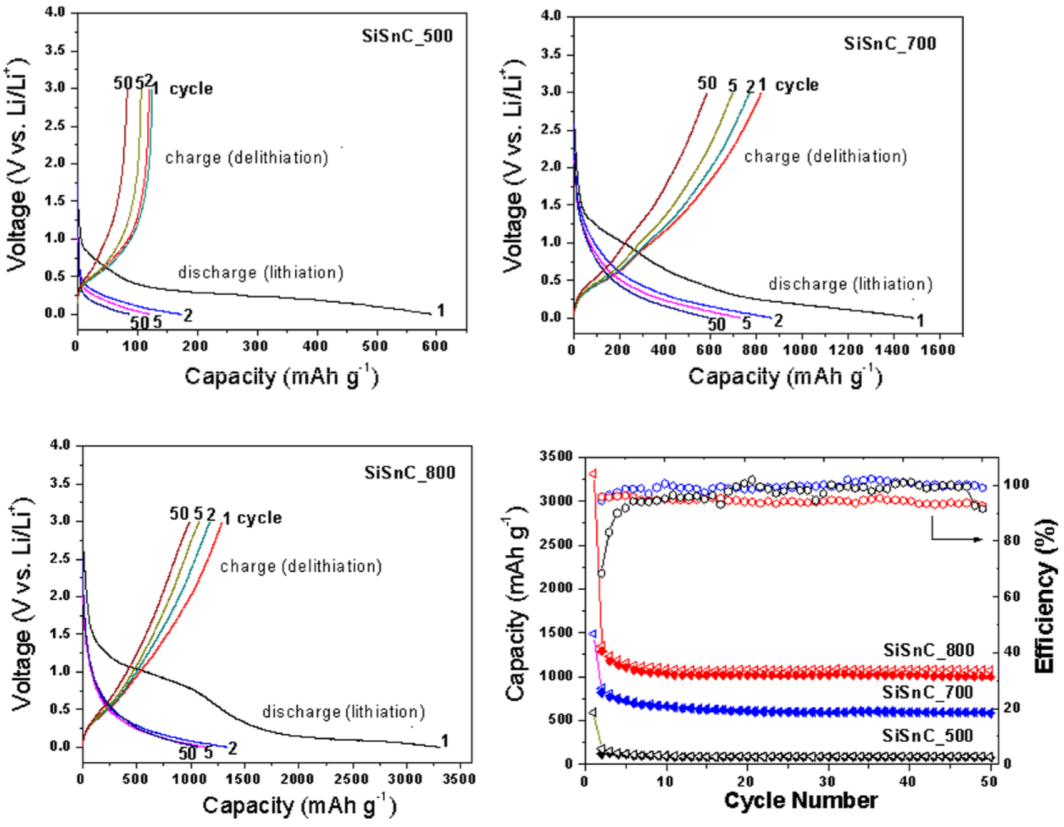

Fig. 2.16 Electrochemical performance of SiSn/C composites.

R. Dahn [52] and his group have done considerable work on Si-Sn alloy. The material that they obtained had a high capacity of 3500 mAh g^{-1}. Gang Yang [51] and his group also prepared Sn-Si nanocomposite, which had a high capacity of 1073 mAh g^{-1} after cycling for 50 cycles. Nam-Soon Choi [50] prepared one-dimensional Si/Sn nanotubes and nanowires, which also had very good electrochemical performance.

Thus, silicon and silicon-based compounds and composites are promising anode materials for the lithium ion battery. They might be suitable substitute materials for graphite. Nanostructured silicon material combined with carbon material, and active and inactive metal might have the best electrochemical performance.

2.2.4 Phosphorus based materials

P has three main allotropes: red, white, and black. White P has a low ignition point, which makes it hard to apply. Black P has a puckered layer structure, with each atom bonded with another three, with the individual layers connected by van der Waals bonds. The structures of phosphorus's three allotropes are shown in Fig. 2.18.

Black P provides an interstitial space along the (0k0) plane for lithium-ion transport. Based on theoretical calculations, the lowest energy barrier for sodium-ion diffusion is 0.18 V along the phosphorene layer.

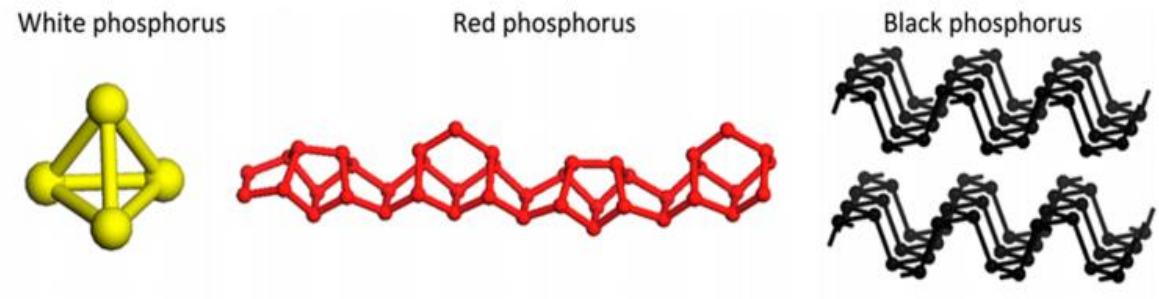

Fig. 2.17 The structures of the three allotropes of phosphorus.

The sodiation mechanism first involves intercalation into interlayers, but when the Na concentration is above $Na_{0.25}P$, the mechanism will change to alloying with P atoms[56]. Black P [57] has capacity of 1279 mAh g^{-1} in a lithium ion battery, with capacity of more than 600 mAh g^{-1} over 100 cycles. The interlayer space of black P is 5.4 Å, which is large enough to hold sodium ions. The capacity of black P in a sodium ion battery is 2035 mAh g^{-1}, although black P is very hard to synthesize, which is obstructing its application. Red P is more commercially viable. The theoretical capacity of red phosphorus is about 2600 mAh g^{-1}, and the operating window is 0.45 V, which is suitable. The main challenges for P are low electrical conductivity and large volume changes. Qian [58] reported that amorphous P has high capacity of 1764 mAh g^{-1} and higher coulombic efficiency compared to black P. Our group[59] simply mixed red phosphorus with CNTs. By this method, the capacity was increased to 2200 mAh g^{-1}. The usual method for preparing P-carbon composites is ball milling, while Chunsheng Wang's [60] group has recently prepared composites of phosphorus and single-walled CNTs (P-SWCNT composites) by a vaporization-condensation method and delivered good results.

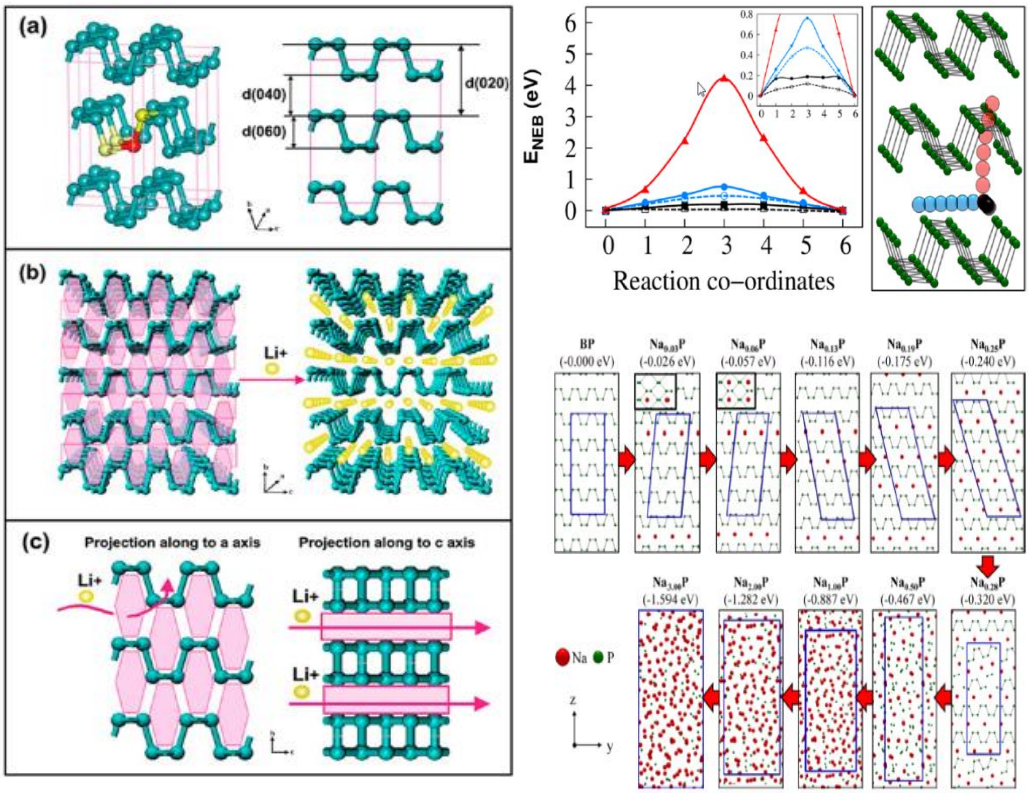

Fig. 2.18 (a) Lattice structure of black P. (b) Transport channels of lithium-ions in black P. (c) Diffusion mechanism of lithium-ions in black P based on theoretical calculations[61]. (d) Diffusion barriers for a Na atom in black phosphorus based on theoretical calculations. (e) Sodiation mechanism of black P based on theoretical calculations [56].

Although phosphorus has high capacity, its huge volume changes result in fast capacity decay. In order to alleviate the volume changes in P as anode material for lithium ion batteries, using metal elements to form compounds or composites is an efficient way. Transition metal phosphorus compounds such as $FePS_3$ and $NiPS_3$ [62] were first applied in lithium batteries as cathode materials in 1977. During the early 2000s some groups

began to study phosphides such as CoP_3 [63], FeP_2 [64], and MnP_4 [65] as anode materials in lithium ion batteries. Based on their studies, it was first proved that phosphides firstly proved can be reacted with lithium-ion in room temperature. Later on, various phosphides such as NiP_2[66], Zn_xP_2[67-68], Sn_4P_3 [69]and VP_x[70] have been greatly studied as anode materials applied in lithium battery. Based on their study, phosphides have high initial capacities but drops quickly in the following few cycles. The reaction mechanisms can be classified as follows.

Conversion reaction: $MP_x + 3Li^+ + 3e^- \leftrightarrow {}_xLi_3P + M$

Insertion reaction: $MP_y + yLi^+ + ye^- \leftrightarrow Li_YMP$

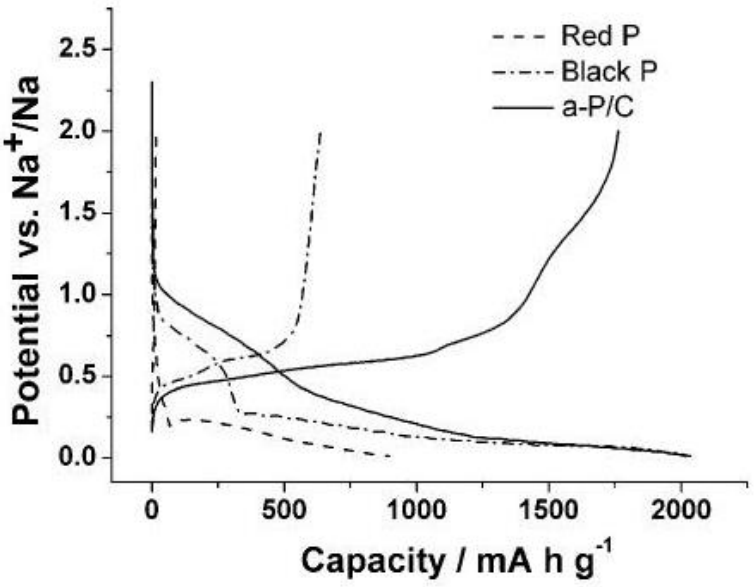

Fig.2.19 The charge-discharge curves of Red P, black P and amorphous P/C composite.

Take Cobalt phosphide for an example of conversion reaction. Some research groups have studied Co_xP as anode material in lithium battery [63, 71-72]. The capacity of Co_3P is about 500mAh g^{-1}, the mechanism equation is conversion reaction as followed: CoP_3 +

$9Li^+ + 9e^- \leftrightarrow 3Li_3P + Co$. After the first cycle, Li_3P formed and amorphous Co formed. Jun Yang's[72] group supposed that during the lithiation process there is one more reversible step that the Co_3P might convert to CoP.

Many groups[66, 73-76] have done research on Ni_xP as anode material in lithium-ion battery as well. The mechanism of lithiation of Ni_xP is different from Co_xP. Based on the study of F. Gillot [66] there are two NiP_2 polymorphs with different reaction mechanism. One is the conversion reaction in cubic NiP_2, and the other is the two steps reaction in monoclinic Ni_2P which firstly formed the $Li_{2.4}NiP_2$ phase and then converted into Li_3P. Though the mechanism of lithiation is different in the first cycle, after few cycles, the reaction will transform to conversion reaction which is beneficial to hinder the crack [19]. Phosphide has high capacity but poor cycling performance, because the low electrical conductivity of P and the huge volume change during charging and discharging process. One efficient way is to combine P or phosphide with carbon materials.

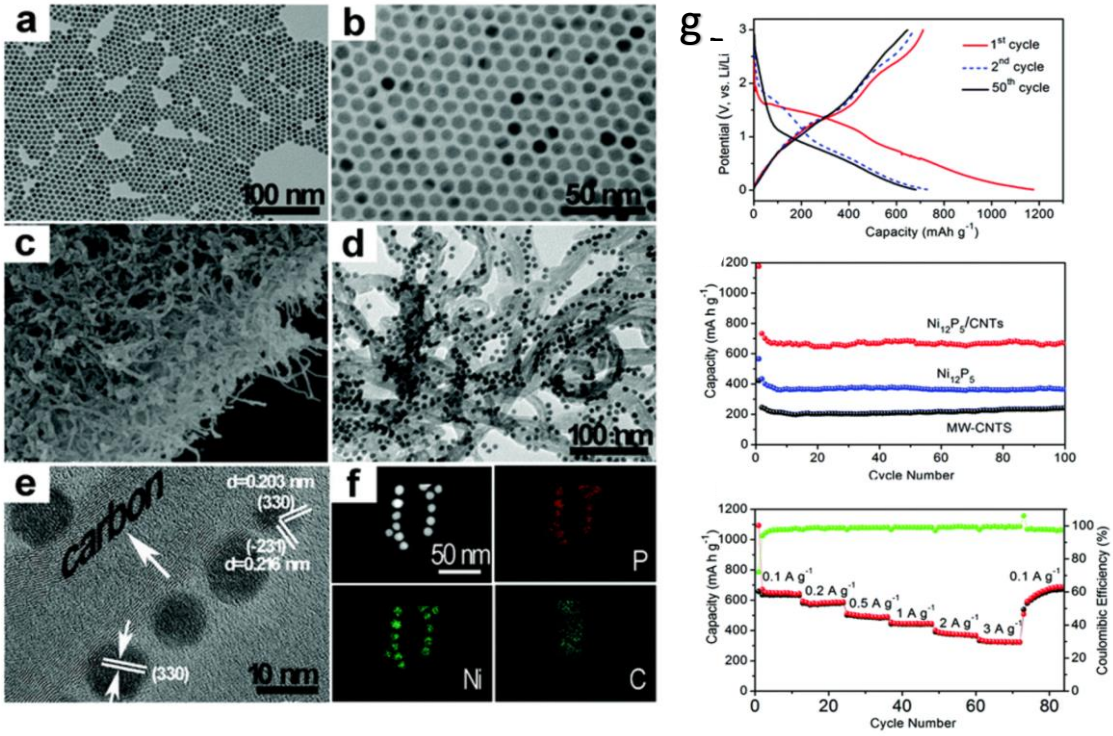

Fig.2.20 The (a) Low- and (b) high-magnification TEM image of $Ni_{12}P_5$ nanocomposites (c) low-magnification SEM, (d) TEM images, and (e) HRTEM images of the $Ni_{12}P_5$/CNT ($Ni_{12}P_5$/CNT), and (f) STEM image and STEM-EDX elemental mapping images of Ni, P and C for a typical individual $Ni_{12}P_5$/CNT, ; and (g) charge-discharge, cycling, and rate performances of $Ni_{12}P_5$/CNT composite.

CNT [77] and graphene[78-80], have been widely used. Carbon nanotubes have been applied to improve the electrochemical performance of P-based materials. Carbon nanotube has high electrical conductivity and can restrict the aggregation of particles. Because of the excellent properties of CNT, Chunde Wang [77] used a simple one-pot hot-solution method to synthesize $N_{12}P_5$ composite, which presented a high initial capacity of over 1100 mAh g^{-1}, and after cycling for 50 cycles, the coulombic efficiency remained 95%, as shown in Figure 2.21. Graphene also has excellent electrical conductivity. Due to the

excellent electrical conductivity of graphene, phosphides such as Ni_2P [79] and CoP_2 [80] perform better when combined with graphene. The Ni_2P/graphene composite in Yi Lu's research presented a capacity of 450 mAh g^{-1} after cycling for 50 cycles, which was much better than the previous report of 400 mAh g^{-1}; Aolin Lu's CoP_2/graphene nanocomposite presented a stable capacity of over 800 mAh g^{-1},which is much higher than the theoretical capacity.

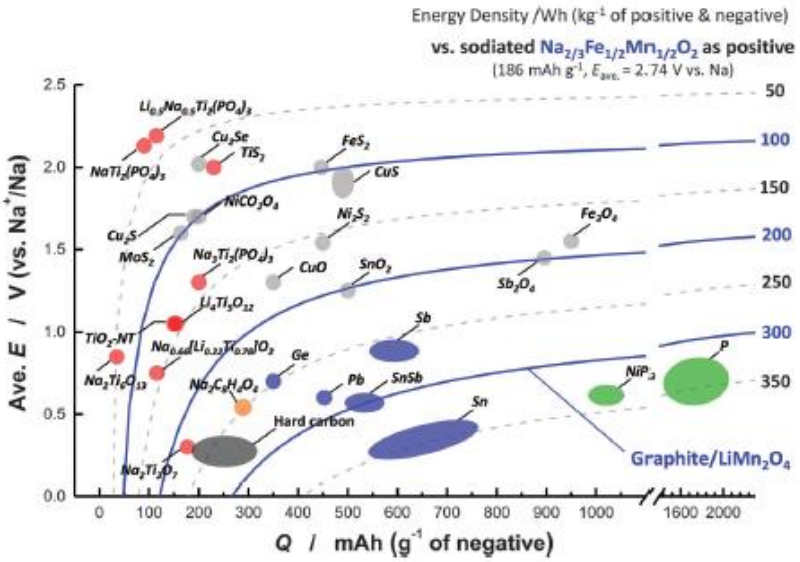

Figure 2.21 Average voltage and energy density versus gravimetric capacity for various negative electrode materials for NIBs [81].

Graphite is performing well as anode material in lithium ion batteries, but it has no capacity in the sodium ion battery. Among the active anode materials in the lithium ion battery, silicon has the highest theoretical capacity in the lithium ion battery, but it has no capacity in the sodium ion battery at room temperature. As shown in Figure 2.22, phosphorus and phosphide have the highest energy density and capacity compared to carbonaceous materials, oxides, and sulfides, while among the other alloy materials,

phosphorus is the most promising anode material. There are two theoretical reasons for this: firstly, the redox potential of a sodium ion inserted into phosphorus is about 0.4 V *vs.* Na/Na^+, whereas the redox potential of a lithium ion inserted into phosphorus is about 0.8 V *vs*. Li/Li^+. The lower redox potential results in higher energy density, so phosphorus-based anode has higher energy potential. This potential is not very low and higher than that of hard carbon, which will prevent Na crystals from forming. Secondly, it has a high theoretical capacity of 2567 mAh g^{-1} in the sodium-ion battery. The first two groups studying phosphorus in sodium batteries were Jiangfeng Qian's [58] group and Youngjin Kim's [82] group. Qian's work resulted in an amorphous-carbon composite delivered a capacity of 1764 mAh g^{-1} and a retained capacity of about 1000 mAh g^{-1} after cycling for 80 cycles. Youngjin Kim's group also prepared a phosphorus/carbon composite, which delivered a high capacity of 1890 mAh g^{-1} and had very stable performance for 30 cycles. The mechanism of sodiation of P is similar to the reaction in the lithium-ion battery. The cyclic voltammetry (CV) curves indicate the mechanism as follows:

$P + 3Na^+ + 3e^- \leftrightarrow Na_3P$

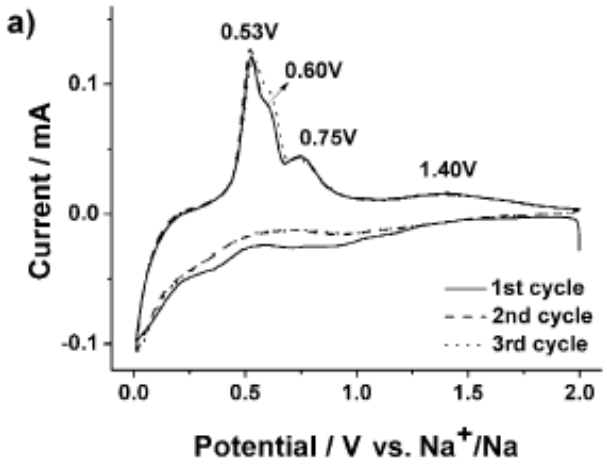

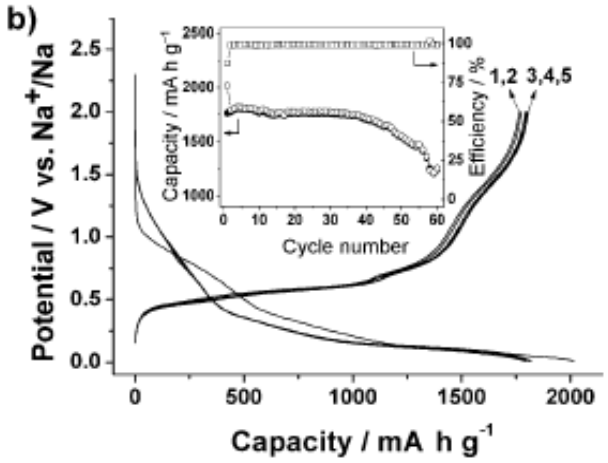

Fig.2.22 (a) CV curves for the first 3 cycles and (b) charge-discharge curves for the first 5 cycles for amorphous P/carbon composite, with the inset showing the cycling performance [58].

The main problem that is obstructing the application of red phosphorus in the sodium ion battery is also the huge volume change, resulting in poor cycling performance. There are two main methods to solve this problem: combining with carbon materials and using active or inactive metals to form phosphides.

Our group [59] has used CNT to improve the electrochemical performance of red phosphorus and had excellent results, as shown in Fig. 2.24.

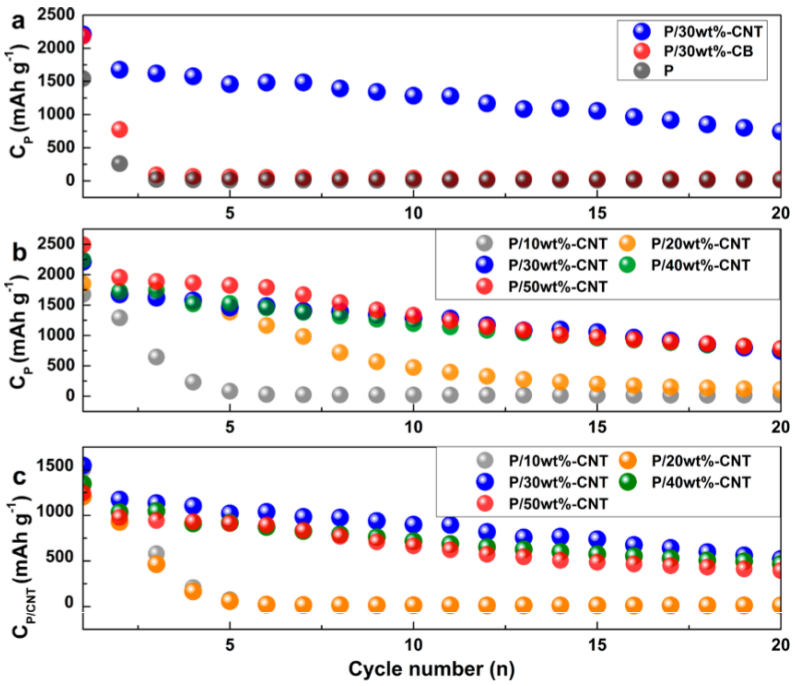

Fig. 2.23 Cycling performance of (a) P/CNT composite and P/carbon black composite, and (b, c) the specific capacity calculated based on the weight of P and of P/CNT composites.

By only adding the CNT by a simple hand-grinding method, the composite reached a high reversible capacity of 1675 mAh g^{-1} and cycled in a stable manner for 10 cycles. The CNT can restrict the volume change, as shown in Fig 2.25.

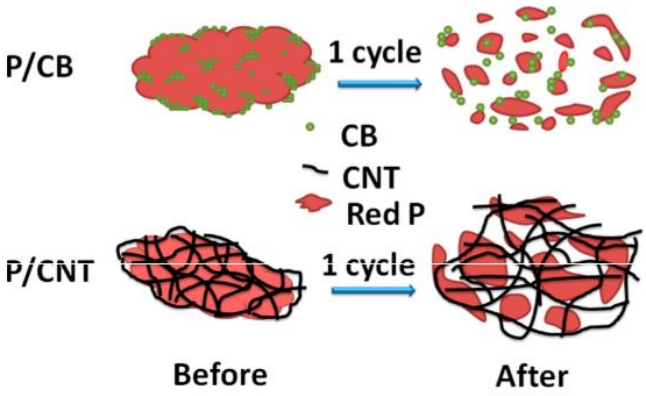

Fig. 2.24 Mechanism of CNTs that restricts the volume change of P.

Jiangxuan Song 's [78] group used graphene as a conductive matrix to restrict the volume change and improve electrical conductivity. Based on their study, the phosphorus/graphene hybrid delivered a high reversible capacity of over 2000 mAh g^{-1} and retained 1700 mAh g^{1} after 60 cycles.

Inspired by phosphides applied in the lithium ion battery, various phosphide and P-based composites have been applied in the sodium-ion battery. The mechanism by which the active metal restricts the volume change of phosphorus is shown in Fig. 2.26.

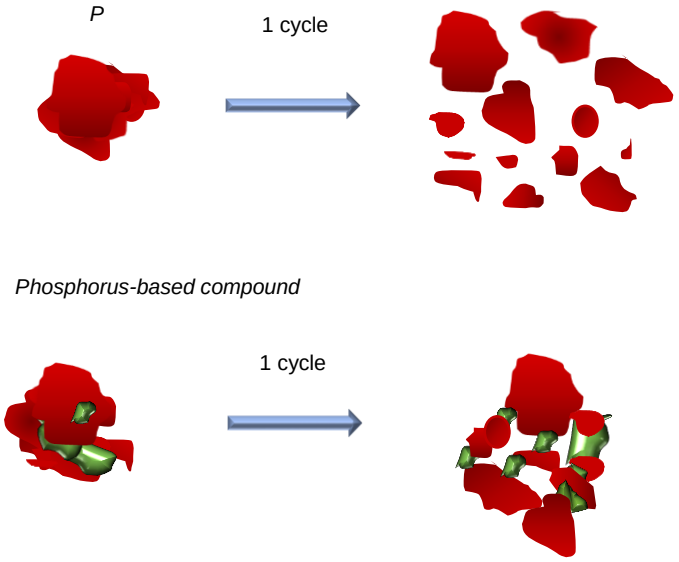

Fig 2.25 The volume change model of phosphorus anode material and phosphorus-based compound during cycling.

SnP_x is one such phosphide that has been investigated in detail. Sn is an active metal that has a theoretical capacity of 847 mAh g^{-1} in the sodium ion battery, forming $Na_{15}Sn_4$. In addition, Sn has high electrical conductivity, which can improve the conductivity of the compound, thus alleviating the capacity fading. Weijie [83], Youngjin Kim [84], and Xiulin Fan [85] have studied SnP_x compound and composites. Weijie prepared $Sn_{4+x}P_3$ @ amorphous Sn-P composites by low energy ball milling. The composite has

a Sn-P amorphous layer that covers the $Sn_{4+x}P_3$ particles, which maintains the stability of the cycling performance. Youngjin Kim and Xiulin Fan also used the ball-milling method to prepare Sn_4P_3 and SnP_3/C composite. The Sn_4P_3 compound prepared by Youngjin Kim delivered a high reversible capacity of 718 mAh g^{-1} and cycled for 100 cycles with little capacity decay. The SnP_3/C composite synthesized by Xiulin Fan performed well in the sodium-ion battery with high initial capacity of 1131 mAh g^{-1} and exhibited over 92% retention over 100 cycles. Based on their study, the final sodiation mechanism of SnP_x can be concluded to be as follows:

$$SnP_x + (3x+4)Na^+ + 3x + 4\ e^- \leftrightarrow Na_4Sn_{15} + xNa_3P$$

CoP has also been studied in sodium-ion batteries. Our group [86] prepared CoP by using a simple ball-milling method. The inactive Co act as a conductive matrix to alleviate the volume changes. The electrode could deliver a high capacity of 700 mAh g^{-1}. The sodiation mechanism of CoP is similar to the lithiation process of CoP. During the discharging process, the CoP decomposed, and then the sodium-ions reacted with P. The equation after the initial discharge process is as follows:

$$CoP_3 + 9Na^+ + 9e^- \leftrightarrow 3Na_3P + Co$$

In short, phosphorus-based compounds and composites have high capacity of over 2500 mAh g^{-1}in lithium and sodium ions batteries, and in addition, the redox potential of a sodium ion inserted into phosphorus is about 0.4 V *vs.* Na/Na^{+}. The lithiation and sodiation mechanisms can be classed into two categories: conversion reaction and insertion reaction. The main challenge for application is the huge volume change during cycling and the poor electrical conductivity. There are basically two methods to solve

the problem: combining with carbon materials and using active or inactive metals to form phosphides. The results demonstrate that phosphorus-based compounds and composites are promising anode materials.

2.3 Electrolytes

The electrolyte is a crucial element in both the lithium ion battery and the sodium ion battery. A suitable electrolyte should exhibit the following characteristics: large electrochemical and thermal stability window; high ionic conductivity and low toxicity; no reaction with the anode and cathode materials.

Table 2.1. The common electrolyte salts used in sodium ion batteries.

Salt	Anion chemical structure	M_w [g mol^{-1}]	T_m [°C] (Li-salt)	σ [mS cm^{-1}][a] (Li-salt)
$NaClO_4$		122.4	468 (236)	6.4 (5.6)
$NaBF_4$		109.8	384 (293)	(3.4)
$NaPF_6$		167.9	300 (200)	7.98 (5.8)
NaTf		172.1	248 (>300)	(1.7)
NaTFSI	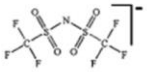	303.1	257 (234)	6.2 (5.1)
NaFSI	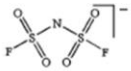	203.3	118 (130)	

[a] 1 M NaX (LiX) in PC at 25 °C.

For the lithium ion battery, the most common and safe salt is $LiPF_6$, since other salts such as $LiClO_4$, $LiAsF_6$, and $LiBF_4$ are explosive or problematic on the negative side, or poisonous. The ionic conductivity of a $LiSO_3CF_3$ containing solution is low [87]. For the sodium ion battery, the most common salts are shown in Table 2.1. The most

suitable sodium ion salts also deliver high ionic conductivity, low toxicity, and electrochemical safety and stability.

Another important consideration for the most suitable electrolyte is the solvents. For the lithium ion battery and the sodium ion battery the common solutions are similar, mostly organic carbonates such as dimethyl carbonate (EC), diethyl carbonate (DEC), ethyl-methyl carbonate (EMC), etc. Table 2.2 shows the melting, boiling, and flash points, the relative dielectric constant, and the viscosity of the solutions.

Table 2.2. Characteristics of the common electrolyte solutions.

Solvent	T_m (°C)	T_b (°C)	T_f (°C)	η (cP) 25 °C	ε 25 °C	AN (DN)
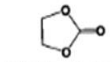 Ethylene carbonate (EC)	36.4	248	160	1.9 (40 °C)	89.78	(16.4)
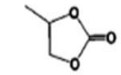 Propylene carbonate (PC)	−48.8	242	132	2.53	64.92	18.3 (15.1)
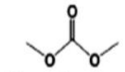 Dimethyl-carbonate (DMC)	4.6	91	18	0.59	3.107	
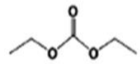 Diethyl carbonate (DEC)	−74.3	126	31	0.75	2.805	(16.0)
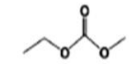 Ethylmethyl carbonate (EMC)	−53	110		0.65	2.958	
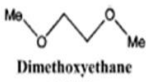 Dimethoxyethane (DME)	−58	84	0	0.46	7.18	10.9 (18.6)
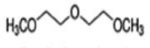 Diethyleneglycol dimethylether (Diglyme)	−64	162	57	1.06	7.4	9.9 (19.2)
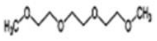 Triethylene glycol dimethyl ether (Triglyme)	−46	216	111	3.39	7.53	10.5 (14)

Additives are another important component of a suitable electrolyte. In the case of the lithium ion battery electrolyte, the additives are supposed to improve the formation of the SEI, protect the cathode, block the decomposition of the salt, or stop corrosion. There are numbers of additives available for application in lithium ion battery electrolyte, such as vinylene carbonate (VC), lithium bis(oxolato)borate (LiBOB), lithium oxalyldifluoroborate (LiODFB), cyclohexane, etc. [88].

The functions of additives in sodium ion electrolyte are similar to those of the additives in the lithium ion battery.

Some of the additives used in lithium ion batteries were also studied for sodium ion batteries, including vinylene carbonate, ethylene sulphite, and fluorethylene carbonate. These additives can efficiently help to form stable SEI layers. The mechanism of the active metal hinder the volume change of phosphorus is shown in Fig 2.27.

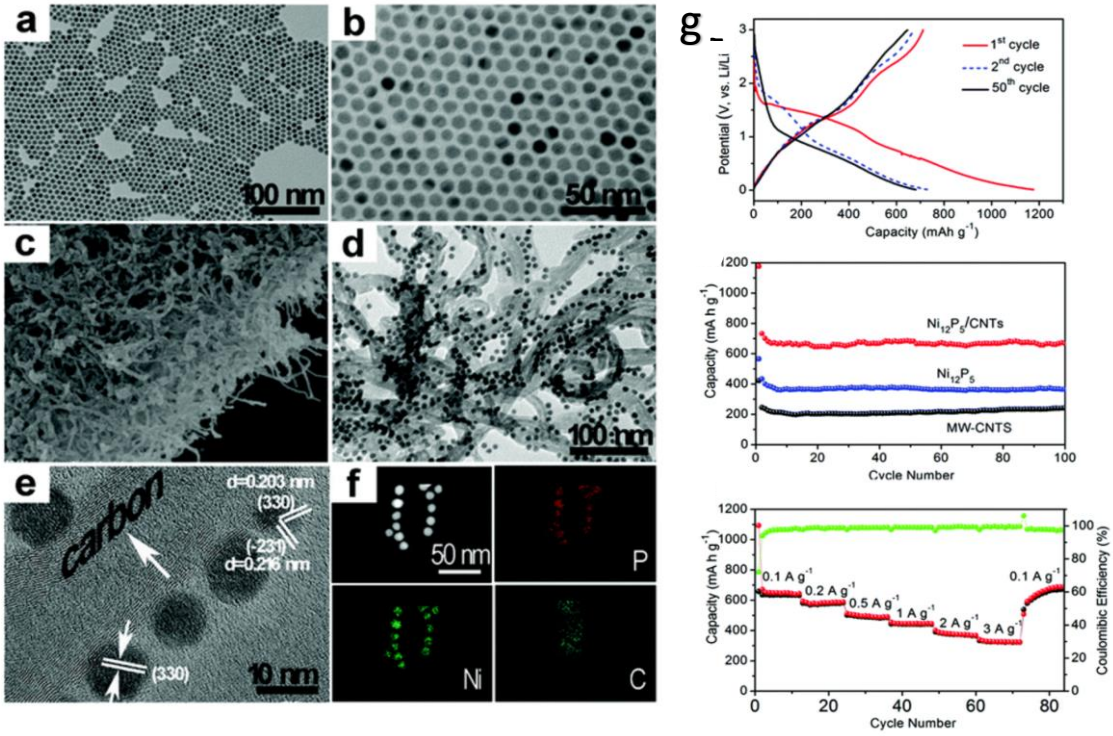

Fig 2.27 The volume change model of anode materials of phosphorus and phosphorus-based compound during cycling.

SnP_x is one of the phosphide that has been greatly investigated. Sn is an active metal has theoretical capacity of 847mAh g^{-1} in sodium battery in forming of $Na_{15}Sn_4$. Besides Sn has high electrical conductivity which can improve the conductivity of the compound thus hinder the capacity fading. Weijie[83], Youngjin Kim[84], and Xiulin Fan[85] have studied the SnP_x compound and composite. Weijie prerpared the $Sn_{4+x}P_3$ @ Amorphous Sn-P Composites by low energy ball milling. The composite has a Sn-P amorphous layer cover the $Sn_{4+x}P_3$ particles which maintain the stability of cycling performance. Youngjin Kim and Xiulin Fan also use ball milling method to prepare Sn_4P_3 and SnP_3 /C composite. Sn_4P_3 compound prepared by Youngjin Kim delivered a high reversible capacity of 718mAh g^{-1} and cycled for 100 cycles with little capacity decay. SnP_3 /C composite synthesis by Xiulin Fan performs well in sodium-ion battery

with high initial capacity 1131mAh g^{-1} and remain over 92% retention over 100cycles. Based on their study, the final sodiation mechanism of SnP_x can be concluded as follows:

$$SnP_x + (3x+4)Na^+ + 3x+4\ e^- \leftrightarrow Na_4Sn_{15} + xNa_3P$$

CoP has also been studied in sodium-ion battery. Our group[86] prepared the CoP by using simple ball milling method. The inactive Co plays as a conductive matrix toe hinder the volume change. The electrode can deliver a high capacity of 700mAh g^{-1}. The sodiation mechanism of CoP is similar to the lithiation process of CoP. During the discharging process, the CoP decomposed, and then the sodium-ion reacted with P. The equation after the initial discharge process is below:

$$CoP_3 + 9Na^+ + 9e^- \leftrightarrow 3Na_3P + Co$$

In a word, phosphorus-based compound and composites have high capacity of over 2500mAh g^{-1}in lithium and sodium battery, besides the redox potential of sodium ion inserted into phosphorus is about 0.4V *vs.* Na/Na^{+}. The lithiation and sodiation mechanism can be classed into two categories: conversion reaction and insertion reaction. The main challenge of application is the huge volume change during cycling and the poor electrical conductivity. In order to solve the problem, there are basically two methods: combined with carbon materials and use active or inactive metal to form phosphides. The results demonstrate that phosphorus-based compound and composites are promising anode materials.

2.3 Electrolytes

Electrolyte is a crucial part in both the lithium ion battery and sodium ion battery. The suitable electrolyte should exhibit: large electrochemical and thermal stability window; high ion conductivity and low toxicity; no reaction with the anode and cathode materials.

Table 2.1 The common salts of sodium ion battery

Salt	Anion chemical structure	M_w [g mol^{-1}]	T_m [°C] (Li-salt)	σ [mS cm^{-1}][a] (Li-salt)
$NaClO_4$		122.4	468 (236)	6.4 (5.6)
$NaBF_4$		109.8	384 (293)	(3.4)
$NaPF_6$		167.9	300 (200)	7.98 (5.8)
NaTf		172.1	248 (>300)	(1.7)
NaTFSI	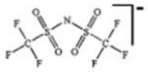	303.1	257 (234)	6.2 (5.1)
NaFSI	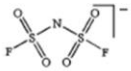	203.3	118 (130)	

[a] 1 M NaX (LiX) in PC at 25 °C.

For lithium ion battery, the most common and safe salt is $LiPF_6$ since other salts such as $LiClO_4$, $LiAsF_6$ and $LiBF_4$ are explosive or problematic on the negative side, or poisonous. The ion conductivity of $LiSO_3CF_3$ containing solution is low [87]. For sodium ion battery, the most common salts are shown in table.1. The suitable sodium ion salts also deliver high ion conductivity, low toxicity and electrochemical safety and stability. Another important part of the suitable electrolyte is the solvents. For lithium ion battery and sodium ion battery the common solutions are similar, for example the common

solutions are mostly organic carbonates such as dimethyl carbonates(EC), diethyl carbonates(DEC), and ethyl-methyl carbonates(EMC) and so on. Table 2 shows the melting, boiling, flash point, dielectric, and the viscosity of the solutions.

Additives are another important component of the suitable electrolyte. For the lithium ion battery electrolyte, the additives are supposed to improve the forming of SEI, protect the cathode or hinder the decomposition of the salt, or hinder the corrosion. There are numbers of additives available for applying in lithium ion battery electrolyte, such as VC, LiBOB, LiODFB, cyclohexane and so on [88].

The functions of additives in sodium ion electrolyte is similar to the additives in lithium ion battery.Some of the additives in lithium ion battery were also studied for sodium ion battery, including vinylene, ethylene sulphite, fluorethylene carbonates. These additives can efficiently helpful to form stable SEI.

CHPATER 3 EXPERIMENT METHODS

3.1Chemical and materials

The chemicals used in my study are summarized in Table 3.1

Table 3.1 Chemicals used in the study

Chemicals	Formula	Purity	Supplier
Polyvinyldene difluoride	$(CH_2CF_2)_n$ 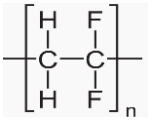	N/A	Sigma Aldrich
Carboxymethyl cellulose	$C_8H_{16}NaO_8$ 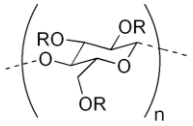	N/A	Sigma Aldrich
Sodium alginate	$C_6H_8O_6)_n$ 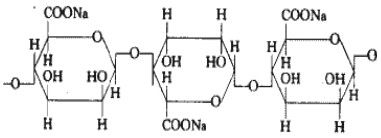	N/A	Sigma Aldrich
Polyacrylic acid	$(C_3H_4O_2)_n$ 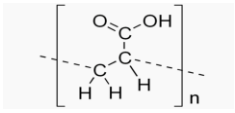	N/A	Sigma Aldrich
Copper foil	Cu	N/A	Sigma Aldrich

Graphite	C	N/A	Sigma Aldrich
Super P	C	N/A	Sigma Aldrich
Hyperchloric acid sodium salt	$NaClO_4$	≥98.0 % (T)	Sigma Aldrich
Sodium hexafluorophosphate	$NaPF_6$	98%	Sigma Aldrich
Lithium phosphorus fluoride	$LiPF_6$	98%	Sigma Aldrich
Lithium bis (fluorosulfonyl) imide LiFSI	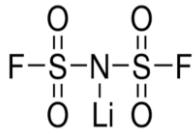	99%	Sigma Aldrich
Fluoroethylene carbonate	$C_3H_3FO_3$ 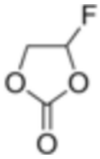	99%	Sigma Aldrich
Sodium metal	Na	99.9%	Sigma Aldrich
Lithium metal	Li	99.9%	Sigma Aldrich
Iron powder	Fe	99%	Sigma Aldrich

Tin powder	Sn	99%	Sigma Aldrich
Silicon powder	Si	99%	Sigma Aldrich
Phosphorus powder	P	99%	Sigma Aldrich
Dimethyl carbonate	$(CH_3O)_2CO$ 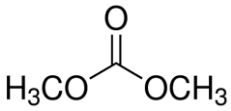	99%	Sigma Aldrich
Ethylene carbonate	$(CH_2O)_2CO$ 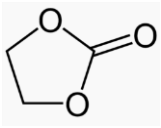	99%	Sigma Aldrich

3.2 Materials preparation

3.2.1 Ball milling

The ball milling machine

A ball mill works on the principle of impact and attrition: size reduction is done by impact as the balls drop from near the top of the shell. It was first started in the early 1870 for producing pottery.

The structure of the ball mills consisting of shell and balls. The balls are the grinding media which made of stainless steel and the inner surface of the shell is made of steel which is abrasion-resistant. When the ball mill works, the balls are lifted up on the

rising side of the shell and then quickly drop down, so that the solid particles are reduced by the impact. The mechanism of ball milling mechanism is shown in Fig3.1.

The ball milling methods usually have two applications: one is grinding the particles or solids to micro or nano size; another application is solid-state chemical reaction such as alloying.

The alloying mechanism usually includes several stages:

Firstly, the initial particles or solids are flattened by compressive forces. Later on, fracturing and welding are dominant, the solid-state chemical reaction happened. After that, the particles are more homogenous in micro-scale or nano-scale. Finally, the particles are deformed (might happen).

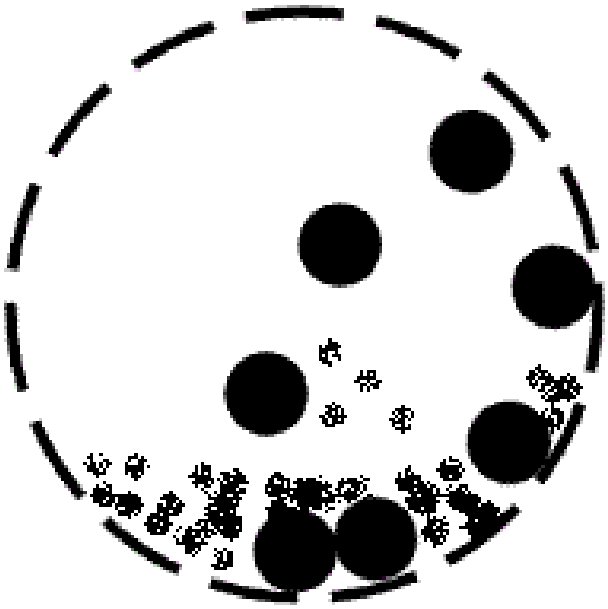

Fig 3.1 Ball mill mechanism.

Usually, an internal cascading can effectively reduce the material to a fine powder. Industrial ball mills can be fed at one end and discharged at the other end which has

various sized ball mills are mechanically rotated on their axis, but the one used in the study only consist of two cylindrical capped containers. The planetary ball milling machine used in this study is shown in Fig3.2.

Planetary ball milling process have been studied for long time. Joise firstly reported his work about the “satellite milling machine”. The determination of the parameters and the optimized mechanism are discussed in his work. In order to find the best synthesis mechanism, various parameters are needed to be determined, such as time of milling, ball milling rate, the ratio of ball milling media to powders and so on.

Fig 3.2 Ball milling machine.

3.2.2 Polymerization

Polymerization is a chemical reaction of reacting monomer molecules into three-dimension polymer networks. Polymerization occurs via various chemical reactions due to the various functional groups such as carbonyl group or alkenes. Some of the monomer units can polymerize themselves such as formaldehyde hydrates, others can form useful long polymer. The example of polymerization is shown in Fig3.3.

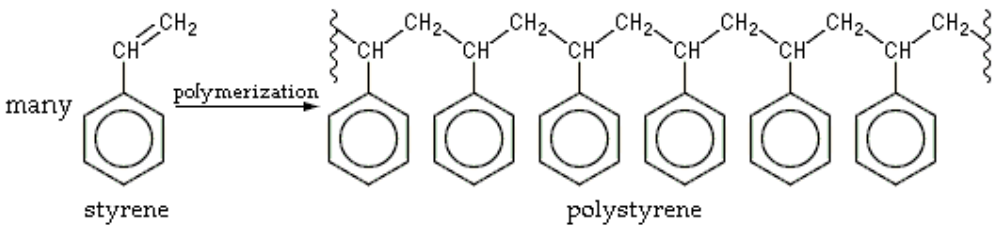

Fig 3. 3 Example of polymerization

The polymerization process usually includes step-growth and chain-growth. Step growth is the reaction between functional groups such as carbonyl group or alkenes; the chain-growth involves the process of molecules' linking together to form long-chain polymer. The example of polymerization is the polymerization of ethylene as shown in Fig3.4. The new propagating center formed form the broken of the π bond.

Fig 3.4 The mechanism picture of polymerization of ethylene

3.3 Physical and chemical characterization

3.3.1 X-ray diffraction

X-ray diffraction is an efficient technique used to analyze crystal structure. The wave length of the X-ray is 0.01 to 10 nm. Thus, the X-ray can be scattered by each set of lattice planes at a unique angle. Based on these, the crystal structure can be analyzed.

The theoretical principle of the X-ray diffraction is Bragg's law:

$$n\lambda = 2d\sin\theta$$

Where d is the lattice spacing of the crystal, n is an integer, λ is the wavelength of the incident X-ray beam, and θ is the angle of the incidence, as shown in Fig3.5.

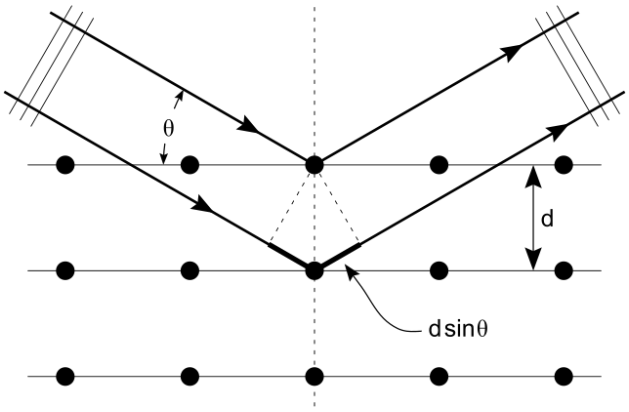

Fig 3.5 The schematic picture of Bragg's law.

In my study, all the XRD measurements were conducted on GBC MMA X-ray generator and diffractometer with Cu Kα radiation with λ of 1.5406 Å. The X-ray diffraction analyse method is the mostly widely used crystal structure analyse measurement.

3.3.2 Scanning electron microscopy equipped with energy dispersive spectroscopy

SEM is a widely used electron microscope with a high-energy electron beam to analyze the surface structure of materials. A variety of signals of the morphology of surface can be detected from the interact with atoms. The electron beam which has an energy range from 0.5ev to 40keV is produced and pass through the scanning coils, and reflect the morphology of the surface of the material. The machine used in the master study is JSM-7500A.

3.3.3 Transmission electron microscopy

TEM is a technique used to analyze the morphology and structure of the materials. The gun of the transmission electron microscopy will emit electrons under high voltage over 100kv. When the material is exposed to this high energy electron beam, the diffractions will occur, and different structures will have different angles, thus the morphology and structures will be analyzed. During my master study, the TEM experiment is carried on JEO 2011.

3.3.4 X-ray photoelectron spectroscopy

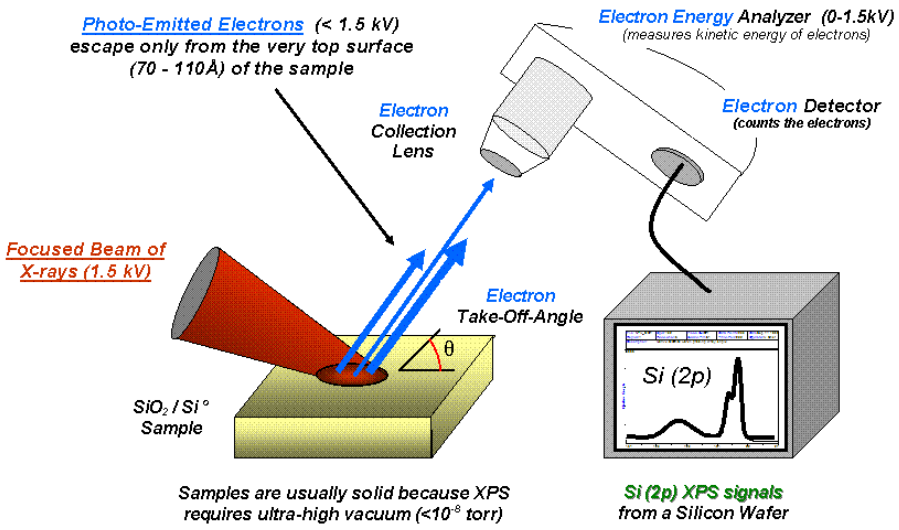

Fig 3. 6 The simple schematic picture of XPS.

XPS is a technique used to analyze the elemental composition at the parts per thousand range which can be used to analyze the surface chemistry of the materials. The simple

schematic picture is shown in Fig3.6. The X-ray photoelectron spectroscopy can be performed by using a XPS system. The basic theoretical equation is shown below:

$$\mathrm{E_{binding}} = E_{\mathrm{photon}} - (\mathrm{E_{kinetic}} + \emptyset)$$

3.3.5 Raman spectroscopy

Raman spectroscopy is a spectroscopic technique widely used in chemistry and material science which is used to identify molecules. Raman measurements can be considered as a procedure that light interacts with molecules and produce the different wavelength radiations. The elastic and inelastic scattering reflects chemical and structure information by showing the energy shift from the radiation. Thus, the molecules can be identified. In my master work, the JOBIN YVON HR800 Raman system with laser wavelength of 632.8nm was used to analyse the materials.

3.4 Electrochemical Measurements

The electrochemical measurements are used to analyze the electrochemical performances of the anode material of lithium and sodium ion batteries.

3.4.1 Electrode preparation and battery assembling

Fig.3.7 The picture of planetary mixture machine

Mixtures of the materials are prepared by the planetary mixture machine as shown in Fig3.7. The materials, binders such as CMC and PVDF, and super P are mixed together by the machine to form a homogenous slurry.

Fig 3.8 The picture of electrode preparing machine.

Then then slurry was coated on the Cu foil by the electrode preparing machine as shown in Fig3.8. After that, the electrode will be dried in the vacuum Oven at the temperature of 80°C or 120°C. After that the electrode will be punched into round with a diameter of 0.96mm.

3.4.2 Galvanostatic electrochemical testing

Galvanostatic electrochemical testing measurements are carried on at a constant current density. The columbic efficiency, capacity and electrochemical plat can be calculated or got from the charge-discharge performance. In my master study, the galvanostatic electrochemical testing was carried on Land battery tester system.

CHAPTER 4 ULTRAFINE NANOSTRUCTURE SILICON-BASED COMPOSITE FOR USE IN HIGH-PERFORMANCE LITHIUM SECONDARY BATTERIES

Introduction

The growing energy demands for practical application in electrical vehicles, portable electronics with high energy density, environmental friendly and low costs lithium ion battery is becoming more and more intense [89-90]. Silicon is abundant in earth curst and is environmental friendly, besides based on the Faraday's law, the anode material which has low formula weight and high electric charge has the highest theoretical capacity [91] and Silicon has the highest theoretical capacity of 4140mAh g^{-1} （$Li_{4.4}Si$）which make it the most promising anode material of lithium ion battery.

The electrical isolation, huge volume changes during charge and discharge and the continuous formation of unstable SEI drastically cause the deterioration of the electrical performance of silicon. Because of this, various studies are focused on hindering the volume change of silicon anode. Typically, using active and inactive materials to hinder the volume change can efficiently improve the cycling performance.

Inactive materials such as Ni [39, 92],Cu[43], Co [44], Fe [45], active metals such as Mg [47],Al [93],Zn [49],Sn [50-52], and can be alloyed with silicon. Using these metals can improve the electrical conductivity and hinder the volume change, so that they can improve electrochemical performance comparing to pure silicon. Beside, active metal can hinder the forming of two-phase regions which can hinder the pulverization. In addition, when

silicon and other metallic element are combined at a proper ratio, they will form isotropic amorphous phase which is beneficial to stable cycling performance and rate capacity. Furthermore, since metal materials have high density comparing to carbon, the alloy compound volume capacity will be higher.

In this chapter, the active material Sn and inactive material Fe together with carbon material graphite were used to prepare the silicon based nanocomposite applied in lithium ion battery.

Experiment

The Si/Fe/Sn/Carbon composite was prepared by simple high energy ball milling method. The starting material Silicon, Tin, iron and graphite powder were mixed at the ratio of 1:1:1:2 and put in a hardened steel vial with 2mm diameter steel balls. The steel vials were sealed in the argon atmosphere in glove box. The rotation speed is 500rpm and the milling time is 40 hours.

The crystalline structure of the active powder was characterized by powder X-ray diffraction (XRD) on a GBC MMA diffractometer with a Cu Ka source. Raman spectra were collected using a HR800 JOBIN Yvon Horiba Raman spectrometer. The morphology of the sample was investigated by field emission scanning electron microscopy (FESEM; EOLJSM-7500FA) and transmission electron microscopy (TEM, JEOL 2011, 200 keV). X-ray photoelectron (XPS) was conducted using a SPECS

PHOIBOS 100 Analyzer installed in a high-vacuum chamber with the base pressure below 10^{-8} mbar. The anode was prepared by coating the slurry of as-prepared Si/Fe/Sn/Carbon composite (80%wt) sodium carboxymethyl cellulose (CMC,10%wt) and acetylene black (10%wt) on a copper foil. The electrode was then dried at 80% in vacuum for 10 hours. The electrolytes for test are 1M $LiPF_6$ or LIFSL in ethylene carbonate/diethyl carbonate (1:1 vol/vol).

Results and discussion

Fig4.1 shows the The XRD pattern of the Si/C/Fe/Sn composite after low-energy ball milling method. The diffraction sharp peaks at 28.6° 47.4° and 56.2°are assigned to （111） (220）and（311）planes which are indexed to cubic phase silicon crystal with Fd3m (JPCDS NO.65-1060). There is no obviously peaks of alloy compound were observed which indicates that after ball milling no new phase was formed during the milling process. Moreover, no diffraction lines from crystalline Tin, Iron and carbon were observed in the XRD patterns, thereby indicating the elements are changed into amorphous.

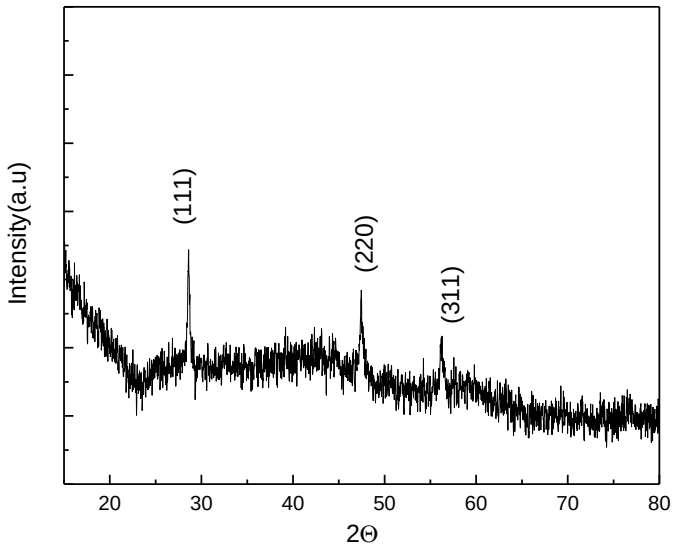

Fig 4.1 XRD pattern of Si/Fe/Sn/C composite

The results is consistent with the TEM selected area electron diffraction image are indexed to cubic phase of silicon, and the diffraction rings are corresponded to (111)(220) (311) and (422) planes.

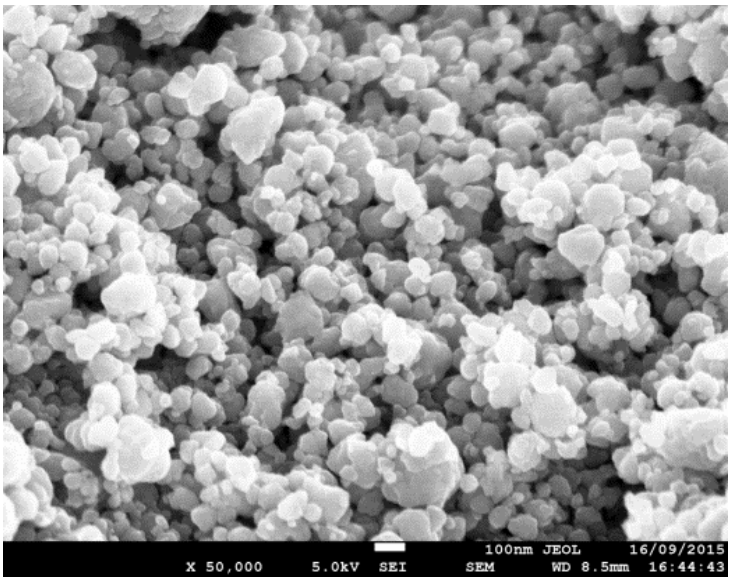

Fig 4.3 The SEM picture of Si/Fe/Sn/C composite

The morphology of the as-prepared nanocomposite was analysed by field emission scan electron scope and EDS mapping.

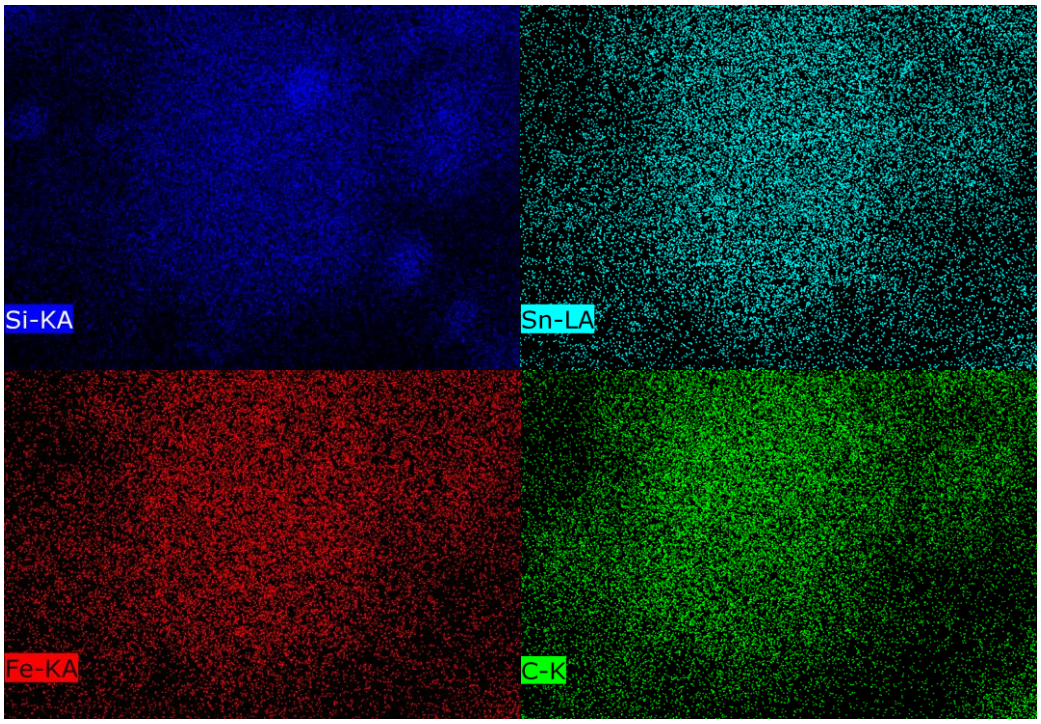

Fig 4.4 EDS mapping picture of Si/Fe/Sn/C nanocomposite

As shown in Fig4.3, after ball milling procedure, the nanoscale particles around 100nm are obtained which is beneficial to standing tensile stress during charging and discharging,and some agglomerates are also found. The EDS mapping picture in Fig 4.4 indicate that Silicon Tin Iron and carbon have been homogeneously mixed.

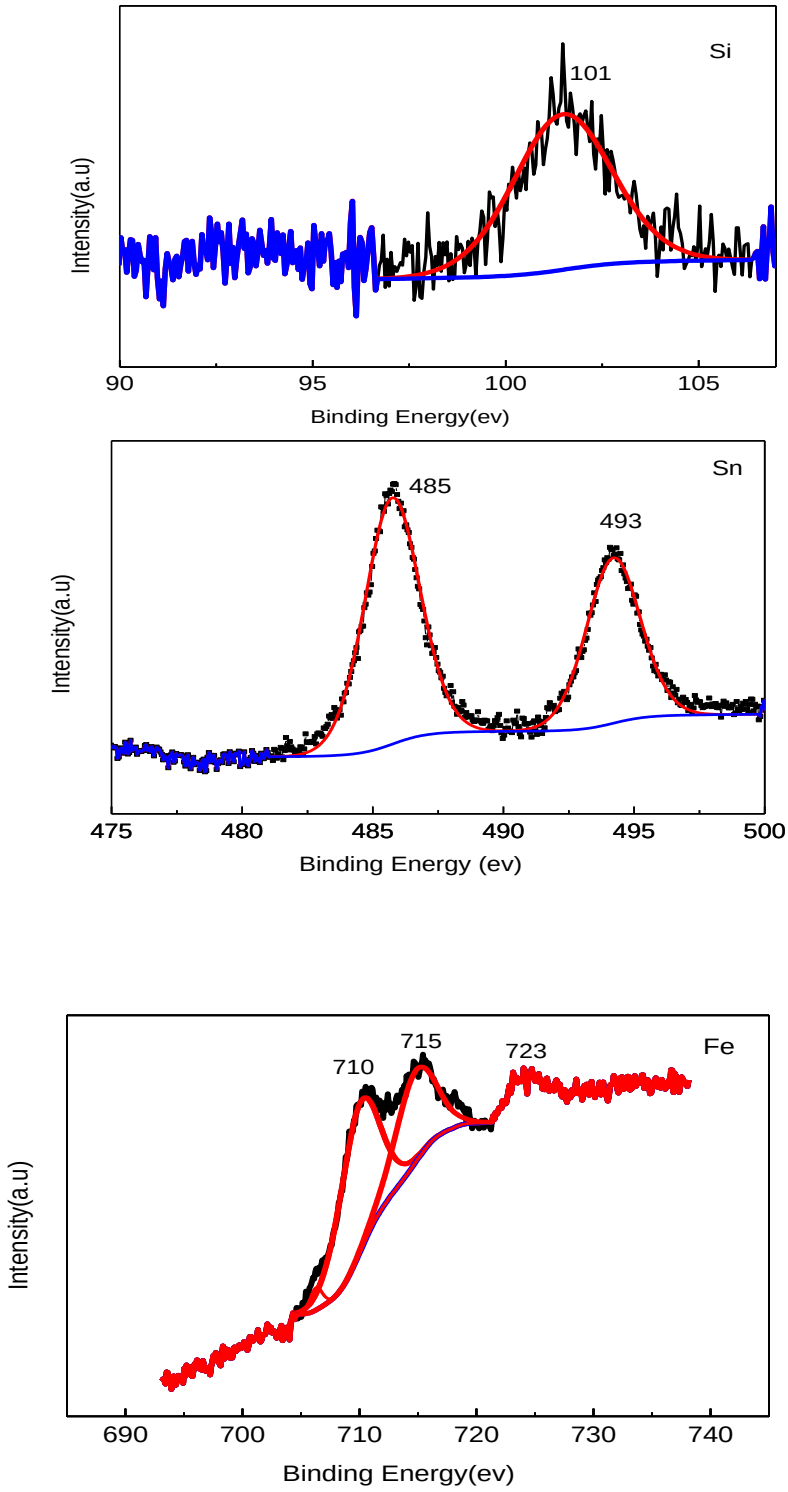

Fig 4.5 XPS survey scan of S2p, Sn3d and Fe2p photoelectron of Si/Fe/Sn/C composite

In order to further analyse the chemical state on the surface of the nanocomposite after ball milling, XPS was conducted. As shown in Fig4.5, to identify all the states of Silicon,

Iron, Tin and carbon elements, we conducted the Si2p, Sn3d and Fe2p. Fig4.4(a) presents the XPS spectra of Si2p, the binding energy of Si2p was at 101ev which approximately correspond to the bulk silicon. Similarly, as shown in Fig 4(b) the main peaks of Sn3d located at located at 485ev and 493ev respectively are ascribed to Sn. Fig4.4(c) presents Fe2p high-resolution XPS spectra. XPS Fe2P core-level exhibited Fe $2P_{1/2}$ line at a binding energy of 723ev and the $Fe2p_{3/2}$ line at binding energy of 710ev which indicate the exist of Fe_2O_3. The peak located at 715 is similar to the characteristic satellite peak of Fe_2O_3. Based on results we confirm that Fe in the nanocomposite has been oxidized to the trivalent state . Zero-valent Fe which is more reducible comparing to Tin and Silicon act as protector to be oxidized firstly which avoids the Sn and Si being oxidized through ball-milling procedure.

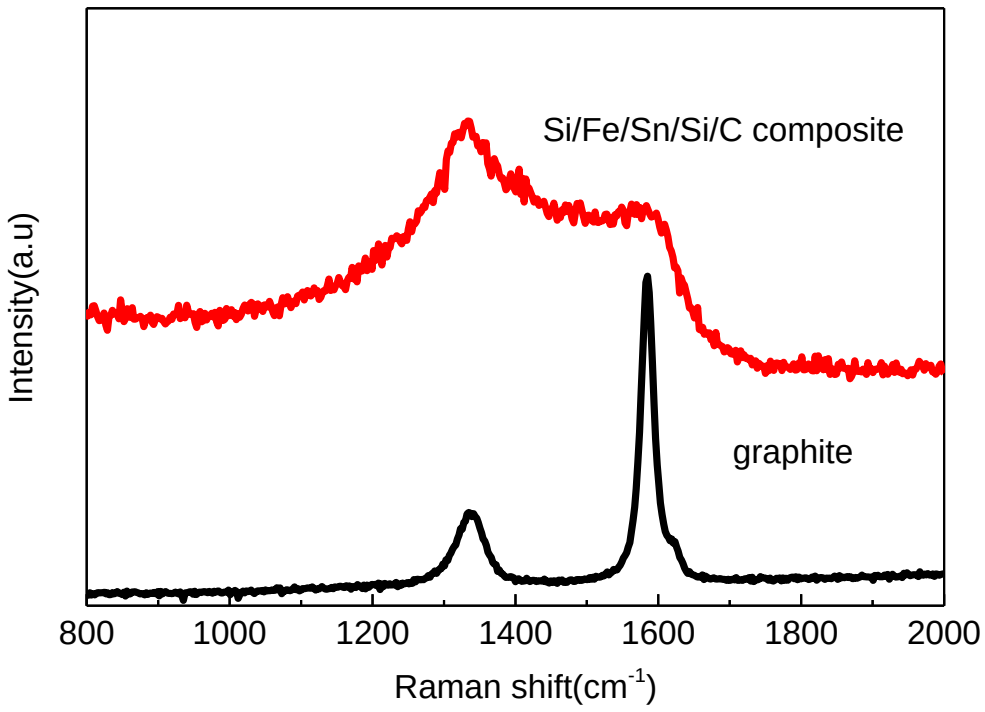

Fig 4.6 Raman spectra of Si/Fe/Sn/C composite and graphite.

After ball milling the precursor graphite has changed into amorphous carbon as shown in Raman spectra, as shown in Fig 4.6. The two board bands are at 1330 cm^{-1} and 1580 cm^{-1} corresponding to the D and G bands of carbon, respectively. The I_D/I_G ratio is 1.22 indicates the low graphitic degree in the composite, since there is no peak, it reflects that amorphous carbon is covered over the composite.

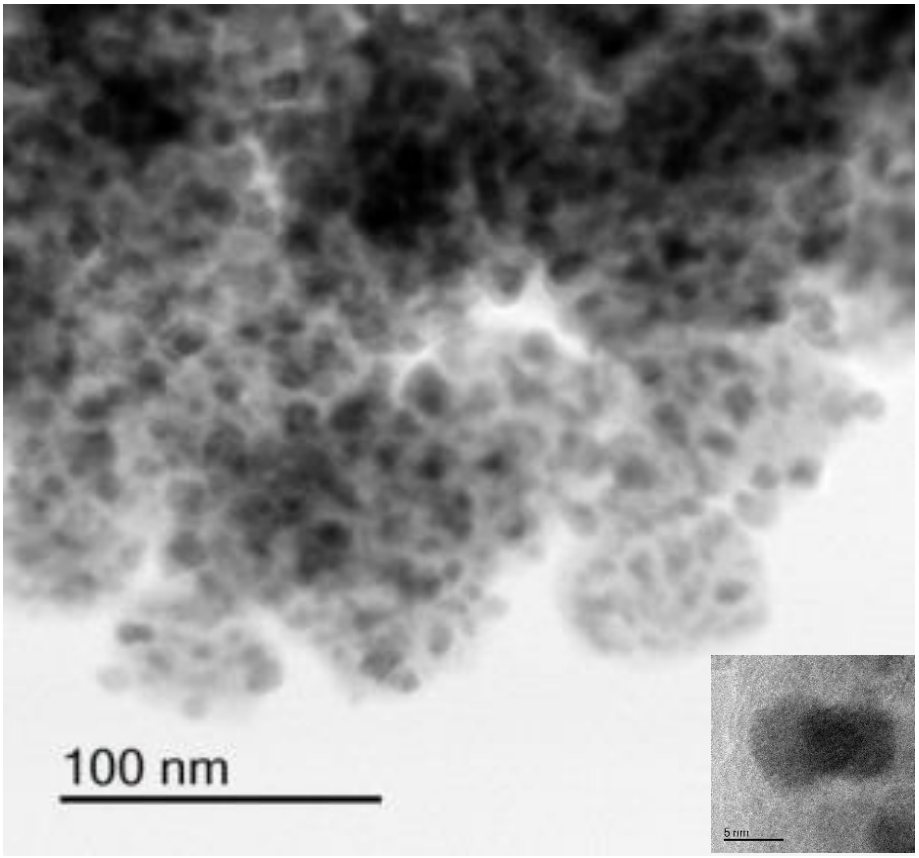

Fig 4.7 TEM picture of Si/Fe/Sn/C nanocomposite

The resolution transmission electron microscope image is shown in Fig 4.7, the silicon crystals embedded in the amorphous matrix with crystals around 5-10nm as shown in the attached map.

The frogspawn like structure can deliver outstanding electrochemical performance, since the amorphous matrix can efficiently hinder the volume change; the “spawn” with electrical shell continuously connect each other which are beneficial to improve the electrical conductivity of silicon; the continuously carbon network can hinder the agglomeration of silicon and Tin upon prolonged cycling.

Besides, as can be seen from the TEM mapping pictures as shown in Fig 4.8, by the simple ball milling method the elements have been homogeneously mixed even at nanoscale.

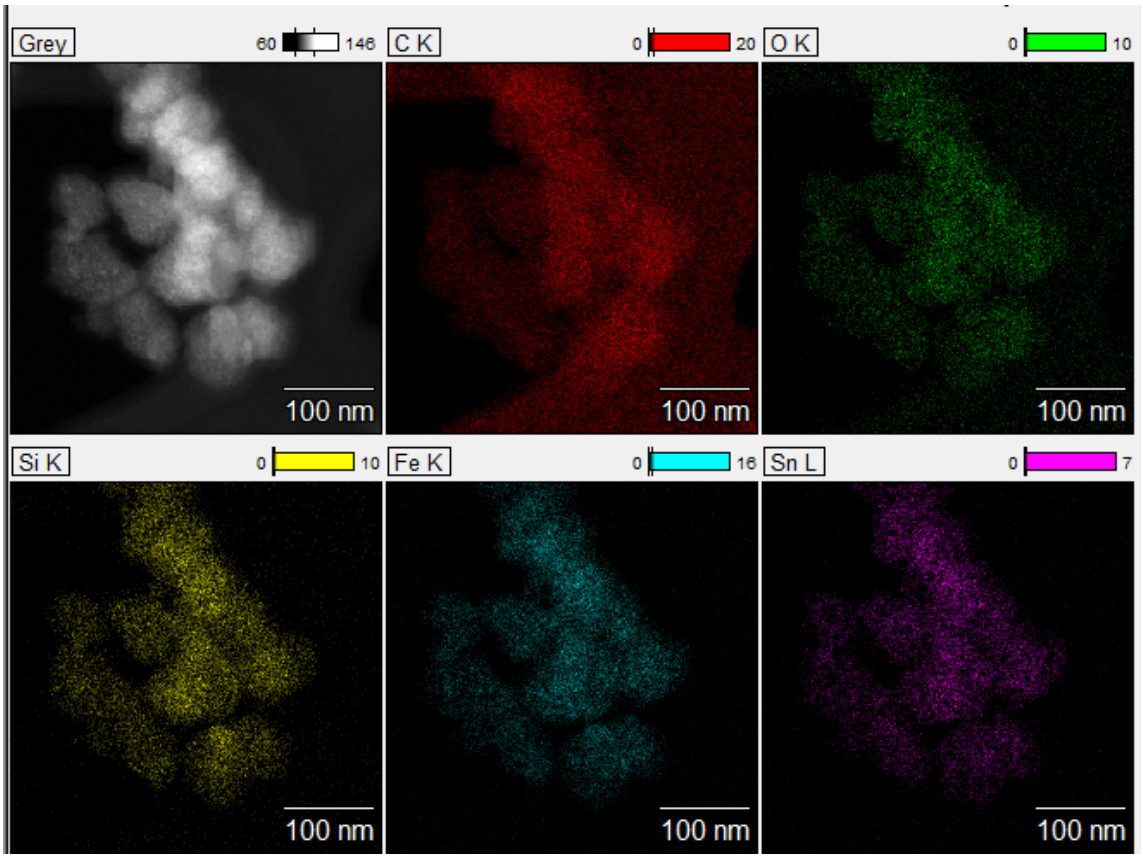

Fig 4.8 TEM mapping picture of as prepared Si/Fe/Sn/C composite.

As an investigation into the as-prepared nanoscale anode material, the electrochemical performance of Si/C/Fe/Sn composite was evaluated with a coin-type lithium half-cell within the voltage 0-3V. The electrolytes used were 1M $LiPF_6$ or 1M LiFSI dissolved in a solution of EC:DEC=1:1(v/v). Fig 4.4.(b) shows the cyclic voltammetry picture of Si/C/Fe/Sn composite.

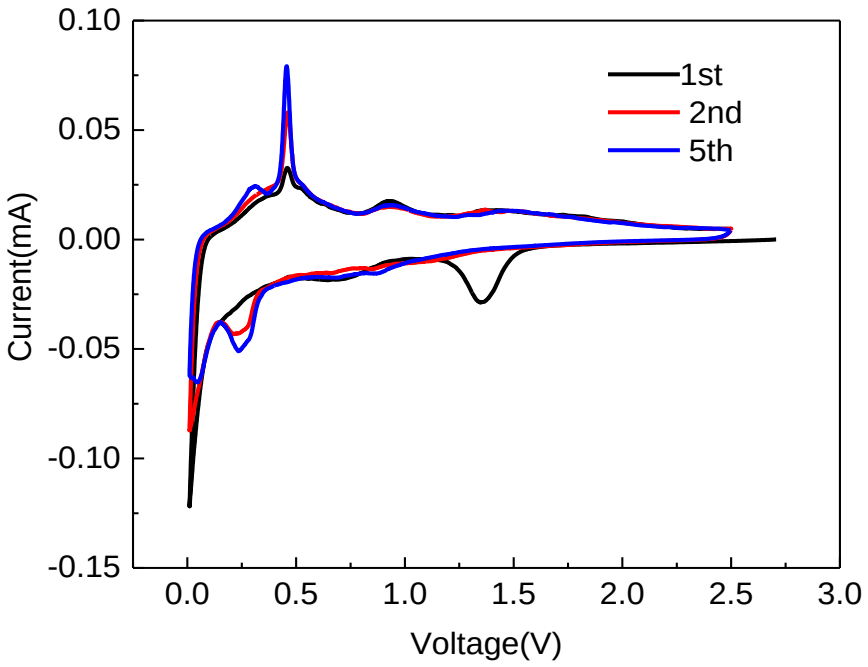

Fig 4.9 The CV curve of Si/Fe/Sn/C composite in a coin cell

The cathodic peak at 0V and the anodic peak at 0.45V are characteristic of crystalline Si. The anodic peaks at 0.21V and 0.09V are corresponded to the forming of SEI. The shift of peaks to lower potential indicates the lower ionic conductivity of the electrolyte because of the different ionic conductivity of the salts [3].

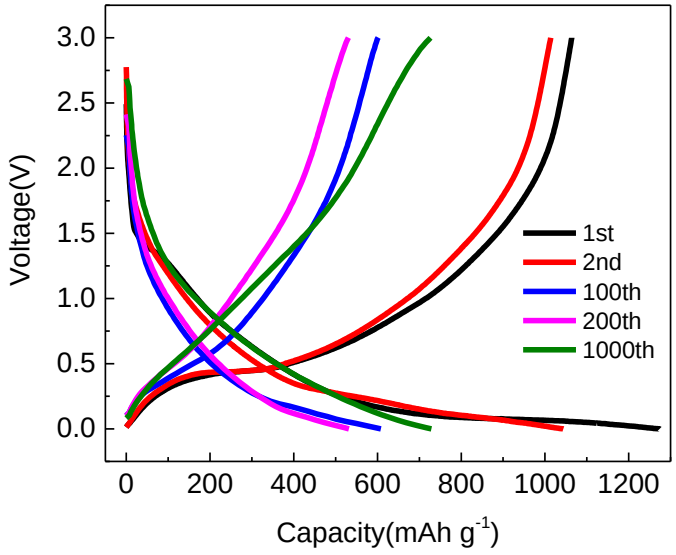

Fig 4.10 Charge-discharge curves of Si/Fe/Sn/C composite in a coin cell

As shown in Fig 4.10 The initial capacity of Si/Sn/Fe/C composite tested in LiFSL electrolyte is 1274mAh g^{-1}, even after 1000 cycles, the capacity remains high capacity of 620 mAh g^{-1}.

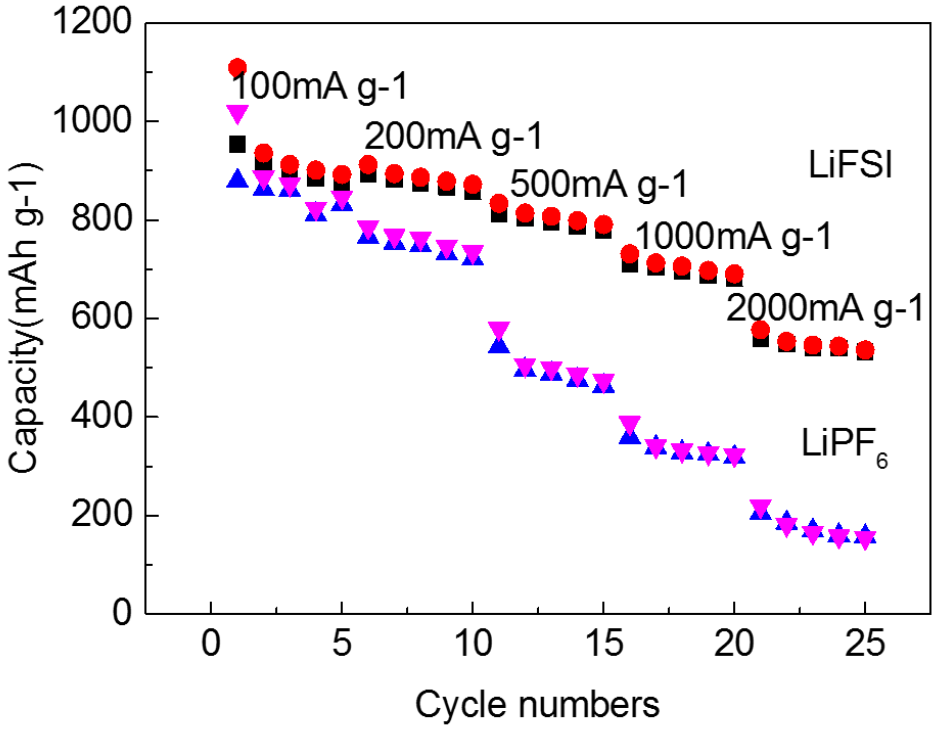

Fig 4.11 the rate performances of Si/Sn/Fe/C composite in different electrolytes

Fig 4.11 shows the excellent rate performance of Si/Sn/Fe/C composite at current density of 100 mA g^{-1} ,200 mA g^{-1} ,500 mA g^{-1},1000 mA g^{-1} ,2000 mA g^{-1}. When the current density increases to 2000 mA g^{-1}, it remains a high capacity of 570 mAh g^{-1}.

Si/Sn/Fe/C composite shows superior rate performance in electrolyte of 1M LiFSI dissolved in a solution of EC:DEC=1:1(v/v), this is due to the better ion conductivity of the electrolyte.

Fig 4.12 shows the cycling performance of Si/Sn/Fe/C composite in different electrolytes. The electrode delivered superior performance in 1M LiFSI dissolved in a solution of EC:DEC=1:1(v/v) since the electrolyte has higher ion conductivity. The

capacity decreased in the first 200 cycles, and after that it become stable. The capacity retention in the 1000th cycle is 700mAh g^{-1} which is 54.9% of the initial capacity.

In order to analyse the reason of capacity variation during the cycling, TEM mapping was carried on to analyse the morphology change of the electrode. As shown in Fig 4.13. Fig4. 14 and Fig 4.15, from the 50th to the 200th cycle the particle size decreases from around 5nm to 1nm because of the pulverisation. After that, the particle size become stable, due to electrochemical reaction can hardly result in further pulverisation.

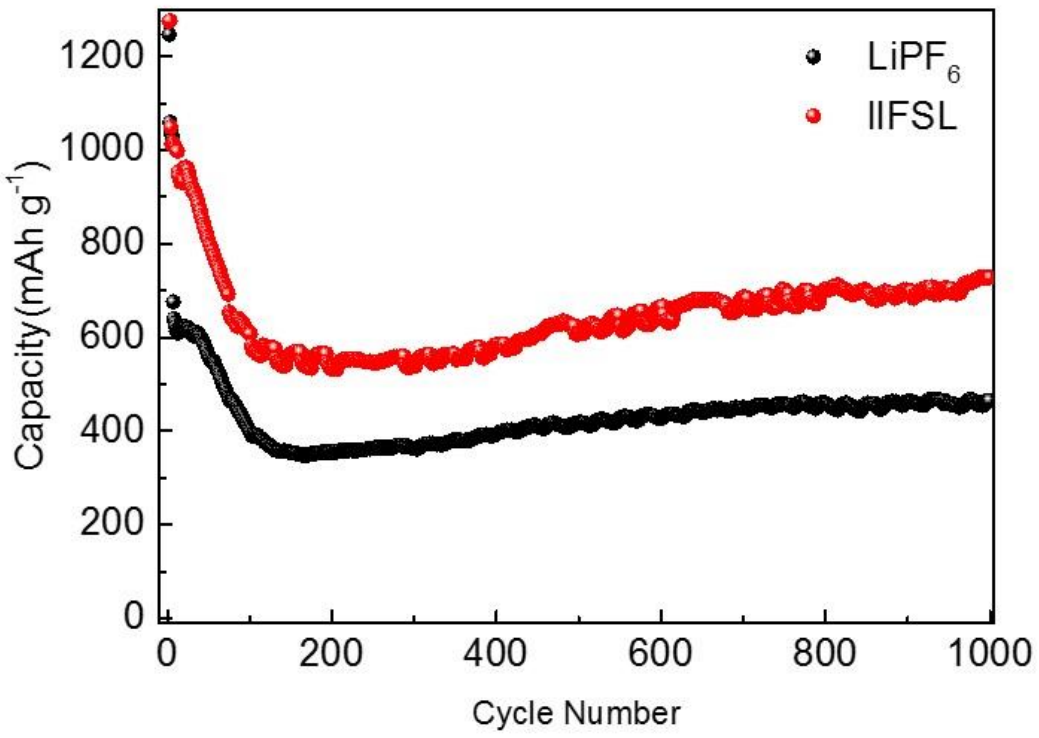

Fig 4.12 The cycling performance of Si/Sn/Fe/C composite in different electrolytes

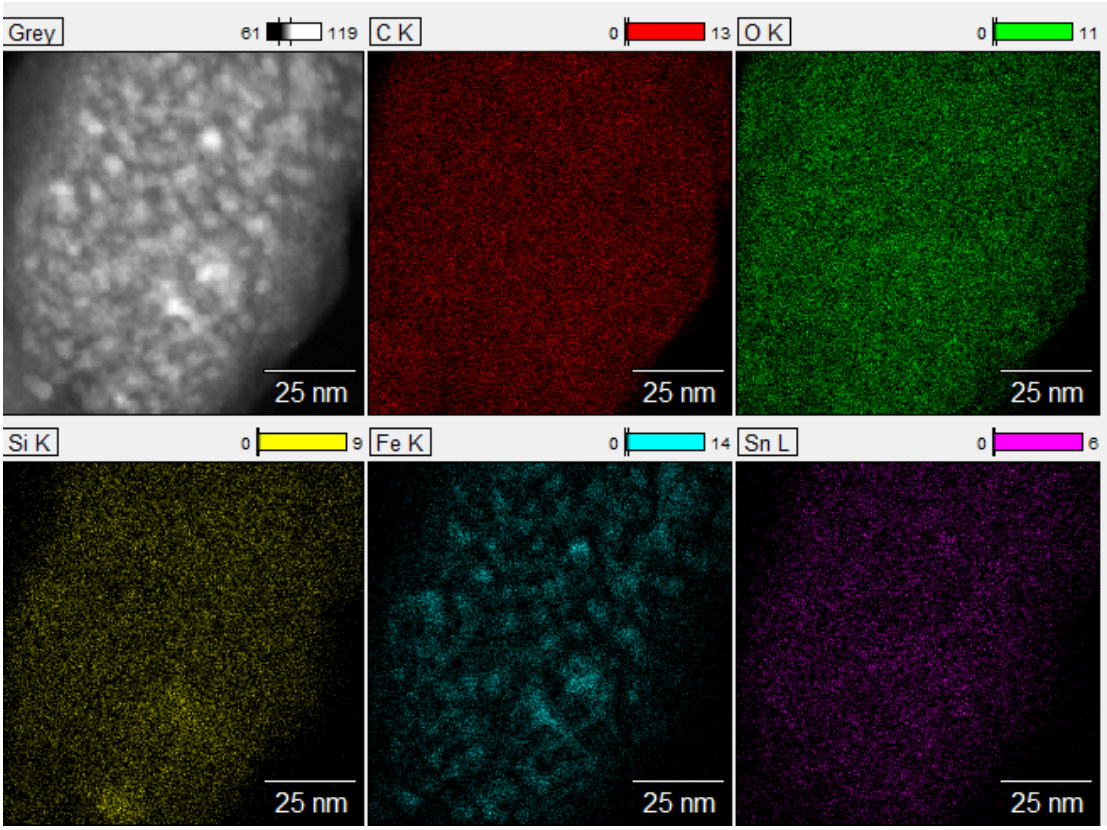

Fig4 .13 The TEM mapping picture of Si/Sn/Fe/C electrode after cycling for 50 cycles.

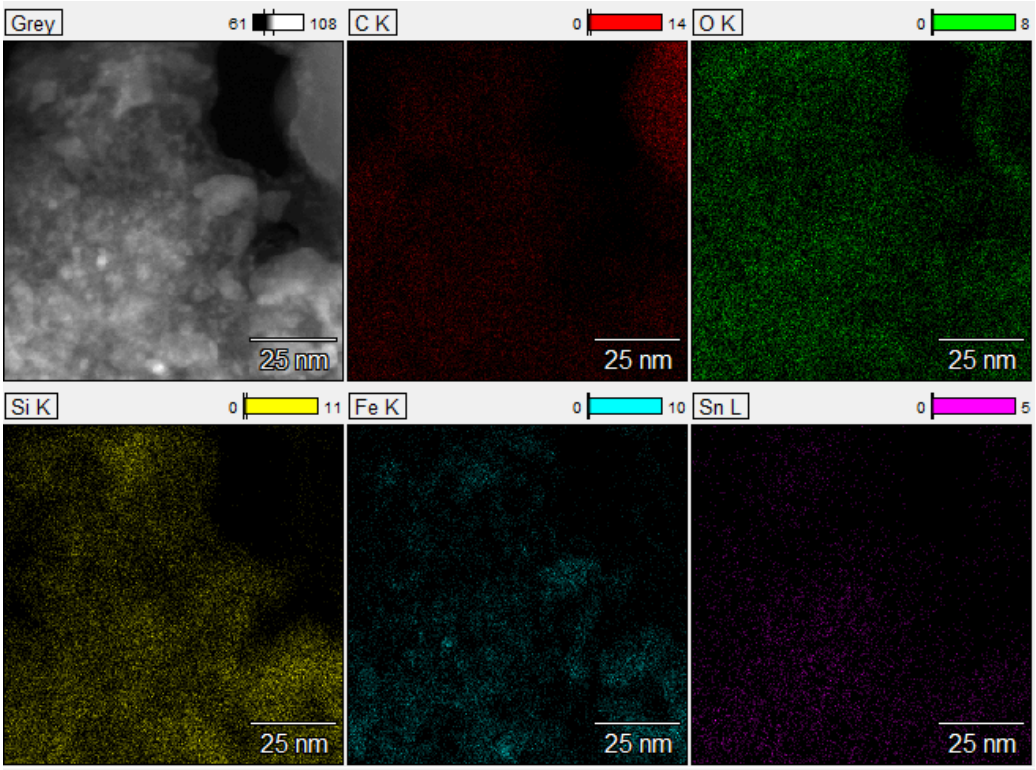

Fig 4.14 The TEM mapping picture of Si/Sn/Fe/C electrode after cycling for 200cycles

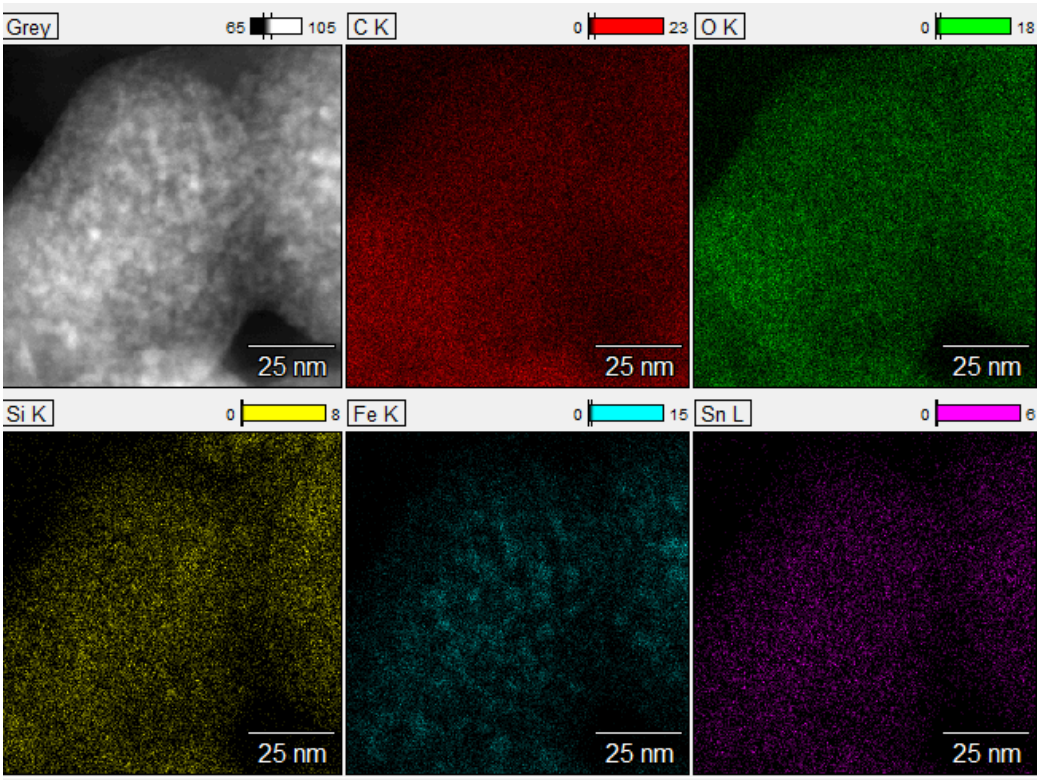

Fig 4 .15 The TEM mapping picture of Si/Sn/Fe/C electrode after cycling for 800 cycles

Conclusion

Si/Sn/Fe/C composite was successfully synthesis by the simple ball milling method. The electrode delivers excellent electrochemical performance, because the he active material Sn and inactive material Fe together with carbon material graphite efficiently improve the conductivity and hinder the volume change of the silicon.

CHAPTER 5 SN/SNO_2@C COMPOSITE NANOFIBERS AS ADVANCED ANODE FOR LITHIUM-ION BATTERIES

Introduction

Lithium-ion batteries (LIBs) are widely applied state-of-the-art power sources for consumer electronic devices and electric vehicles because of their high energy density, long charge/discharge cycle life, and lack of any "memory effect" [94-95]. Although commercial graphite performs well as an anode material for LIBs, it suffers from safety issues and its low theoretical lithium storage capacity (372 mAh g^{-1}) [94, 96]. Therefore, to satisfy the ever-growing power requirements, great efforts have been made to explore alternative materials to replace graphite anode [97-99]. Among these appealing candidates, tin-based materials (Sn and/or SnO_2 and their composites) have been considered as suitable substitutes for graphite, owing to their higher theoretical capacity than carbonaceous materials, safe working potential, and low toxicity [100-101]. Nevertheless, the practical usage of tin-based materials for LIBs is severely hampered by large specific volume changes that occurs during Li^+ insertion and extraction reactions, which usually cause the aggregation and pulverization of active material particles with fast capacity fading [102]. To overcome this problem, carbon materials were used to hybridize with tin-based materials, and these hybrids could not only effectively accommodate the strain of volume changes, but also enhance the conductivity of the electrode materials, thus improving the Li^+ storage and cycling performance [103]. Recent works have demonstrated that composite electrode materials consisting of a tin-based

material and a one-dimensional (1D) carbon material, such as carbon nanotubes (CNTs), can effectively improve the lithium ion storage capability, as well as maintaining excellent cycling performance, which makes these composites suitable for potential applications in LIBs [104-105], although the synthesis of such 1D hybrid composites generally involves special apparatus, tedious fabrication processes, and even expensive and non-eco-friendly solvents. For example, binding SnO_2 nanocrystals in graphene sheets were fabricated via a 28 h hydrothermal process and a tedious procedure for in situ hydrazine monohydrate vapor reduction [106]. In another report, carbon nanowires@ultrathin SnO_2 nanosheets@carbon composite was fabricated via a long process, including polymerization of pyrrole to form a polypryyole nanowires@ultrathin SnO_2 nanosheets composite and a solvothermal reaction, which was followed by an ice-water bath to rapid cooling [107].Therefore, it is highly desirable to develop a facile strategy to simplify the synthetic approach and reduce the preparation time and cost of 1D tin-carbon composites.

2.Experimental

2.1Synthesis of Sn/SnO_2@C

In a typical synthesis, 0.5 g commercial CNTs (NTP3003, > 95%) were uniformly dispersed in 30 ml dimethylformamide (DMF, Sigma-Aldrich, 99.8%) and deionized water solution (1:1 v/v) by 4 h ultrasonic treatment via an ultrasonic processor (SONICS Vibracell VC750). 1.52 g $SnCl_2$ (Sigma-Aldrich, 98%) and 0.3 g polyvinylpyrrolidone (PVP, Sigma-Aldrich, with average mol. wt. of 40,000) were

dissolved in 3 ml of the above solution with intensive stirring at ambient temperature. Then, the solution was stirred in an oil bath at 90 °C for 30 min to let the solvent evaporate. After cooling naturally, the residue was transferred to a corundum boat, which was located in the center of a horizontal tube furnace. The furnace was flushed with Ar for 10 h to remove oxygen and moisture in the reaction system, and the precursor was then heated in Ar atmosphere at a heating rate of 5 °C/min. When the temperature reached 600 °C, the Ar was switched to 5% H_2/Ar mixed gas. After 2 h of reaction, the system was cooled down naturally to room temperature in Ar. The black powder in the corundum boat was collected. This sample was designated as Sn/SnO_2@C.

Materials characterization

X-ray diffraction (XRD) patterns of the sample were acquired with a GBC MMA powder diffractometer equipped with a Cu Kα radiation source (λ = 1.541 Å) operating at 40 kV and 25 mA (step size = 0.002° s^{-1}). The morphologies were observed by field-emission scanning electron microscopy (SEM, JEOL JSM 7500-FA, 5 kV) and high-resolution transmission electron microscopy (HRTEM, JEOL ARM200F, 200kv). Thermogravimetric analysis (TG, METTLER TOLEDO TGA 1 STAR System) was conducted from 40°C to 950 °C at a ramp rate of 10 °C min^{-1} in air to determine the changes in sample weight with increasing temperature and to estimate the amount of carbon fraction in the sample. X-ray photoelectron spectroscopy (XPS) of the sample was conducted on a SPECS PHOIBOS 100 spectrometer installed in a high-vacuum

chamber with base pressure below 10^{-8} mbar. X-ray excitation was provided by monochromatic Al Kα radiation with photon energy *hv* = 1486.6 eV at the high voltage of 12 kV and power of 120 W. Raman spectroscopy (JobinYvon HR800) was also conducted by employing a 10 mW helium/neon laser at 632.8 nm.

2.3 Electrochemical measurements

The electrodes were prepared by mixing 80 wt% active material (Sn/SnO_2@C), 10 wt% carbon black, and 10 wt% polyvinylidene fluoride (PVDF) binder to form an electrode slurry, which then was coated onto copper foil, followed by drying at 120 °C in a vacuum oven for 12 h. The electrode was punched into round discs, with the electrode material loaded at ~2 mg cm^{-2}. The electrodes were then pressed at 10 MPa by using a pair of disc-shaped steel dies 14 mm in diameter to enhance the contact between the Cu foil, active material, and conductive carbon. CR2032 coin-type cells were assembled in an Ar-filled glove box (Mbraun, Unilab, Germany). Lithium metal foil was employed as both reference and counter electrode. The electrolyte was 1.0 M $LiPF_6$ in an ethylene carbonate (EC) – diethyl carbonate (DEC) solution (1:1 v/v). The cells were galvanostatically charged and discharged in the range of 0.005-3 V at different current densities by a Land CT2001A battery tester at 25 °C. The calculation of specific capacity is based on the mass of active material (excluding carbon black and binder). A Biologic VMP-3 electrochemical workstation was used to perform electrochemical impedance spectroscopy (EIS, ac amplitude 10 mV, frequency range

100 kHz – 0.01 Hz) and cyclic voltammetry (CV, voltage range 0 – 3.2 V, scan rate 0.1 mV s^{-1}).

Result and discussion

Fig5. 1 shows the XRD pattern of the Sn/SnO_2@C. As observed, besides the broad peak located at around 26°, which is due to (002) diffraction of graphite in the CNT [108], the crystalline Sn (JCPDS card No. 04-0673) diffractions can be clearly observed [109-110], It is suggested that the Sn came from the decomposition of $SnCl_2$ during the synthetic process, when heating at 600 °C in the reducing 5% H_2/Ar atmosphere. The sharp peaks of Sn also indicate that the Sn in the composite is well crystallized. Moreover, no obvious diffraction peak assigned to tin oxide is observed, suggesting that the tin oxide could be in a poorly crystallized state. The content of carbonaceous species in the Sn/SnO_2@C composite, including CNTs and the amorphous carbon matrix, is estimated to be 63.1 wt% by TG analysis in Fig5.2.

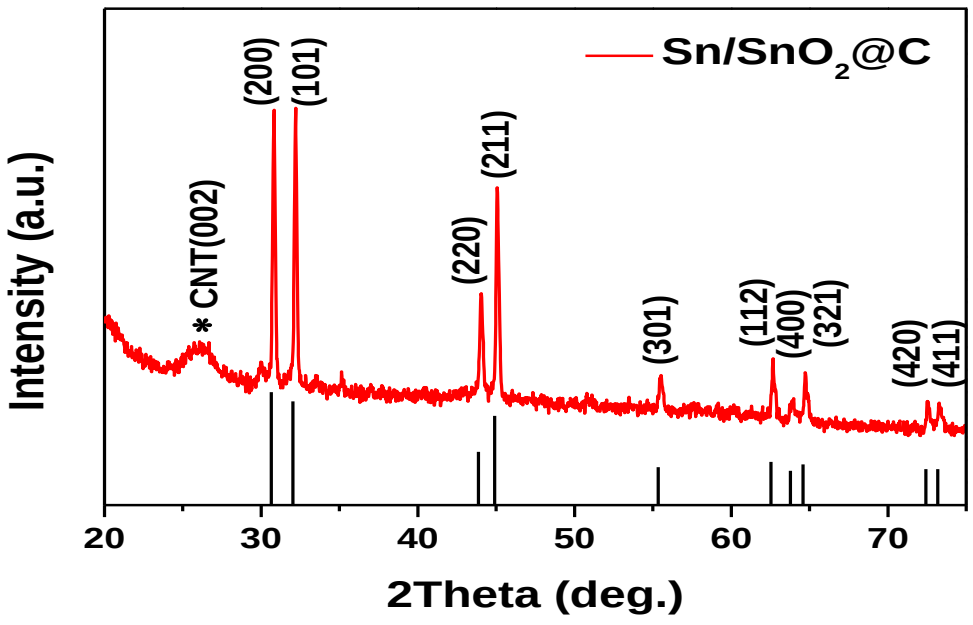

Fig 5.1 XRD pattern of Sn/SnO_2@C

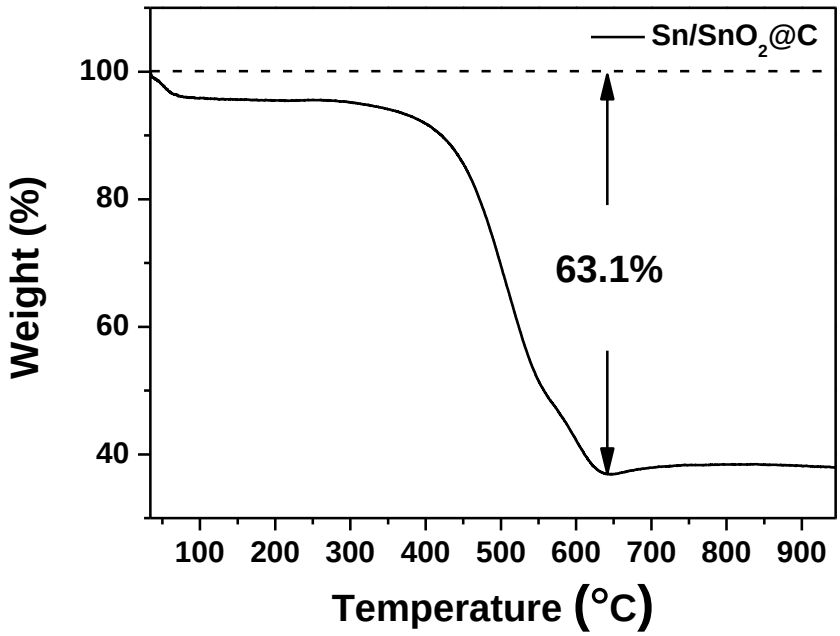

Fig 5.2 TG curve of Sn/SnO2@C

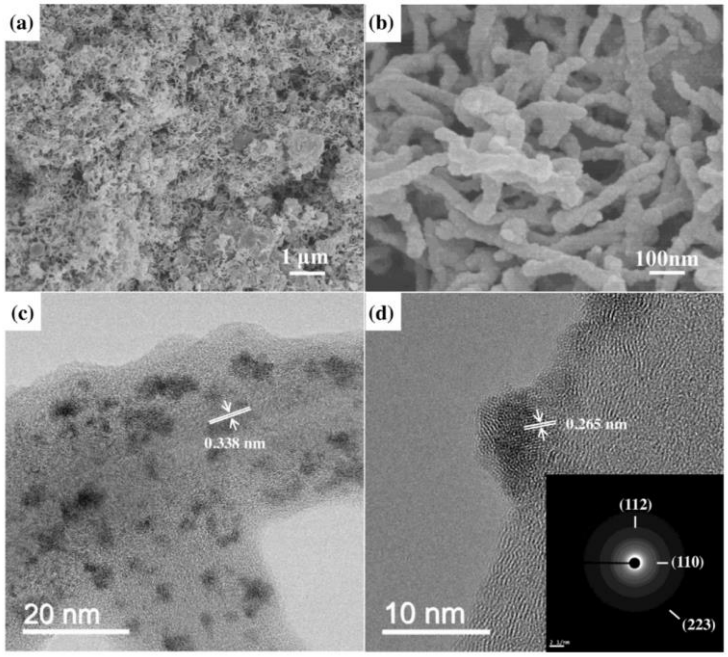

Fig 5.3 SEM and TEM patterns of Sn/SnO_2@C

The morphology of the Sn/SnO_2@C was examined using SEM, as shown in Fig5. 3(a) and (b). From Fig5. 3(a), it can be seen that a highly entangled network of curving nanofibers was formed, with some submicron particles incorporated in the fibers. Energy dispersive spectroscopy (EDS) analysis was employed to detect the chemical composition of these submicron particles (Fig5.4 and Table 1 in the Supporting Information), which revealed the presence of the elements Sn, C, O, and Pt. The corresponding quantified data are listed in Table 1, suggesting that these particles were mainly composed of metallic Sn, which is in accordance with the results from the XRD pattern. The Pt signal came from the sputtered Pt conducting film that covered the sample.

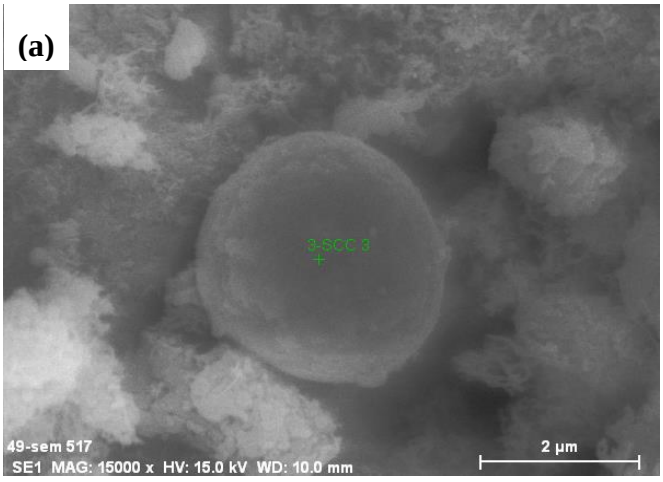

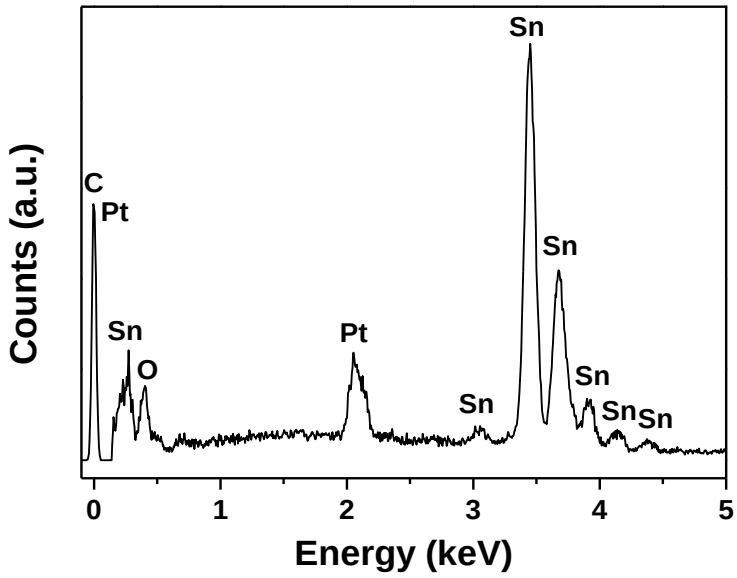

Fig 5 .4 (a) SEM image of a Sn particle surrounded by composite nanofibers. (b)EDS picture of the Sn particle.

Fig5. 3(b), the magnified SEM image, shows that the diameter of the nanofibers was around 40-50 nm, and the surfaces of the fibers were covered by small lumps and bumps rather than being smooth, indicating that these nanofibers were not pure CNTs.

Fig5. 3(c) and (d) contains HRTEM images of these nanofibers. As shown in Fig5. 3(c), small particles 2-7 nm in size were uniformly embedded in a layer of amorphous matrix which wrapped the CNTs, forming a core-shell structure. The aligned lattice fringes of the CNTs are also clearly illustrated, with a carbon layer separation of 0.338 nm, which is typical for multiwall CNTs. A magnified image of a CNT decorated with nanoparticles (Fig5. 3(d)) demonstrates that the nanoparticles are not crystallized very well, and the *d*-spacing of the nanoparticles is 0.265 nm, corresponding to the (002) planes of orthorhombic SnO_2. The selected area electron diffraction (SAED) pattern

(inset in Fig5.3(d)) of a SnO_2 nanoparticle presents the characteristics of polycrystalline rings. Such poor crystallization of the SnO_2 nanoparticles may be responsible for the absence of diffraction peaks of tin oxide in the XRD pattern. It is expected that the SnO_2 probably came from the oxidation of ultrafine Sn when the sample was exposed to air during the sample transfer and storage, given the extremely active nature of ultrafine Sn with such a small size (< 10 nm). And the ultrafine Sn particles may nuclear on the surface of CNTs, as revealed by Raman spectroscopy, which was conducted for the original CNT sample.

Table 5. 1 Quantified element analysis of the EDS spectrum

Element	Sn	C	O	Pt
Mass ratio (wt. %)	79.56	8.32	1.90	10.22
Atom ratio (at. %)	43.69	45.15	7.75	3.41

There are two main peaks located at ~ 1350 cm^{-1} and ~ 1580 cm^{-1}, as shown in Fig 5.5, which are attributed respectively to the disorder-induced D band and the graphic-like G band. The high intensity ratio I_D/I_G indicates low crystal quality of CNTs and high amount of amorphous carbon.

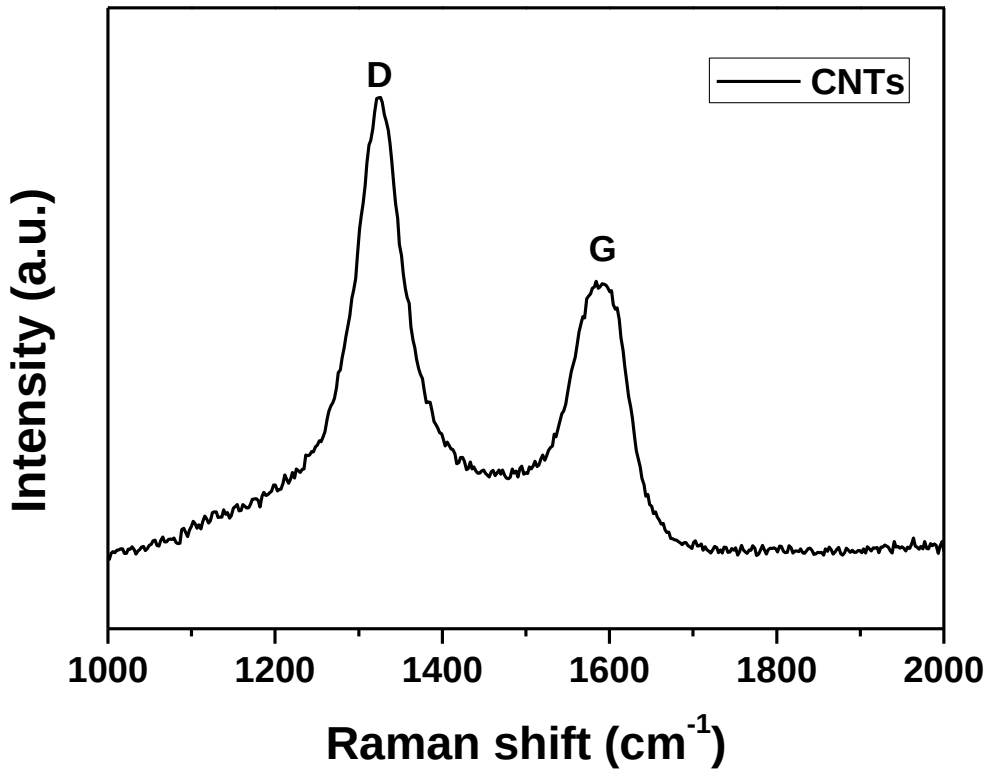

Fig 5.5 Raman spectrum of the original CNTs.

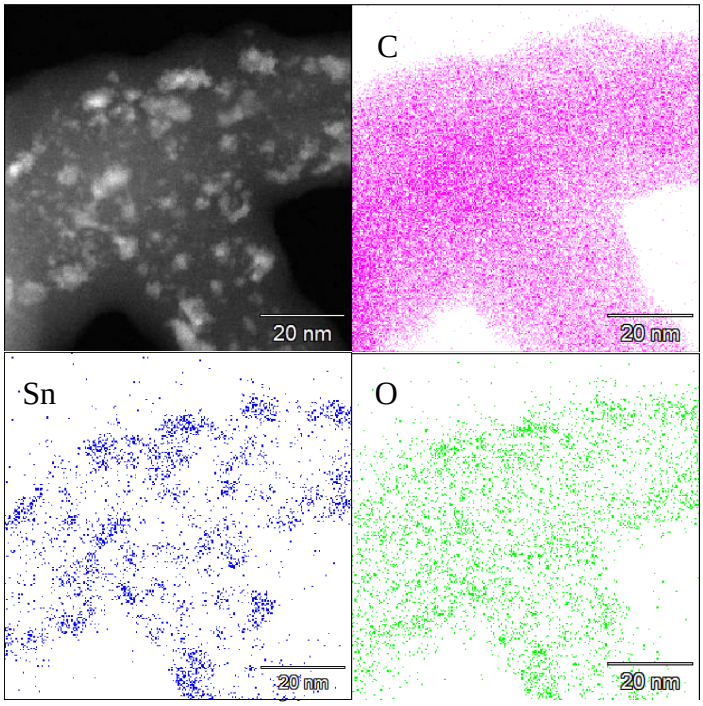

Fig 5.6 Dark-field scanning TEM image and EDS mapping of Sn/SnO_2@C.

A dark-field scanning TEM (STEM) image and EDS mapping of the core-shell structure of the CNTs encapsulated in an amorphous carbon matrix are shown in Fig5. 6 in the Supporting Information. Three elements, C (red), Sn (blue), and O (green), were selected for EDS mapping. The uniform distribution of the C element is evident, which indicates that the amorphous layer wrapped on the CNTs is carbon. This amorphous carbon layer may have come from the decomposition of PVP, which is beneficial for sustaining the volume changes of Sn-Li alloy in the extraction and insertion of Li^+. On the other hand, comparison of the EDS elemental maps for Sn and O with the STEM image indicates that the bright part of the STEM image, i.e. the nanoparticles embedded in the amorphous carbon matrix, is the Sn and O rich region. These observations suggest that the nanoparticles are composed of both Sn and O, which is well consistent with the SnO_2 phase of the nanoparticles, as determined by the lattice fringes in the TEM image and the SAED pattern of Fig4.4(d).

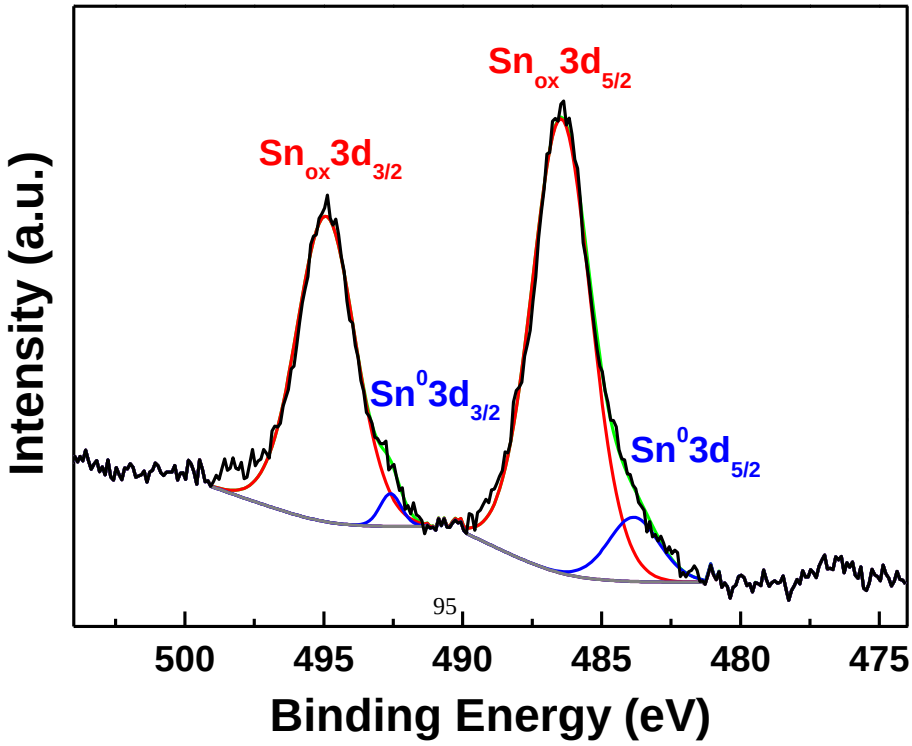

Fig 5.7 Sn 3d XPS spectrum of Sn/SnO_2@C.

XPS was carried out to investigate the surface composition and the chemical states of the elements in the as-prepared sample. Fig5.7 presents the XPS spectrum of the Sn 3d region. The peaks centered at 492.6 and 483.8 eV are assigned to Sn $3d_{3/2}$ and Sn $3d_{5/2}$, respectively; while the peaks at 494.9 and 486.4 eV are identical to the reported data for Sn 3d in SnO_2. The gap between the Sn $3d_{5/2}$ and Sn $3d_{3/2}$ levels is 8.5 eV, and the ratio of the areas of the two peaks is 1.5, which are approximately the same values as those in the standard spectrum of SnO_2.

It should be noted that the intensity of the SnO_2 peaks is greater than for Sn. This result could be explained as follows: the Sn particles incorporated in the network of nanofibers, as shown in the SEM image in Fig5. 4(a), had been partially oxidized in air during XPS analysis, although the remaining part of the Sn particles still exhibited strong diffraction peaks during the above XRD characterization (Fig 5.1). Similar phenomena were observed in Sn-based composites by different groups [111].

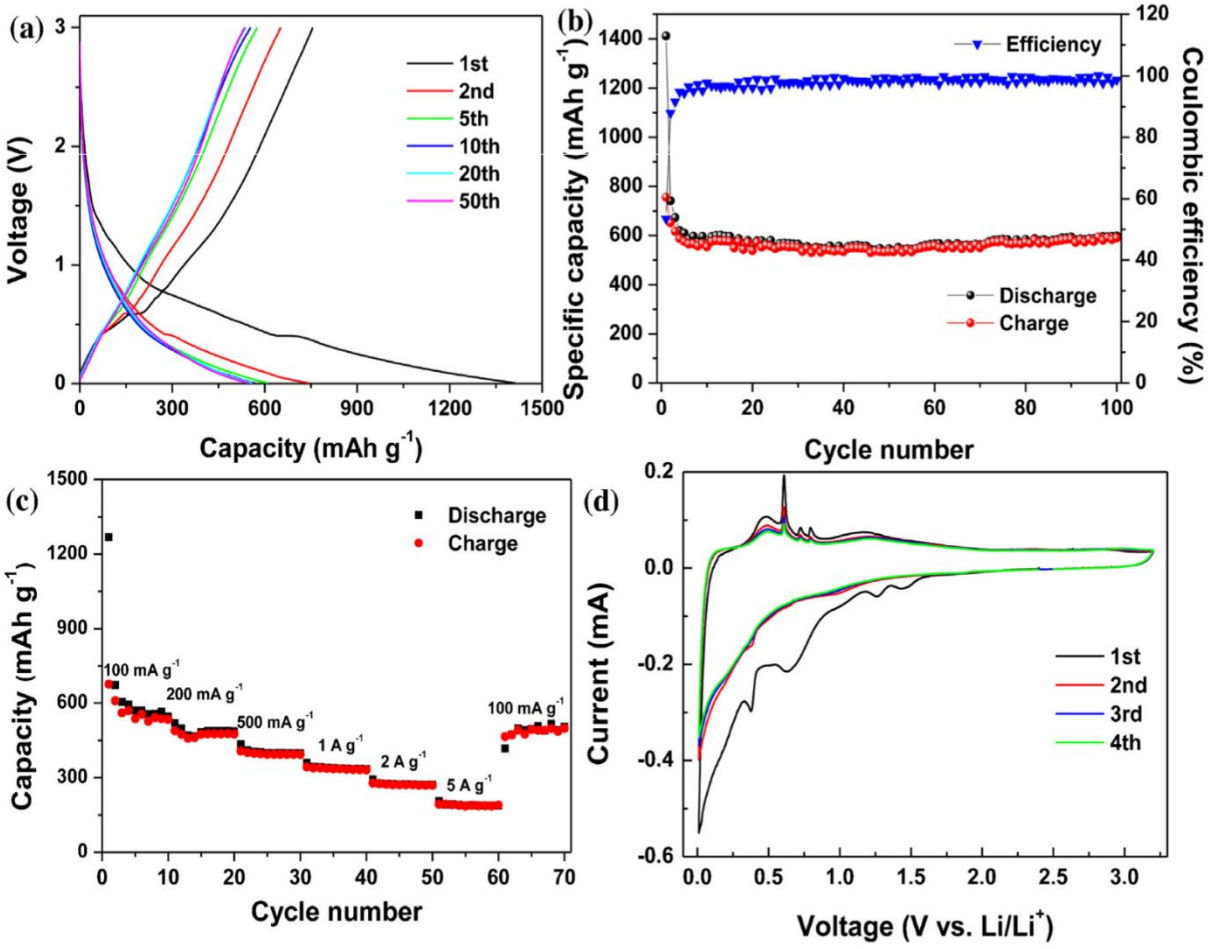

Fig 5. 8 (a) Charge-discharge curves for selected cycles and (b) cycling performance of Sn/SnO_2@C at the current density of 100 mA g^{-1}, (c) rate performance of Sn/SnO_2@C tested at different current densities from 100 mA g^{-1} to 5 A g^{-1}, (d) CV curves for the first 4 cycles of Sn/SnO_2@C at a scanning rate of 0.1 mV s^{-1}.

The electrochemical performance in lithium batteries of the Sn/SnO_2@C was investigated. Fig5. 8(a) shows the galvanostatic charge-discharge curves tested at a current density of 100 mA g^{-1}. The sample exhibited a high discharge capacity of 1412 mAh g^{-1} and a charge capacity of 756 mAh g^{-1} in the first cycle. It should be noted that the specific capacity values are calculated on the basis of the total mass of the

Sn/SnO_2@C composite material. The irreversible capacity loss (656 mAh g^{-1}) mainly originated from the formation of a solid electrolyte interphase (SEI) film [112]. From the charge-discharge results in the first cycle, the sample featured large Li^+ storage and an initial coulombic efficiency of around 54%, which is a value much higher than the capacities of graphite (300 mAh g^{-1}) and the pristine SnO_2 (645 mAh g^{-1}). It is believed that this excellent capacity should be attributed to the combination of SnO_2 particles with CNTs. As described above, SnO_2 nanopaticles 2-7 nm in size are embedded in an amorphous carbon matrix, which is firmly attached on the CNTs. The large surface area of the SnO_2 nanoparticles provides more reaction sites, and the small size could shorten the diffusion length of Li^+ during insertion and extraction. In addition, the good conductivity of CNTs may be helpful to the electron transfer, which can enhance the performance of the sample [113]. During the second cycle, the composite electrode delivers a charge capacity of 652 mAh g^{-1}, and the coulombic efficiency increases to 88%, which indicates high utilization of the active material in the composite. Fig5.8(b) exhibits the cycling performance of the sample. Specific capacity of 591 mAh g^{-1} is retained after 100 cycles, corresponding to coulombic efficiency higher than 98%, which is evidence of excellent performance and stability. Fig5.8(c) presents the rate capability of the sample at various current densities from 100 mA g^{-1} to 5 A g^{-1}, which delivers capacities of 535 mAh g^{-1} and 190 mAh g^{-1} at 100 mA g^{-1} and 5 A g^{-1}, respectively. When the current rate is reversed back to 100 mA g^{-1}, a stable capacity of 498 mAh g^{-1} can be restored, which suggests that the composite material can endure varying current densities while maintaining high stability in the meantime. Three

factors may contribute to the excellent rate capability: (1) the CNTs and the carbon matrix supply effective electronic conductivity; (2) the free spaces in the composite structure of Sn/SnO_2@C facilitate Li^+ diffusion between the active material and the electrolyte; (3) the ultrafine nature of the SnO_2 is beneficial for rapid Li^+ diffusion.

CV was carried out to investigate the electrochemical reactivity of the sample, and the results are displayed in Fig5.8(d). The interactions with Li^+, SnO_2, and carbonaceous species can be described by the following reactions:

$$4Li^+ + SnO_2 + 4e^- \rightarrow Sn + 2Li_2O \quad (1)$$

$$xLi^+ + Sn + xe^- \leftrightarrow Li_xSn\ (0 \leq x \leq 4.4) \quad (2)$$

$$yLi^+ + Carbon + ye^- \leftrightarrow Li_yC \quad (3)$$

During the first cycle there are a series of reduction peaks ranging from 0.3 to 1.4 V, which can be attributed to various reactions [114], including the transformation of SnO_2 and Li^+ to Sn and Li_2O, the formation of a series of Li–Sn alloys, and the Li^+ insertion in CNT layers (Eqs. (1) – (3)). From the second cycle, there is a pronounced decrease in the cathodic current, which can be attributed to the decomposition of the electrolyte and formation of a SEI layer in the first cycle [114]. In addition, a strong reduction peak can be observed close to 0 V, and a weak oxidation shoulder peak occurs near 0.2 V in the positive scan, corresponding to lithiation and delithiation of carbonaceous species. There are other anodic peaks that appear in the range from 0.4 to 1.2 V, which are related to the Li^+ extraction from Sn in the sample [115], although there are only two corresponding cathodic current peaks that can be observed in the CV cathodic scans.

The CV curves coincide very well except for the first cycle, indicating that Sn/SnO_2@C possesses good cycling stability. A CR2032 cell was disassembled after the LIB cycling and the active material was characterized by HRTEM. Lithiation and delithiation of Sn occur periodically during the cycling, as determined by the dark-field STEM image and EDS mapping of a Sn particle. It can be seen that the Sn particle remains to be metallic and does not convert to tin oxide after cycling. This phenomenon is explained by Eq. (2).

EIS was then conducted to investigate the interface reactions between the electrolyte solution and the electrode. The Nyquist plots of Sn/SnO_2@C before cycling and after the 5^{th} cycle are shown in Fig5. 4.

Usually there are a high frequency semicircle that is associated with Li^+ migration through the SEI film, and a middle frequency semicircle that is linked to the charge transfer reaction. In Fig5. 4, there is only one depressed semicircle instead of two semicircles in the high and middle frequency region, which is caused by the damage of the passivated film on the anode surface. The passivated film is destroyed by the de-intercalation of lithium ions, so that the SEI film decreases very rapidly. Thus the two

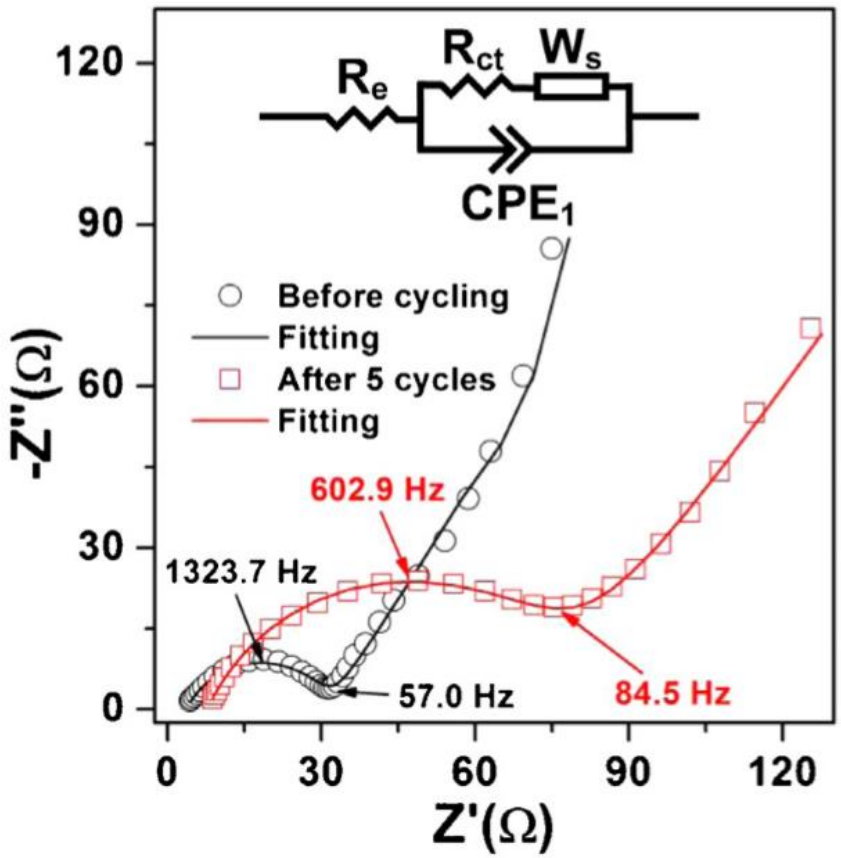

Fig 5. 9 EIS spectra of Sn/SnO_2@C before cycling and after 5 cycles. Inset is the equivalent circuit for fitting.

semicircles overlap and appear to be one. The inclined line at lower frequencies represents the Warburg impedance, which represents the lithium ion diffusion process within the electrodes [116-117]. The Nyquist plots were fitted by the equivalent circuit in the inset of Fig5. 4, where R_e represents the electrolyte and ohmic resistance, R_f and R_{ct} represent the surface film resistance and the charge transfer resistance, Q_1 and Q_2 represent the constant phase angle elements, while the Warburg impedance (W_s) relates to the Li^+ bulk diffusion resistance. The main fitted data from different cycles for the

sample are listed in Table 1. There is a small difference between the values of R_e (2.7—7.9 Ω) of the composite electrode before and after cycling. The value of R_{ct} increased from 19.6 to 70.9 Ω after 5 cycles of electrochemical tests. Generally, for the anode of a LIB, the value of R_{ct} reflects the compaction of particles in the composite anode, i.e. inter-particle contacts such as CNT-Sn contacts. Therefore the increase of R_{ct} can be attributed to the increase in the internal resistance of the electrode induced by the SEI film formation on the surface of particles of the active material during cycling [108]. R_f is the resistance that occurs while ions transfer through the SEI film.

Table5. 2

EIS fitting results for Sn/SnO_2@C electrode.

	Before cycling	After 5th cycle
R_e (Ω)	3.7	7.7
R_{ct} (Ω)	28.5	72.6

For active material with large volume variation during cycling, such as bare SnO_2, the interparticle contact resistance increases by cracking or crumbling of the particles during cycling.

On the other hand, the cracking or crumbling of particles creates fresh electrode/electrolyte interface, on which new SEI film could form during cycling afterwards, which usually leads to the increase of R_f. However, the value of R_f in Table 1 decreased from 8.9 to as small as 1.2 Ω after the 5^{th} cycle, which is indicative of the formation of a stabilized and thin SEI film. Therefor there is not much fresh electrode/electrolyte interface formed during cycling, i.e. no obvious cracking and

crumbling of particles. Such an SEI film can suppress the continuous electrolyte decomposition and the further growth of the SEI layer, making the electrode/electrolyte interface more stable [118]. And the integrity of the electrode was preserved for repeated lithium insertion and extraction. These results suggest that the excellent electrochemical performance of Sn/SnO_2@C is related both to the microstructure of the hybrid composite, which can buffer the volume expansion on the macrodomain, and to the construction of a desirable SEI film.

Conclusions

In summary, Sn/SnO_2@C anode composite nanofibers were successfully prepared by a facile annealing method. The composite consists of ultrafine (< 10 nm) SnO_2 nanoparticles embedded in the amorphous carbon coating layer on the CNTs, forming core-shell-structured composite nanofibers. The curving nanofibers form entangled networks, which surround the submicron Sn particles. This structure can buffer the volume expansion during charge/discharge by utilizing the ductile carbon matrix and the free spaces in the composite. A high reversible capacity, high coulombic efficiency, and excellent cyclability were achieved. The Sn/SnO_2@C composite exhibited an initial charge capacity of 756 mAh g^{-1} and can sustain stable cycling, with a charge capacity of 591 mAh g^{-1} retained after 100 cycles at 100 mA g^{-1}. In addition, the formation of a stable SEI film also contributed to the excellent cycling performance of the Sn/SnO_2@C by stabilizing the electrolyte/electrode interface. The excellent electrochemical performance indicates that Sn/SnO_2@C can be promising anode material for LIBs.

CHAPTER 6 BALL-MILLED FEP/GRAPHITE AS A LOW-COST ANODE MATERIAL FOR THE SODIUM-ION BATTERY

Introduction

Due to the increasing demand for consumer electronic devices and electric vehicles every year, and the severe environmental problems that are brought about by the use of traditional automobiles, development of high-energy storage devices has become a crucial issue[119]. Using lithium-ion batteries is an essential way to solve this issue[120-121], but lithium resources are not sufficient for widespread use. Because of the similarities in chemical properties between sodium and lithium, the sodium-ion battery has become the most available substitute for the lithium battery[122-127]. There are a variety of Na-ion anode materials, such as hard carbon[128-130], metal oxides[131-134], and metals which can alloy with sodium.

Tin (847 mAh g^{-1}), Antimony (664 mAh g^{-1}), and Phosphorus (2560 mAg g^{-1}) are attractive anode materials because of their high theoretical capacity. According to Qian's [82] report, the electrical conductivity and volume changes during significantly affect the performance of alloy compounds. Coating carbon or using carbon material as matrix are efficient methods to improve cycle life and rate performances in alloy anodes. For example, in Zhu's group[135], wood fiber was found to work as a mechanical buffer, and after 400 cycles, the retained capacity was around 339 mAh g^{-1}, 40% of the initial capacity. Wang's group[136] prepared Sn@carbon nanotube composite delivering a

capacity of 550 μAh cm^{-2} in the 100th cycle, which was 62% of the initial cycle. Ji et al[137] prepared an Sb/acetylene black composite which delivered a capacity of 73 $mAhg^{-1}$ after 70 cycles, with initial capacity of 624 mAh g^{-1}. Wu et al[138] synthesized Sb@C microspheres with 93% capacity retention after 100 cycles. P has a high theoretical capacity of 2596mAh g^{-1} in sodium battery. However, phosphorus has a low electrical conductivity of $1\times10^{-14}S^{-1}cm$, which results in poor cycling and rate performances. One efficient way is to synthesize P/carbon composites. Qian[58] et al. were the first to synthesize a phosphorus/C composite. Inspired by this, our group[59] prepared a red phosphorus/carbon nanotube (CNT) composite by simply hand grinding, which retained 76.6% of the initial capacity in the 10th cycle.

Our group[139] has studied iron phosphide (FeP) compound for application in sodium batteries, as it has high initial capacity of over 700 mAh g^{-1}. The capacity of a sample with poly(vinylidene difluoride) (PVDF) binder decreased to around 50 mAh g^{-1} after 40 cycles, because of the poor electrical conductivity. One efficient way to improve the FeP compound is to use carbon material to make a composite.

According to previous report, ball milling is a cheap and productive way to synthesis carbon coated composite[109, 140-142]. Our group's previous work[83, 139] demonstrate that after 20 hours milling at the rotation speed of 300rpm can get the nanoparticles about 30-100nm in size which can deliver well electrochemical performance. Based on the previous work and the equipment we have, FeP/graphite composite was prepared by this ball milling method at optimized condition with rotation speed 300rpm for 20 hours.

After that, graphite turns into an amorphous carbon matrix with FeP particles embedded in it. The amorphous carbon serves as a conductive and ductile matrix to connect particles and improve electrical conductivity, which significantly improves the cycling and rate performances. FeP/graphite will be a promising anode material in the future.

Experiment

Synthesis of FeP/graphite composite:

FeP/graphite composite was synthesis by a simple and productive low-energy ball-milling method. FeP/graphite composite powder was prepared by using FeP compound and commercial graphite. The FeP compound and graphite were mixed in the weight ratio of 7:3, respectively and then put into a hardened steel vial with 2 mm diameter milling balls. The weight ratio of balls to powder was 20:1. The vial was assembled in a glove box with water and oxygen lower than 0.1 ppm. The rotation conditions were set to 300 rpm for 20 hours.

Characterization:

The crystal structure was characterized by X-ray diffraction (XRD). The XRD patterns of the as-prepared powders were collected on a GBC MMA instrument with a Cu K_α source (λ = 1.541 Å), operating at 40 kV and 25 mA (step size = 0.002° s^{-1}). Scanning electron microscopy (JEOL JSM-7500FA) and transmission electron microscopy (TEM, JEOL 2011, 200 keV) were used to characterize the morphology of the samples. Raman spectra were collected using a HR800 JOBIN Yvon Horiba Raman spectrometer.

Results and discussion

In order to evaluate the electrochemical performance, the FeP/graphite and FeP electrodes were prepared by mixing 80wt% active material, 10wt% carbonyl–β-cyclodextrin, and 10wt% carbon black with de-ionised (DI) water to form the homogeneous slurry, which was then coated on Cu foil, dried at 80 ℃ for 10 hours in a vacuum oven, and then pressed under a pressure of 10 MPa. The electrodes were then punched into disks with 3 $mg \cdot cm^{-2}$ active material loaded on them. The electrolyte was $NaClO_4$ in a mixture of ethylene carbonate (EC) and diethyl carbonate (DEC) in the ratio of 1:1 by volume. The cell was assembled in an Ar-filled glove box with water and oxygen content lower than 0.1 ppm. The assembled cells were tested on a Land cycler (Wuhan) at the current density of 50 mA g^{-1} within the voltage window of 0-1.5 V (vs. Na/Na^+). C-rate tests were conducted under current densities from 50 mA g^{-1} to 2500 mA g^{-1} within the voltage range of 0-1.5 V (vs. Na/Na^+).

Result and discussion

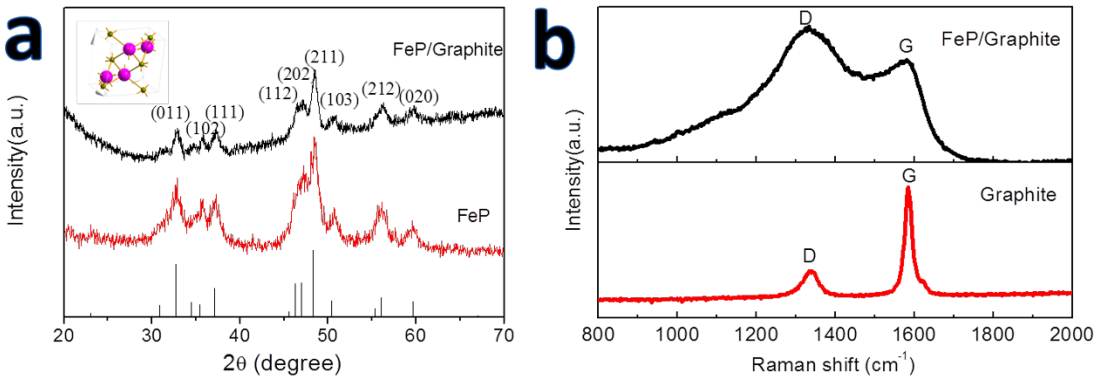

Fig6.1. (a) XRD patterns of FeP/graphite and FeP, and (b) Raman spectra of FeP/graphite composite and graphite.

Fig6. 1(a) shows the XRD patterns of FeP/graphite and pure FeP compound. All the diffraction peaks are indexed to orthorhombic phase (JPCDS No.65-2595) with space group *Pnma*. The decreased peak intensity of FeP/graphite compared to the original FeP is due to the smaller grain size after 20 hours of low energy ball milling. Based on the Debye-Scherrer [143]formula, $D = K\gamma B^{-1}\cos\theta$, K is a numerical factor referred to as the crystallite-shape factor, γ is the wavelength of the X-ray, B is the half maximum width of X-ray peak and θ is Bragg angle. After calculating, the FeP crystal size in FeP/graphite was found to be about 14.5 nm.

In order to further analyze the structure of FeP/graphite composite, Raman spectroscopy was used. As shown in Fig6. 1(b), the Raman spectrum of FeP/graphite has two obvious bands at 1330 cm^{-1} and 1570 cm^{-1}, corresponding to the D and G bands of carbon, respectively. The D band assigned to the A_{1g} mode corresponds to the defects in the structure, and the G band is assigned to the first-order scattering of the E_{2g} mode in the graphitic structure. [82, 144-145]The intensity ratio of D/G (I_D/I_G) characterizes the ratio of disordered to ordered carbon in the sample. The intensity ratio from the spectrum for pure graphite is 0.28, while the I_D/I_G ratio of FeP/graphite is 1.18. This phenomenon indicates that the graphite has been transformed to disordered carbon after 20 hours of ball milling, which is consistent with the XRD pattern, where no graphite peak can be observed. There are no significant Fe-P bands in the spectrum, which indicates that the FeP particles might be covered with amorphous carbon. In addition,

there is no band for P-P or P-C, and no obviously peak shifting can be observed, which indicates that the FeP compound has not decomposed or reacted with graphite after ball milling.

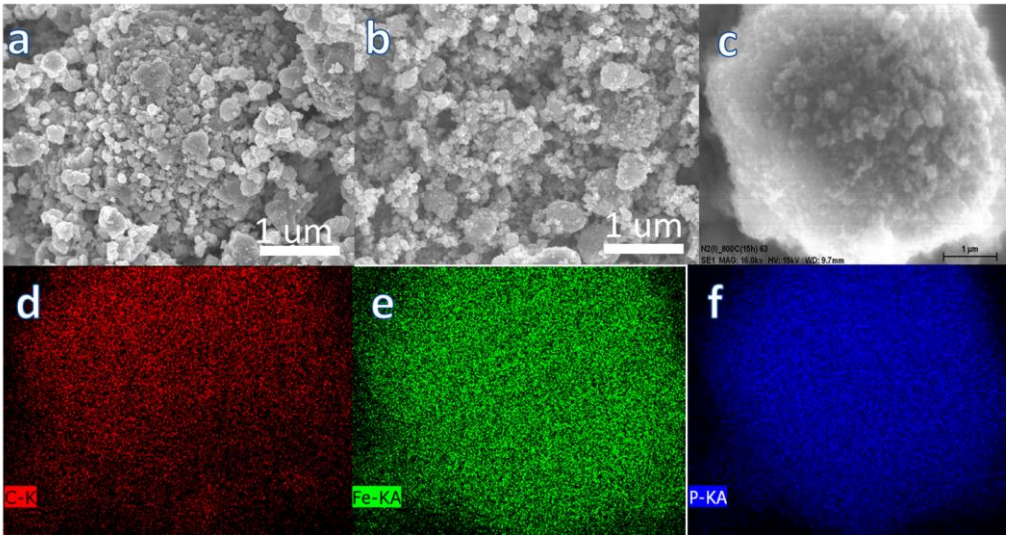

Fig 6.2. SEM images of FeP compound (a) and FeP/graphite composite (b, c). (d-f) are the EDS mapping of the FeP/graphite composite particle in (c).

To explore the morphology of FeP/graphite after ball milling, scanning electron microscopy (SEM) and energy dispersive spectroscopy (EDS) mapping were conducted. Fig6. 2(a) and (b) shows the surface morphology of FeP compound and FeP/graphite composite powder after 20 hours of ball milling. Compared to the original FeP compound, the average size of secondary particles in the FeP/graphite composite is decreased from 100-150 nm to about 100 nm, which is consistent with the decreased peak intensity in the XRD pattern. The irregular-shaped original particles have become spherical, which is advantageous for battery application. In order to confirm that the FeP was mixed homogeneously with the carbon, an individual particle in Fig6. 2(b)

was explored by EDS mapping, as shown in Fig6. 2(c). It seems that the carbon was distributed homogeneously over the FeP compound particles, which is in accordance with the Raman result that no Fe-P or P-P band could be observed

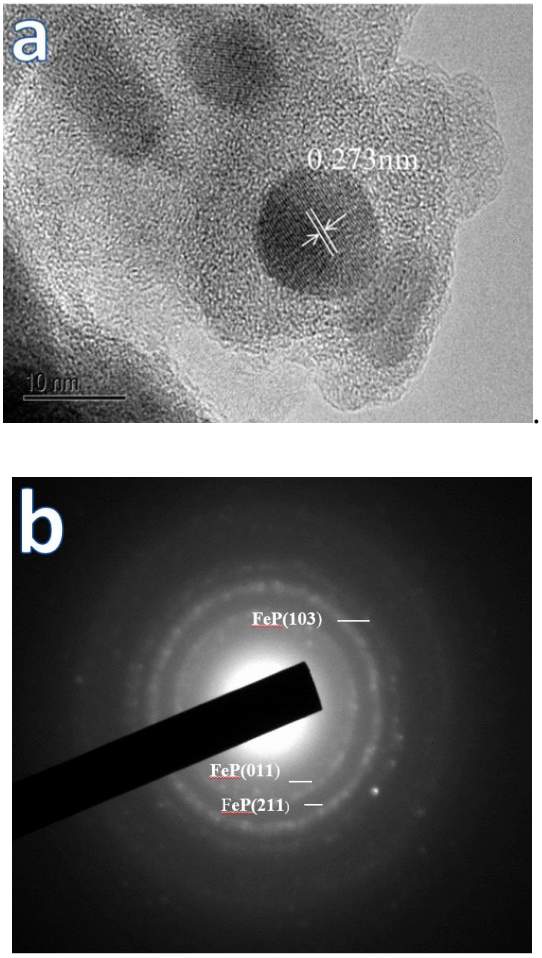

Fig 6.3 TEM image (a) and SAED pattern (b) of FeP/graphite composite.

To further confirm that the FeP compound particles were embedded in amorphous carbon, transmission electron microscopy (TEM) and selected area electron diffraction (SAED) analysis (Fig6. 3) were conducted on the as-prepared composite powder. In Fig6. 3(a), lattice fringes with *d*-spacing of 0.273 nm, corresponding to the (011) planes

of FeP, are observed. There are no lattice fringes between the FeP and the amorphous carbon, which indicates that no bonding was formed between the FeP and the carbon[146], which is in line with the Raman spectra. The FeP nanocrystals are embedded in the amorphous carbon matrix. The electron diffraction rings, corresponding to the (011), (211), and (103) planes of FeP, are shown in Fig6. 3(b). On combining the evidence above, it is clear that, after simple ball milling, the graphite is converted to amorphous carbon with FeP crystalline particles 10 nm in size homogeneously embedded inside. The amorphous carbon can serve as a conductive matrix to enable well electric contact between particles so that can improve the cycling and rate performance.

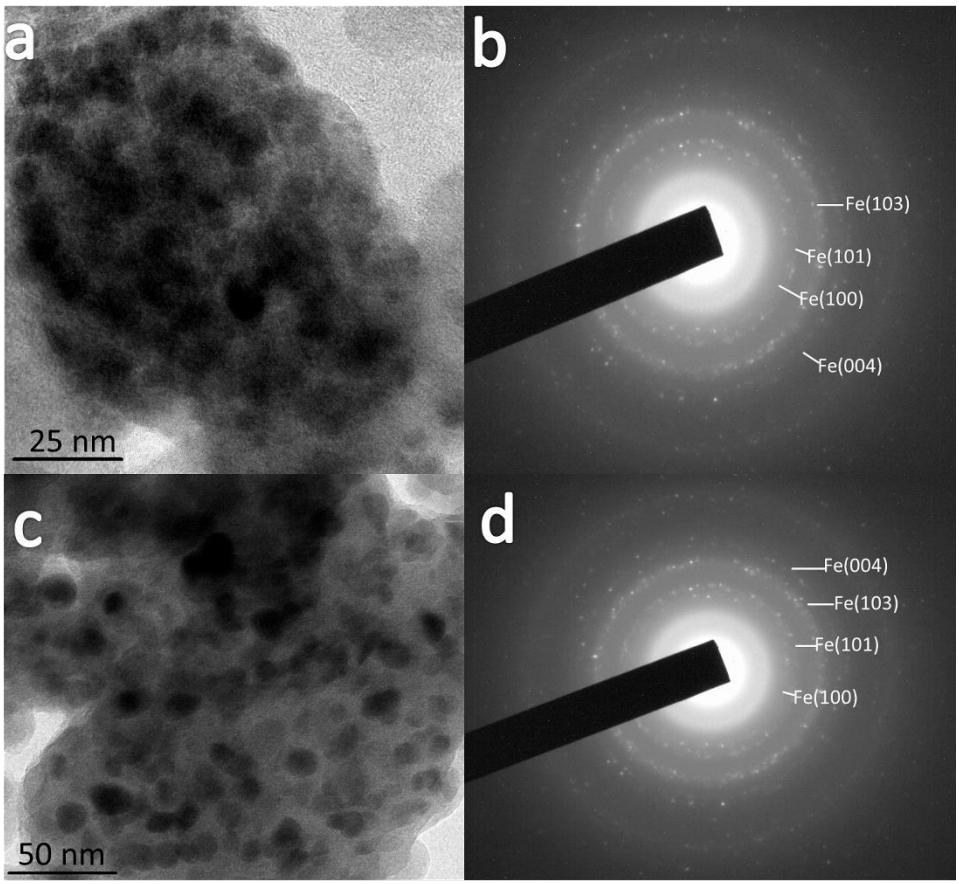

Fig 6. 4 TEM and SEAD images of FeP (a,b) and FeP/graphite (c,d) electrodes charged at 1.5V.

As shown in Figure6.4, transmission electron microscopy (TEM) and selected area electron diffraction (SAED) analysis were used to analyze the structure and phase of FeP and FeP/graphite electrodes after cycling for two cycles and charged at 1.5V. The electron diffraction pattern of FeP and FeP/graphite are similar. After one cycle there is only one crystal existed. The electro diffraction rings are corresponding to (101),(100),(004),(103) phase of polycrystal Fe, which indicate that after one cycle FeP might has decomposed into Fe and amorphous P which is in accordant with the report [139]. As can be seen from the TEM image in Fig6.4(a), after cycling FeP electrode particles have pulverized into small nanoparticles, and isolated which results in poor cycling and rate performance. Comparing to FeP electrode, the FeP/graphite (Fig6.4(b)) electrode has Fe particles imbedded in the amorphous carbon, thus amorphous carbon can serve as conductive matrix to maintain the contact between particles hinder aggregation during cycling and improve electrical conductivity.

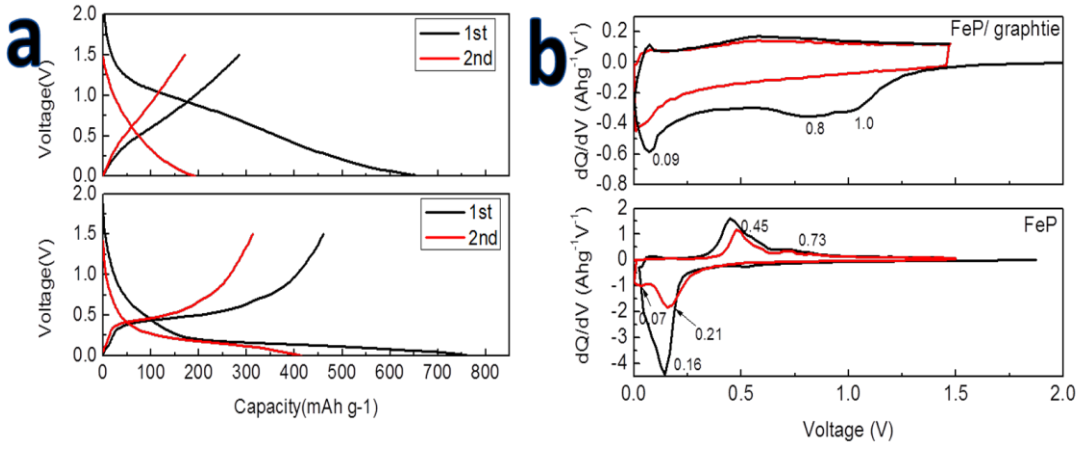

Fig6.5. Charge-discharge curves at the current density of 50 mA g^{-1} (a) and corresponding *dQ*/*dV* plots (b) in the first two cycles for FeP/graphite and FeP electrodes.

The discharge and charge performances of de-alloying and alloying of Na-ion with FeP compound and FeP/graphite composite was examined in 1.0 mol L^{-1} $NaClO_4$ in EC-DEC solution (1:1 v/v). The loading mass of active material was ~3 mg cm^{-2}. Fig6. 4(a) displays the discharge and charge profiles (within the voltage range of 0-1.5 V vs. Na/Na^+) of FeP compound and FeP/graphite under the current density of 50 mA g^{-1}. The discharge capacity of FeP/graphite composite in the first cycle is 658.4 mAh g^{-1}. The calculated specific capacity based on the ratio of FeP compound is 823 $mAhg^{-1}$, which is close to the theoretical capacity of 893.3 mAh g^{-1} and higher than the pure FeP capacity of 764.5 mAh g^{-1}. During the initial discharge of FeP/graphite, a slope between 0.8 -1.0V can be clearly observed, which corresponds to the formation of the solid electrolyte interphase (SEI). The plateau at 0.09 V is similar to that of FeP compound, which is due to Na alloying with P to form Na_3P. [139]

In order to compare the chemical reactivity of the FeP/graphite composite to FeP compound, and to analysis the mechanism of in both samples, differential capacity (*dQ*/*dV*) curves were plotted, as shown in Fig6. 4(b).

In the first discharge process, two cathodic peaks are observed, i.e., one wide peak (0.8-1.0 V versus Na/Na^+) and one sharp peak (0.09 V versus Na/Na^+). The first wide current cathodic peak can be ascribed to the decomposition of electrolyte and the formation of the SEI. The second small peak is assigned to the alloy step of sodium ion insertion

reaction to form Na_3P and NaC_x.[147] It is obviously observed an anodic peak at 0.05 V which corresponds to the desodiation. The overall reaction process can be summarized as follows:

$$3Na^+ + 3e^- + Fe + P \leftrightarrow Na_3P + Fe \quad (1)$$

$$xC + Na^+ + e^- \leftrightarrow NaC_x \quad (2)$$

The *dQ*/*dV* curve of FeP compound plotted in Fig6. 4(b) shows that there are two cathodic peaks at 0.07 V and 0.21 V, and two anodic peaks at 0.44 V and 0.76 V in the second cycle, which is similar to the reported curve.[139] These peaks correspond to the alloying and de-alloying reactions between Na^+ and FeP compound.

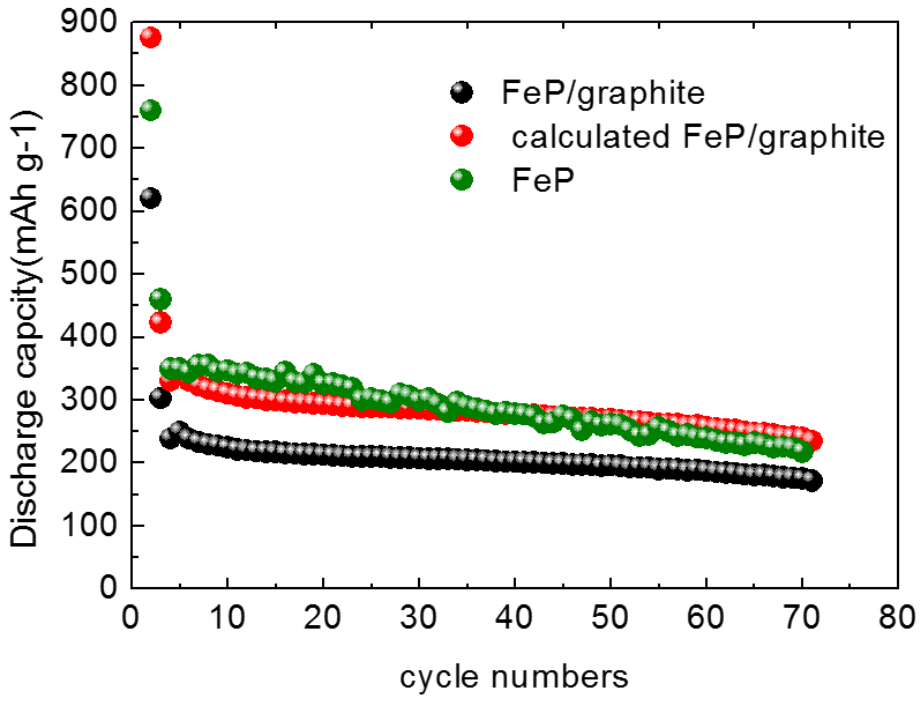

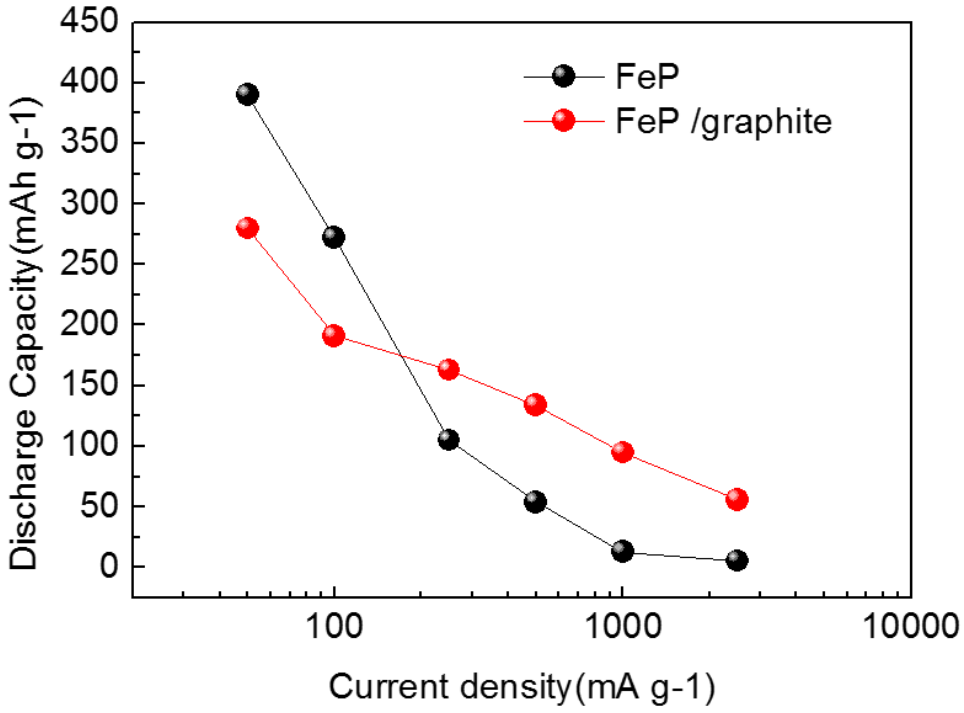

Fig6.6. Cycling performances of FeP/graphite at 50mA g^{-1}, calculated FeP/graphite, and FeP compound (a). Rate performance of FeP compound and FeP/graphite composite.

Fig. 6.6(a) shows the cycling performances of FeP/graphite and FeP compound. The discharge capacity of FeP at the 70th cycle is 217 mAh g^{-1}, which represents 47% capacity retention with respect to the second cycle. The FeP/graphite composite shows an obvious improvement in cycling performance. The 70th discharge capacity is 175 mAh g^{-1}, which is 58% of the second cycle. The reason for the lower capacity of FeP/graphite compared to FeP is the limited specific capacity of graphite. If the capacity is calculated based on the weight of FeP only, after 70 cycles, the capacity remains 240 mAh g^{-1}, which is higher than that of pristine FeP. The main reason for the improvement in cycling performance is that the amorphous carbon can connect the isolated particles

and improve the electrical conductivity. Fig6. 5(b) shows the rate capabilities of FeP and FeP/graphite electrodes. The average discharge capacities are 390/280, 272/191, 105/163, 54/134, 13/95, and 5.5/56 mAh g^{-1} at current densities of 50, 100, 250, 500, 1000, and 2500mA g^{-1} for the FeP and FeP/graphite electrodes, respectively. It is obvious that the rate capacity of FeP/graphite is better than that of FeP, especially when the current density increases to over 500 mA g^{-1}. This is probably because the amorphous carbon can serve as conductive matrix to maintain the contact between particles hinder aggregation during cycling and improve electrical conductivity.

Conclusion

In summary, FeP/graphite composite was prepared by a simple low-energy ball-milling method. The results demonstrate that, after ball milling with graphite, the cycling and high-rate performances of FeP compound are greatly improved: the discharge capacity of FeP/graphite represents 58% capacity retention with respect to the second cycle; when the current density increases to 500 mA g^{-1}, FeP/graphite composite still delivered 134 mAh g^{-1}, which is more than twice the capacity of the FeP compound. The graphite was converted to amorphous carbon after ball milling, which serves as a conductive matrix to well connect the particles, hinder aggregation and improve the electrical conductivity. Our results suggest that FeP/graphite composite will be a cheap and productive anode material for sodium ion batteries in the future.

CHAPTER 7 CONCLUSION

The environmental friendly and efficient energy power lithium ion battery have been widely applied in various area such as laptop, electric cars, mobile phones and so on. Meanwhile, the lithium ion battery is utilized as high efficient energy storage system combining with sorts of clean renewable energy such as solar energy, wind energy and tidy energy. The great success of using Lithium ion battery, results in the shortage of Lithium source such as high-energy cobalt-based materials which lead to the increasing of the cost of Lithium-ion battery. Comparing to lithium source, the sodium element is rich existed and evenly distributed in the earth curst. Besides, the sodium ion and lithium ion have many similarities in chemical properties which makes the development of high energy density sodium ion battery become more and more important.

This master thesis discussed some promising anode materials-silicon based composite, Sn based composite and FeP/graphite composite applied in lithium ion batteries and sodium ion batteries. The main thought is using simple low cost productive synthesis method to alloy-carbon composite. The carbon materials and other metal element can efficiently hinder the volume change of the original material and improve the conductivity as well. Therefore, the electrical chemical performances can be efficiently improved.

The silicon based anode material /Fe/Sn/Carbon composite delivers an excellent electrochemical performance that the capacity of first cycle is 1274mAh g^{-1} and after cycling for 1000 cycles, the capacity remains 620 mAh g^{-1}. This is due to the frogspawn

like structure in which the amorphous matrix can efficiently hinder the volume change, besides the continuously carbon network can efficiently hinder the agglomeration of particles upon prolonged cycling.

The Tin based anode material Sn/SnO_2@C nanofiber consists of ultrafine SnO_2 nanoparticles embedded in the amorphous carbon coating layer on the CNTs delivered a high reversible capacity of 756 mAh g^{-1} and remained 591 mAh g^{-1} after cycling for 100 cycles. This is due to the ductile carbon matrix can buffer the volume expansion during cycling.

Graphite was used to improve the electrochemical performance of FeP compound. The composite was prepared by productive and cheap ball milling method. The result demonstrated that by using the carbon material, the cycling performance and rate performance can be efficiently improved. For example, when the current density increases to 500 mA g^{-1} the discharge capacity of FeP/graphite represents 134 mAh g^{-1}, which is more than twice the capacity of the FeP compound.

This thesis mainly focused on the alloy based anode materials. The main problem of applying alloy compound is the huge volume change resulting in pulverization which will lead to the poor electrical chemical performances. The core strategy is to use carbon material and active or inactive metal to hinder the volume and improve the conductivity.

The results prove the feasibility of the strategy. These alloy based composites are promising anode materials. The anticipation of the lithium ion battery and sodium ion battery are bright.

OUTLOOK

In the future, more work will be carried on anode material, such as NiP2/CNT for sodium ion battery. The NiP_2 compound and NiP_2/CNT will be prepared by high-energy ball milling method. The crystal structure of the NiP_2/CNT will be analyzed by XRD. The microstructure and morphology of the NiP_2/CNT will be observed by field emission scanning electron microscopy (FESEM) and transmission electron microscopy (TEM). The Raman spectra analyses will also be employed to characterize the as-prepared composite. The mechanism of sodiation in NiP_2/CNT composite will be analyzed by ex-situ TEM and in-situ XRD (Whether Na_2NiP_2 will form or whether the amorphous P will form).

PUBLICATIONS

1.Li, W.-J.; **Yang, Q.-R.**; Chou, S.-L.; Wang, J.-Z.; Liu, H.-K., Cobalt phosphide as a new anode material for sodium storage. *Journal of Power Sources* **2015**, *294*, 627-632

2**.Yang, Q.-R**.; Li, W.-J.; Chou, S.-L.; Wang, J.-Z.; Liu, H.-K., Ball-milled FeP/graphite as a low-cost anode material for the sodium-ion battery. *RSC Advances* **2015**, *5* (98), 80536-80541.

3.Hu, Y.; **Yang, Q.-R**.; Ma, J.; Chou, S.-L.; Zhu, M.; Li, Y., Sn/SnO_2@C composite nanofibers as advanced anode for lithium-ion batteries. *Electrochimica Acta* **2015**, *186*, 271-276.

Reference

1. Tarascon, J.-M.; Armand, M., Issues and challenges facing rechargeable lithium batteries. *Nature* **2001,** *414* (6861), 359-367.
2. Etacheri, V.; Marom, R.; Elazari, R.; Salitra, G.; Aurbach, D., Challenges in the development of advanced Li-ion batteries: a review. *Energy & Environmental Science* **2011,** *4* (9), 3243.
3. Mizushima, K.; Jones, P.; Wiseman, P.; Goodenough, J., LixCoO2 (0< x<-1): A new cathode material for batteries of high energy density. *Materials Research Bulletin* **1980,** *15* (6), 783-789.
4. Yabuuchi, N.; Kubota, K.; Dahbi, M.; Komaba, S., Research development on sodium-ion batteries. *Chemical reviews* **2014,** *114* (23), 11636-82.
5. Ohzuku, T.; Iwakoshi, Y.; Sawai, K., Formation of Lithium-Graphite Intercalation Compounds in Nonaqueous Electrolytes and Their Application as a Negative Electrode for a Lithium Ion (Shuttlecock) Cell. *Journal of The Electrochemical Society* **1993,** *140* (9), 2490-2498.
6. Sawai, K.; Ohzuku, T.; Hirai, T., Natural graphite as an anode for rechargeable nonaqueous cells. *Chem. Express* **1990,** *5*, 837.
7. Doeff, M. M.; Ma, Y.; Visco, S. J.; De Jonghe, L. C., Electrochemical insertion of sodium into carbon. *Journal of The Electrochemical Society* **1993,** *140* (12), L169-L170.
8. de las Casas, C.; Li, W., A review of application of carbon nanotubes for lithium ion battery anode material. *Journal of Power Sources* **2012,** *208*, 74-85.
9. Cui, L.-F.; Hu, L.; Choi, J. W.; Cui, Y., Light-weight free-standing carbon nanotube-silicon films for anodes of lithium ion batteries. *ACS nano* **2010,** *4* (7), 3671-3678.
10. Ko, S.; Lee, J. I.; Yang, H. S.; Park, S.; Jeong, U., Mesoporous CuO Particles Threaded with CNTs for High-Performance Lithium-Ion Battery Anodes. *Advanced Materials* **2012,** *24* (32), 4451-4456.
11. Wang, H.; Cui, L.-F.; Yang, Y.; Sanchez Casalongue, H.; Robinson, J. T.; Liang, Y.; Cui, Y.; Dai, H., Mn3O4− graphene hybrid as a high-capacity anode material for lithium ion batteries. *Journal of the American Chemical Society* **2010,** *132* (40), 13978-13980.
12. Wu, Z.-S.; Ren, W.; Wen, L.; Gao, L.; Zhao, J.; Chen, Z.; Zhou, G.; Li, F.; Cheng, H.-M., Graphene anchored with Co3O4 nanoparticles as anode of lithium ion batteries with enhanced reversible capacity and cyclic performance. *ACS nano* **2010,** *4* (6), 3187-3194.
13. Kheirabadi, N.; Shafiekhani, A., Graphene/Li-ion battery. *Journal of Applied Physics* **2012,** *112* (12), 124323.
14. Qie, L.; Chen, W. M.; Wang, Z. H.; Shao, Q. G.; Li, X.; Yuan, L. X.; Hu, X. L.; Zhang, W. X.; Huang, Y. H., Nitrogen-doped porous carbon nanofiber webs as anodes for lithium ion batteries with a superhigh capacity and rate capability. *Advanced materials* **2012,** *24* (15), 2047-2050.
15. Ponrouch, A.; Goñi, A.; Palacín, M. R., High capacity hard carbon anodes for sodium ion batteries in additive free electrolyte. *Electrochemistry communications* **2013,** *27*, 85-88.
16. Liu, Y.; Xue, J.; Zheng, T.; Dahn, J., Mechanism of lithium insertion in hard carbons prepared by pyrolysis of epoxy resins. *Carbon* **1996,** *34* (2), 193-200.
17. Buiel, E.; Dahn, J., Li-insertion in hard carbon anode materials for Li-ion batteries. *Electrochimica acta* **1999,** *45* (1), 121-130.
18. Stevens, D.; Dahn, J., The mechanisms of lithium and sodium insertion in carbon materials. *Journal of The Electrochemical Society* **2001,** *148* (8), A803-A811.
19. Park, C.-M.; Kim, J.-H.; Kim, H.; Sohn, H.-J., Li-alloy based anode materials for Li secondary batteries.

Chemical Society reviews **2010,** *39* (8), 3115-3141.

20. Kim, H.; Cho, J., Superior lithium electroactive mesoporous Si@ Carbon core− shell nanowires for lithium battery anode material. *Nano letters* **2008,** *8* (11), 3688-3691.

21. Su, X.; Wu, Q.; Li, J.; Xiao, X.; Lott, A.; Lu, W.; Sheldon, B. W.; Wu, J., Silicon-Based Nanomaterials for Lithium-Ion Batteries: A Review. *Advanced Energy Materials* **2014,** *4* (1), n/a-n/a.

22. Chan, C. K.; Peng, H.; Liu, G.; McIlwrath, K.; Zhang, X. F.; Huggins, R. A.; Cui, Y., High-performance lithium battery anodes using silicon nanowires. *Nat Nanotechnol* **2008,** *3* (1), 31-5.

23. Cui, L.-F.; Ruffo, R.; Chan, C. K.; Peng, H.; Cui, Y., Crystalline-amorphous core− shell silicon nanowires for high capacity and high current battery electrodes. *Nano letters* **2008,** *9* (1), 491-495.

24. Kim, H.; Han, B.; Choo, J.; Cho, J., Three-dimensional porous silicon particles for use in high-performance lithium secondary batteries. *Angewandte Chemie* **2008,** *120* (52), 10305-10308.

25. Kim, H.; Seo, M.; Park, M. H.; Cho, J., A critical size of silicon nano-anodes for lithium rechargeable batteries. *Angewandte Chemie* **2010,** *49* (12), 2146-9.

26. Landi, B. J.; Ganter, M. J.; Cress, C. D.; DiLeo, R. A.; Raffaelle, R. P., Carbon nanotubes for lithium ion batteries. *Energy & Environmental Science* **2009,** *2* (6), 638-654.

27. Wang, W.; Epur, R.; Kumta, P. N., Vertically aligned silicon/carbon nanotube (VASCNT) arrays: Hierarchical anodes for lithium-ion battery. *Electrochemistry Communications* **2011,** *13* (5), 429-432.

28. Wang, W.; Kumta, P. N., Nanostructured hybrid silicon/carbon nanotube heterostructures: reversible high-capacity lithium-ion anodes. *Acs Nano* **2010,** *4* (4), 2233-2241.

29. Gohier, A.; Laik, B.; Kim, K. H.; Maurice, J. L.; Pereira-Ramos, J. P.; Cojocaru, C. S.; Van Tran, P., High-rate capability silicon decorated vertically aligned carbon nanotubes for Li-ion batteries. *Advanced materials* **2012,** *24* (19), 2592-7.

30. Novoselov, K. S.; Geim, A. K.; Morozov, S.; Jiang, D.; Zhang, Y.; Dubonos, S. a.; Grigorieva, I.; Firsov, A., Electric field effect in atomically thin carbon films. *science* **2004,** *306* (5696), 666-669.

31. Huang, X.; Qi, X.; Boey, F.; Zhang, H., Graphene-based composites. *Chemical Society reviews* **2012,** *41* (2), 666-86.

32. Jung, J.-W.; Ryu, W.-H.; Shin, J.; Park, K.; Kim, I.-D., Glassy Metal Alloy Nanofiber Anodes Employing Graphene Wrapping Layer: Toward Ultralong-Cycle-Life Lithium-Ion Batteries. *ACS nano* **2015,** *9* (7), 6717-6727.

33. Zhou, X.; Yin, Y. X.; Wan, L. J.; Guo, Y. G., Facile synthesis of silicon nanoparticles inserted into graphene sheets as improved anode materials for lithium-ion batteries. *Chemical communications* **2012,** *48* (16), 2198-200.

34. Wang, J.-Z.; Zhong, C.; Chou, S.-L.; Liu, H.-K., Flexible free-standing graphene-silicon composite film for lithium-ion batteries. *Electrochemistry Communications* **2010,** *12* (11), 1467-1470.

35. Xiang, H.; Zhang, K.; Ji, G.; Lee, J. Y.; Zou, C.; Chen, X.; Wu, J., Graphene/nanosized silicon composites for lithium battery anodes with improved cycling stability. *Carbon* **2011,** *49* (5), 1787-1796.

36. Wang, B.; Li, X.; Zhang, X.; Luo, B.; Jin, M.; Liang, M.; Dayeh, S. A.; Picraux, S.; Zhi, L., Adaptable silicon–carbon nanocables sandwiched between reduced graphene oxide sheets as lithium ion battery anodes. *ACS nano* **2013,** *7* (2), 1437-1445.

37. Shen, X.; Mu, D.; Chen, S.; Xu, B.; Wu, B.; Wu, F., Si/mesoporous carbon composite as an anode material for lithium ion batteries. *Journal of Alloys and Compounds* **2013,** *552*, 60-64.

38. Ng, S. H.; Wang, J.; Wexler, D.; Chew, S. Y.; Liu, H. K., Amorphous carbon-coated silicon nanocomposites: a low-temperature synthesis via spray pyrolysis and their application as high-capacity anodes for lithium-ion batteries. *The Journal of Physical Chemistry C* **2007,** *111* (29), 11131-11138.

39. Wang, G.; Sun, L.; Bradhurst, D.; Zhong, S.; Dou, S.; Liu, H., Nanocrystalline NiSi alloy as an anode material for lithium-ion batteries. *Journal of Alloys and Compounds* **2000,** *306* (1), 249-252.

40. Liu, W.-R.; Wu, N.-L.; Shieh, D.-T.; Wu, H.-C.; Yang, M.-H.; Korepp, C.; Besenhard, J. O.; Winter, M., Synthesis and Characterization of Nanoporous NiSi-Si Composite Anode for Lithium-Ion Batteries. *Journal of The Electrochemical Society* **2007,** *154* (2), A97.

41. Cao, F. F.; Deng, J. W.; Xin, S.; Ji, H. X.; Schmidt, O. G.; Wan, L. J.; Guo, Y. G., Cu-Si Nanocable Arrays as High-Rate Anode Materials for Lithium-Ion Batteries. *Advanced materials* **2011,** *23* (38), 4415-4420.

42. Kim, B.-C.; Uono, H.; Satou, T.; Fuse, T.; Ishihara, T.; Ue, M.; Senna, M., Cyclic properties of Si-Cu/carbon nanocomposite anodes for Li-ion secondary batteries. *Journal of The Electrochemical Society* **2005,** *152* (3), A523-A526.

43. Maranchi, J.; Hepp, A.; Evans, A.; Nuhfer, N.; Kumta, P., Interfacial properties of the a-Si/Cu: active–inactive thin-film anode system for lithium-ion batteries. *Journal of the Electrochemical Society* **2006,** *153* (6), A1246-A1253.

44. Kim, Y.-L.; Lee, H.-Y.; Jang, S.-W.; Lim, S.-H.; Lee, S.-J.; Baik, H.-K.; Yoon, Y.-S.; Lee, S.-M., Electrochemical characteristics of Co–Si alloy and multilayer films as anodes for lithium ion microbatteries. *Electrochimica Acta* **2003,** *48* (18), 2593-2597.

45. Kim, J.-B.; Lee, H.-Y.; Lee, K.-S.; Lim, S.-H.; Lee, S.-M., Fe/Si multi-layer thin film anodes for lithium rechargeable thin film batteries. *Electrochemistry Communications* **2003,** *5* (7), 544-548.

46. Kim, J.-B.; Jun, B.-S.; Lee, S.-M., Improvement of capacity and cyclability of Fe/Si multilayer thin film anodes for lithium rechargeable batteries. *Electrochimica Acta* **2005,** *50* (16-17), 3390-3394.

47. Kim, H.; Choi, J.; Sohn, H. J.; Kang, T., The Insertion Mechanism of Lithium into Mg2Si Anode Material for Li-Ion Batteries. *Journal of the Electrochemical Society* **1999,** *146* (12), 4401-4405.

48. He, Y.; Yu, X.; Wang, Y.; Li, H.; Huang, X., Alumina-coated patterned amorphous silicon as the anode for a lithium-ion battery with high coulombic efficiency. *Advanced materials* **2011,** *23* (42), 4938-41.

49. MacEachern, L.; Dunlap, R.; Obrovac, M., A Combinatorial Investigation of Fe-Si-Zn Thin Film Negative Electrodes for Li-Ion Batteries. *Journal of The Electrochemical Society* **2015,** *162* (1), A229-A234.

50. Choi, N.-S.; Yao, Y.; Cui, Y.; Cho, J., One dimensional Si/Sn-based nanowires and nanotubes for lithium-ion energy storage materials. *Journal of Materials Chemistry* **2011,** *21* (27), 9825-9840.

51. Wang, H.; Huang, H.; Chen, L.; Wang, C.; Yan, B.; Yu, Y.; Yang, Y.; Yang, G., Preparation of Si/Sn-based nanoparticles composited with carbon fibers and improved electrochemical performance as anode materials. *ACS Sustainable Chemistry & Engineering* **2014,** *2* (10), 2310-2317.

52. Hatchard, T.; Dahn, J., Study of the Electrochemical Performance of Sputtered Si1− x Sn x Films. *Journal of The Electrochemical Society* **2004,** *151* (10), A1628-A1635.

53. Ahn, H.-J.; Kim, Y.-S.; Park, K.-W.; Seong, T.-Y., Use of Sn–Si nanocomposite electrodes for Li rechargeable batteries. *Chem. Commun.* **2005,** (1), 43-45.

54. Lee, H.-Y.; Lee, S.-M., Graphite–FeSi alloy composites as anode materials for rechargeable lithium batteries. *Journal of power sources* **2002,** *112* (2), 649-654.

55. Obrovac, M.; Chevrier, V., Alloy negative electrodes for Li-ion batteries. *Chemical reviews* **2014,** *114* (23), 11444-11502.

56. Hembram, K.; Jung, H.; Yeo, B. C.; Pai, S. J.; Kim, S.; Lee, K.-R.; Han, S. S., Unraveling the atomistic sodiation mechanism of black phosphorus for sodium ion batteries by first-principles calculations. *The Journal of Physical Chemistry C* **2015,** *119* (27), 15041-15046.

57. Park, C. M.; Sohn, H. J., Black phosphorus and its composite for lithium rechargeable batteries. *Advanced materials* **2007,** *19* (18), 2465-2468.

58. Qian, J.; Wu, X.; Cao, Y.; Ai, X.; Yang, H., High capacity and rate capability of amorphous phosphorus for sodium ion batteries. *Angewandte Chemie* **2013,** *52* (17), 4633-6.

59. Li, W. J.; Chou, S. L.; Wang, J. Z.; Liu, H. K.; Dou, S. X., Simply mixed commercial red phosphorus and carbon nanotube composite with exceptionally reversible sodium-ion storage. *Nano letters* **2013,** *13* (11), 5480-4.

60. Zhu, Y.; Wen, Y.; Fan, X.; Gao, T.; Han, F.; Luo, C.; Liou, S.-C.; Wang, C., Red Phosphorus–Single-Walled Carbon Nanotube Composite as a Superior Anode for Sodium Ion Batteries. *ACS nano* **2015,** *9* (3), 3254-3264.

61. Sun, L.-Q.; Li, M.-J.; Sun, K.; Yu, S.-H.; Wang, R.-S.; Xie, H.-M., Electrochemical Activity of Black Phosphorus as an Anode Material for Lithium-Ion Batteries. *The Journal of Physical Chemistry C* **2012,** *116* (28), 14772-14779.

62. Thompson, A.; Whittingham, M., Transition metal phosphorus trisulfides as battery cathodes. *Materials Research Bulletin* **1977,** *12* (7), 741-744.

63. Alcantara, R.; Tirado, J.; Jumas, J.; Monconduit, L.; Olivier-Fourcade, J., Electrochemical reaction of lithium with CoP 3. *Journal of power sources* **2002,** *109* (2), 308-312.

64. Silva, D.; Crosnier, O.; Ouvrard, G.; Greedan, J.; Safa-Sefat, A.; Nazar, L., Reversible lithium uptake by FeP2. *Electrochemical and solid-state letters* **2003,** *6* (8), A162-A165.

65. Souza, D.; Pralong, V.; Jacobson, A.; Nazar, L., A reversible solid-state crystalline transformation in a metal phosphide induced by redox chemistry. *Science* **2002,** *296* (5575), 2012-2015.

66. Gillot, F.; Boyanov, S.; Dupont, L.; Doublet, M.-L.; Morcrette, M.; Monconduit, L.; Tarascon, J.-M., Electrochemical reactivity and design of NiP2 negative electrodes for secondary Li-ion batteries. *Chemistry of materials* **2005,** *17* (25), 6327-6337.

67. Hwang, H.; Kim, M. G.; Kim, Y.; Martin, S. W.; Cho, J., The electrochemical lithium reactions of monoclinic ZnP 2 material. *Journal of Materials Chemistry* **2007,** *17* (30), 3161-3166.

68. Bichat, M.-P.; Pascal, J.-L.; Gillot, F.; Favier, F., Electrochemical lithium insertion in Zn3P2 zinc phosphide. *Chemistry of materials* **2005,** *17* (26), 6761-6771.

69. Kim, Y.-U.; Lee, C. K.; Sohn, H.-J.; Kang, T., Reaction mechanism of tin phosphide anode by mechanochemical method for lithium secondary batteries. *Journal of The Electrochemical Society* **2004,** *151* (6), A933-A937.

70. Gillot, F.; Ménétrier, M.; Bekaert, E.; Dupont, L.; Morcrette, M.; Monconduit, L.; Tarascon, J.-M., Vanadium diphosphides as negative electrodes for secondary Li-ion batteries. *Journal of power sources* **2007,** *172* (2), 877-885.

71. Pralong, V.; Souza, D.; Leung, K.; Nazar, L., Reversible lithium uptake by CoP 3 at low potential: role of the anion. *Electrochemistry communications* **2002,** *4* (6), 516-520.

72. Zhang, Z.; Yang, J.; Nuli, Y.; Wang, B.; Xu, J., CoP x synthesis and lithiation by ball-milling for anode materials of lithium ion cells. *Solid State Ionics* **2005,** *176* (7), 693-697.

73. Boyanov, S.; Bernardi, J.; Bekaert, E.; Ménétrier, M.; Doublet, M.-L.; Monconduit, L., P-redox mechanism at the origin of the high lithium storage in NiP2-based batteries. *Chemistry of Materials* **2008,** *21* (2), 298-308.

74. Xiang, J.; Tu, J.; Wang, X.; Huang, X.; Yuan, Y.; Xia, X.; Zeng, Z., Electrochemical performances of nanostructured Ni 3 P–Ni films electrodeposited on nickel foam substrate. *Journal of Power Sources* **2008,** *185* (1), 519-525.

75. Lu, Y.; Tu, J.-p.; Gu, C.-d.; Wang, X.-l.; Mao, S. X., In situ growth and electrochemical characterization versus lithium of a core/shell-structured Ni 2 P@ C nanocomposite synthesized by a facile organic-phase

strategy. *Journal of Materials Chemistry* **2011,** *21* (44), 17988-17997.

76. Fullenwarth, J.; Darwiche, A.; Soares, A.; Donnadieu, B.; Monconduit, L., NiP 3: a promising negative electrode for Li-and Na-ion batteries. *Journal of Materials Chemistry A* **2014,** *2* (7), 2050-2059.

77. Wang, C.; Ding, T.; Sun, Y.; Zhou, X.; Liu, Y.; Yang, Q., Ni 12 P 5 nanoparticles decorated on carbon nanotubes with enhanced electrocatalytic and lithium storage properties. *Nanoscale* **2015**.

78. Song, J.; Yu, Z.; Gordin, M. L.; Hu, S.; Yi, R.; Tang, D.; Walter, T.; Regula, M.; Choi, D.; Li, X., Chemically bonded phosphorus/graphene hybrid as a high performance anode for sodium-ion batteries. *Nano letters* **2014,** *14* (11), 6329-6335.

79. Lu, Y.; Wang, X.; Mai, Y.; Xiang, J.; Zhang, H.; Li, L.; Gu, C.; Tu, J.; Mao, S. X., Ni2P/Graphene Sheets as Anode Materials with Enhanced Electrochemical Properties versus Lithium. *The Journal of Physical Chemistry C* **2012,** *116* (42), 22217-22225.

80. Lu, A.; Zhang, X.; Chen, Y.; Xie, Q.; Qi, Q.; Ma, Y.; Peng, D.-L., Synthesis of Co 2 P/graphene nanocomposites and their enhanced properties as anode materials for lithium ion batteries. *Journal of Power Sources* **2015,** *295*, 329-335.

81. Dahbi, M.; Yabuuchi, N.; Kubota, K.; Tokiwa, K.; Komaba, S., Negative electrodes for Na-ion batteries. *Physical Chemistry Chemical Physics* **2014,** *16* (29), 15007-15028.

82. Kim, Y.; Park, Y.; Choi, A.; Choi, N. S.; Kim, J.; Lee, J.; Ryu, J. H.; Oh, S. M.; Lee, K. T., An amorphous red phosphorus/carbon composite as a promising anode material for sodium ion batteries. *Adv Mater* **2013,** *25* (22), 3045-9.

83. Li, W.; Chou, S. L.; Wang, J. Z.; Kim, J. H.; Liu, H. K.; Dou, S. X., Sn4+x P3 @ amorphous Sn-P composites as anodes for sodium-ion batteries with low cost, high capacity, long life, and superior rate capability. *Advanced materials* **2014,** *26* (24), 4037-42.

84. Kim, Y.; Kim, Y.; Choi, A.; Woo, S.; Mok, D.; Choi, N. S.; Jung, Y. S.; Ryu, J. H.; Oh, S. M.; Lee, K. T., Tin phosphide as a promising anode material for Na-ion batteries. *Adv Mater* **2014,** *26* (24), 4139-44.

85. Fan, X.; Mao, J.; Zhu, Y.; Luo, C.; Suo, L.; Gao, T.; Han, F.; Liou, S. C.; Wang, C., Superior Stable Self-Healing SnP3 Anode for Sodium-Ion Batteries. *Advanced Energy Materials* **2015,** *5* (18).

86. Li, W.-J.; Yang, Q.-R.; Chou, S.-L.; Wang, J.-Z.; Liu, H.-K., Cobalt phosphide as a new anode material for sodium storage. *Journal of Power Sources* **2015,** *294*, 627-632.

87. Aurbach, D.; Talyosef, Y.; Markovsky, B.; Markevich, E.; Zinigrad, E.; Asraf, L.; Gnanaraj, J. S.; Kim, H.-J., Design of electrolyte solutions for Li and Li-ion batteries: a review. *Electrochimica Acta* **2004,** *50* (2), 247-254.

88. Zhang, S. S., A review on electrolyte additives for lithium-ion batteries. *Journal of Power Sources* **2006,** *162* (2), 1379-1394.

89. Lu, L.; Han, X.; Li, J.; Hua, J.; Ouyang, M., A review on the key issues for lithium-ion battery management in electric vehicles. *Journal of power sources* **2013,** *226*, 272-288.

90. Pan, H.; Hu, Y.-S.; Chen, L., Room-temperature stationary sodium-ion batteries for large-scale electric energy storage. *Energy & Environmental Science* **2013,** *6* (8), 2338-2360.

91. Gao, X.-P.; Yang, H.-X., Multi-electron reaction materials for high energy density batteries. *Energy & Environmental Science* **2010,** *3* (2), 174-189.

92. Liu, W.-R.; Wu, N.-L.; Shieh, D.-T.; Wu, H.-C.; Yang, M.-H.; Korepp, C.; Besenhard, J.; Winter, M., Synthesis and characterization of nanoporous NiSi-Si composite anode for lithium-ion batteries. *Journal of The Electrochemical Society* **2007,** *154* (2), A97-A102.

93. He, Y.; Yu, X.; Wang, Y.; Li, H.; Huang, X., Alumina-Coated Patterned Amorphous Silicon as the Anode for a Lithium-Ion Battery with High Coulombic Efficiency. *Advanced Materials* **2011,** *23* (42),

4938-4941.
94. Etacheri, V.; Marom, R.; Elazari, R.; Salitra, G.; Aurbach, D., Challenges in the development of advanced Li-ion batteries: a review. *Energy & Environmental Science* **2011,** *4* (9), 3243-3262.
95. Tirado, J. L., Inorganic materials for the negative electrode of lithium-ion batteries: state-of-the-art and future prospects. *Materials Science and Engineering: R: Reports* **2003,** *40* (3), 103-136.
96. Goodenough, J. B.; Kim, Y., Challenges for rechargeable Li batteries†. *Chemistry of Materials* **2009,** *22* (3), 587-603.
97. Su, Y.; Li, S.; Wu, D.; Zhang, F.; Liang, H.; Gao, P.; Cheng, C.; Feng, X., Two-dimensional carbon-coated graphene/metal oxide hybrids for enhanced lithium storage. *ACS nano* **2012,** *6* (9), 8349-8356.
98. Wen, Z.; Lu, G.; Mao, S.; Kim, H.; Cui, S.; Yu, K.; Huang, X.; Hurley, P. T.; Mao, O.; Chen, J., Silicon nanotube anode for lithium-ion batteries. *Electrochemistry Communications* **2013,** *29*, 67-70.
99. Zhong, C.; Wang, J.; Chen, Z.; Liu, H., SnO2–graphene composite synthesized via an ultrafast and environmentally friendly microwave autoclave method and its use as a superior anode for lithium-ion batteries. *The Journal of Physical Chemistry C* **2011,** *115* (50), 25115-25120.
100. Wang, C.; Zhou, Y.; Ge, M.; Xu, X.; Zhang, Z.; Jiang, J., Large-scale synthesis of SnO2 nanosheets with high lithium storage capacity. *Journal of the American Chemical Society* **2009,** *132* (1), 46-47.
101. Wang, Y.; Huang, Z. X.; Shi, Y.; Wong, J. I.; Ding, M.; Yang, H. Y., Designed hybrid nanostructure with catalytic effect: beyond the theoretical capacity of SnO2 anode material for lithium ion batteries. *Scientific reports* **2015,** *5*.
102. Lou, X. W.; Li, C. M.; Archer, L. A., Designed synthesis of coaxial SnO2@ carbon hollow nanospheres for highly reversible lithium storage. *Advanced Materials* **2009,** *21* (24), 2536-2539.
103. Chen, P.; Wu, F.; Wang, Y., Four-Layer Tin–Carbon Nanotube Yolk–Shell Materials for High-Performance Lithium-Ion Batteries. *ChemSusChem* **2014,** *7* (5), 1407-1414.
104. Tian, Q.; Zhang, Z.; Yang, L.; Hirano, S. i., Encapsulation of SnO2/Sn Nanoparticles into Mesoporous Carbon Nanowires and its Excellent Lithium Storage Properties. *Particle & Particle Systems Characterization* **2015,** *32* (3), 381-388.
105. Chen, J.; Yang, L.; Fang, S.; Zhang, Z.; Deb, A.; Hirano, S.-i., Sn-contained N-rich carbon nanowires for high-capacity and long-life lithium storage. *Electrochimica Acta* **2014,** *127*, 390-396.
106. Zhou, X.; Wan, L. J.; Guo, Y. G., Binding SnO2 Nanocrystals in Nitrogen-Doped Graphene Sheets as Anode Materials for Lithium-Ion Batteries. *Advanced materials* **2013,** *25* (15), 2152-2157.
107. Tian, Q.; Zhang, Z.; Chen, J.; Yang, L.; Hirano, S.-i., Carbon nanowires@ ultrathin SnO 2 nanosheets@ carbon composite and its lithium storage properties. *Journal of Power Sources* **2014,** *246*, 587-595.
108. Guo, Z.; Zhao, Z.; Liu, H.; Dou, S., Electrochemical lithiation and de-lithiation of MWNT–Sn/SnNi nanocomposites. *Carbon* **2005,** *43* (7), 1392-1399.
109. Zhu, Z.; Wang, S.; Du, J.; Jin, Q.; Zhang, T.; Cheng, F.; Chen, J., Ultrasmall Sn nanoparticles embedded in nitrogen-doped porous carbon as high-performance anode for lithium-ion batteries. *Nano letters* **2013,** *14* (1), 153-157.
110. Ding, S.; Chen, J. S.; Qi, G.; Duan, X.; Wang, Z.; Giannelis, E. P.; Archer, L. A.; Lou, X. W., Formation of SnO2 hollow nanospheres inside mesoporous silica nanoreactors. *Journal of the American Chemical Society* **2010,** *133* (1), 21-23.
111. Yue, W.; Yang, S.; Liu, Y.; Yang, X., A facile synthesis of mesoporous graphene-tin composites as high-performance anodes for lithium-ion batteries. *Materials Research Bulletin* **2013,** *48* (4), 1575-1580.
112. Su, D.; Ahn, H.-J.; Wang, G., SnO 2@ graphene nanocomposites as anode materials for Na-ion

batteries with superior electrochemical performance. *Chemical communications* **2013,** *49* (30), 3131-3133.

113. Park, M. S.; Wang, G. X.; Kang, Y. M.; Wexler, D.; Dou, S. X.; Liu, H. K., Preparation and Electrochemical Properties of SnO2 Nanowires for Application in Lithium-Ion Batteries. *Angewandte Chemie* **2007,** *119* (5), 764-767.

114. Idota, Y.; Kubota, T.; Matsufuji, A.; Maekawa, Y.; Miyasaka, T., Tin-based amorphous oxide: a high-capacity lithium-ion-storage material. *Science* **1997,** *276* (5317), 1395-1397.

115. Winter, M.; Besenhard, J. O., Electrochemical lithiation of tin and tin-based intermetallics and composites. *Electrochimica Acta* **1999,** *45* (1), 31-50.

116. Huang, Y.; Wu, D.; Han, S.; Li, S.; Xiao, L.; Zhang, F.; Feng, X., Assembly of Tin Oxide/Graphene Nanosheets into 3D Hierarchical Frameworks for High-Performance Lithium Storage. *ChemSusChem* **2013,** *6* (8), 1510-1515.

117. Liang, J.; Zhao, Y.; Guo, L.; Li, L., Flexible free-standing graphene/SnO2 nanocomposites paper for Li-ion battery. *ACS applied materials & interfaces* **2012,** *4* (11), 5742-5748.

118. Ji, L.; Gu, M.; Shao, Y.; Li, X.; Engelhard, M. H.; Arey, B. W.; Wang, W.; Nie, Z.; Xiao, J.; Wang, C., Controlling SEI Formation on SnSb-Porous Carbon Nanofibers for Improved Na Ion Storage. *Advanced Materials* **2014,** *26* (18), 2901-2908.

119. Yang, Z.; Zhang, J.; Kintner-Meyer, M. C.; Lu, X.; Choi, D.; Lemmon, J. P.; Liu, J., Electrochemical energy storage for green grid. *Chemical reviews* **2011,** *111* (5), 3577-3613.

120. Whittingham, M. S., Lithium batteries and cathode materials. *Chemical reviews* **2004,** *104* (10), 4271-4302.

121. Zhang, W.-J., A review of the electrochemical performance of alloy anodes for lithium-ion batteries. *Journal of Power Sources* **2011,** *196* (1), 13-24.

122. Palomares, V.; Serras, P.; Villaluenga, I.; Hueso, K. B.; Carretero-González, J.; Rojo, T., Na-ion batteries, recent advances and present challenges to become low cost energy storage systems. *Energy & Environmental Science* **2011,** *5* (3), 5884-5901.

123. Ellis, B. L.; Nazar, L. F., Sodium and sodium-ion energy storage batteries. *Current Opinion in Solid State and Materials Science* **2012,** *16* (4), 168-177.

124. Ponrouch, A.; Dedryvère, R.; Monti, D.; Demet, A. E.; Mba, J. M. A.; Croguennec, L.; Masquelier, C.; Johansson, P.; Palacín, M. R., Towards high energy density sodium ion batteries through electrolyte optimization. *Energy & Environmental Science* **2013,** *6* (8), 2361-2369.

125. Slater, M. D.; Kim, D.; Lee, E.; Johnson, C. S., Sodium-Ion Batteries. *Advanced Functional Materials* **2013,** *23* (8), 947-958.

126. Kim, Y.; Ha, K. H.; Oh, S. M.; Lee, K. T., High-Capacity Anode Materials for Sodium-Ion Batteries. *Chemistry-A European Journal* **2014,** *20* (38), 11980-11992.

127. Yabuuchi, N.; Kubota, K.; Dahbi, M.; Komaba, S., Research development on sodium-ion batteries. *Chemical reviews* **2014,** *114* (23), 11636-11682.

128. Ponrouch, A.; Goñi, A. R.; Palacín, M. R., High capacity hard carbon anodes for sodium ion batteries in additive free electrolyte. *Electrochemistry Communications* **2013,** *27*, 85-88.

129. Zhao, J.; Zhao, L.; Chihara, K.; Okada, S.; Yamaki, J.-i.; Matsumoto, S.; Kuze, S.; Nakane, K., Electrochemical and thermal properties of hard carbon-type anodes for Na-ion batteries. *Journal of Power Sources* **2013,** *244*, 752-757.

130. Dahbi, M.; Nakano, T.; Yabuuchi, N.; Ishikawa, T.; Kubota, K.; Fukunishi, M.; Shibahara, S.; Son, J.-Y.; Cui, Y.-T.; Oji, H.; Komaba, S., Sodium carboxymethyl cellulose as a potential binder for hard-carbon

negative electrodes in sodium-ion batteries. *Electrochemistry Communications* **2014,** *44*, 66-69.
131. Xiong, H.; Slater, M. D.; Balasubramanian, M.; Johnson, C. S.; Rajh, T., Amorphous TiO2 nanotube anode for rechargeable sodium ion batteries. *The Journal of Physical Chemistry Letters* **2011,** *2* (20), 2560-2565.
132. Gu, M.; Kushima, A.; Shao, Y.; Zhang, J.-G.; Liu, J.; Browning, N. D.; Li, J.; Wang, C., Probing the failure mechanism of SnO2 nanowires for sodium-ion batteries. *Nano letters* **2013,** *13* (11), 5203-5211.
133. Hu, M.; Jiang, Y.; Sun, W.; Wang, H.; Jin, C.; Yan, M., Reversible conversion-alloying of Sb2O3 as a high-capacity, high-rate, and durable anode for sodium ion batteries. *ACS applied materials & interfaces* **2014,** *6* (21), 19449-55.
134. Grinbom, G.; Duveau, D.; Gershinsky, G.; Monconduit, L.; Zitoun, D., Silicon/Hollow γ-Fe2O3Nanoparticles as Efficient Anodes for Li-Ion Batteries. *Chemistry of Materials* **2015,** *27* (7), 2703-2710.
135. Zhu, H.; Jia, Z.; Chen, Y.; Weadock, N.; Wan, J.; Vaaland, O.; Han, X.; Li, T.; Hu, L., Tin anode for sodium-ion batteries using natural wood fiber as a mechanical buffer and electrolyte reservoir. *Nano letters* **2013,** *13* (7), 3093-100.
136. Xie, X.; Kretschmer, K.; Zhang, J.; Sun, B.; Su, D.; Wang, G., Sn@CNT nanopillars grown perpendicularly on carbon paper: A novel free-standing anode for sodium ion batteries. *Nano Energy* **2015,** *13*, 208-217.
137. Hou, H.; Yang, Y.; Zhu, Y.; Jing, M.; Pan, C.; Fang, L.; Song, W.; Yang, X.; Ji, X., An Electrochemical Study of Sb/Acetylene Black Composite as Anode for Sodium-Ion Batteries. *Electrochimica Acta* **2014,** *146*, 328-334.
138. Wu, L.; Lu, H.; Xiao, L.; Ai, X.; Yang, H.; Cao, Y., Electrochemical properties and morphological evolution of pitaya-like Sb@C microspheres as high-performance anode for sodium ion batteries. *J. Mater. Chem. A* **2015,** *3* (10), 5708-5713.
139. Li, W. J.; Chou, S. L.; Wang, J. Z.; Liu, H. K.; Dou, S. X., A new, cheap, and productive FeP anode material for sodium-ion batteries. *Chemical communications* **2015,** *51* (17), 3682-5.
140. Kim, Y.; Kim, Y.; Choi, A.; Woo, S.; Mok, D.; Choi, N. S.; Jung, Y. S.; Ryu, J. H.; Oh, S. M.; Lee, K. T., Tin Phosphide as a Promising Anode Material for Na-Ion Batteries. *Advanced materials* **2014,** *26* (24), 4139-4144.
141. Qian, J.; Wu, X.; Cao, Y.; Ai, X.; Yang, H., High capacity and rate capability of amorphous phosphorus for sodium ion batteries. *Angewandte Chemie* **2013,** *125* (17), 4731-4734.
142. Ramireddy, T.; Rahman, M. M.; Xing, T.; Chen, Y.; Glushenkov, A. M., Stable anode performance of an Sb–carbon nanocomposite in lithium-ion batteries and the effect of ball milling mode in the course of its preparation. *Journal of Materials Chemistry A* **2014,** *2* (12), 4282.
143. De Keijser, T. H.; Langford, J.; Mittemeijer, E. J.; Vogels, A., Use of the Voigt function in a single-line method for the analysis of X-ray diffraction line broadening. *Journal of Applied Crystallography* **1982,** *15* (3), 308-314.
144. Kostecki, R.; Schnyder, B.; Alliata, D.; Song, X.; Kinoshita, K.; Kötz, R., Surface studies of carbon films from pyrolyzed photoresist. *Thin Solid Films* **2001,** *396* (1–2), 36-43.
145. Datta, M. K.; Epur, R.; Saha, P.; Kadakia, K.; Park, S. K.; Kumta, P. N., Tin and graphite based nanocomposites: Potential anode for sodium ion batteries. *Journal of Power Sources* **2013,** *225*, 316-322.
146. Sun, J.; Zheng, G.; Lee, H.-W.; Liu, N.; Wang, H.; Yao, H.; Yang, W.; Cui, Y., Formation of Stable Phosphorus–Carbon Bond for Enhanced Performance in Black Phosphorus Nanoparticle–Graphite

Composite Battery Anodes. *Nano letters* **2014,** *14* (8), 4573-4580.
147. Liu, Y.; Zhang, N.; Jiao, L.; Tao, Z.; Chen, J., Ultrasmall Sn Nanoparticles Embedded in Carbon as High-Performance Anode for Sodium-Ion Batteries. *Advanced Functional Materials* **2015,** *25* (2), 214-220.